

Development of a Hyperbaric Intravascular Membrane Oxygenator Catheter

by

Stewart Farling

Department of Civil & Environmental Engineering
Duke University

Date: _____

Approved:

Marc Deshusses, Advisor

Mark Wiesner

Michael Bergin

Bruce Klitzman

Dissertation submitted in partial fulfillment of
the requirements for the degree of Doctor
of Philosophy in the Department of
Civil & Environmental Engineering in the Graduate School
of Duke University

2021

ABSTRACT

Development of a Hyperbaric Intravascular Membrane Oxygenator Catheter

by

Stewart Farling

Department of [Department]
Duke University

Date: _____

Approved:

Marc Deshusses, Advisor

Mark Wiesner

Michael Bergin

Bruce Klitzman

An abstract of a dissertation submitted in partial
fulfillment of the requirements for the degree
of Doctor of Philosophy in the Department of
Civil & Environmental Engineering in the Graduate School of
Duke University

2021

Copyright by
Stewart Ryan Farling
2021

Abstract

Acute Respiratory Distress Syndrome (ARDS), a form of acute lung injury resulting in hypoxic respiratory failure is a frequent and often lethal indication for admission to both adult and pediatric intensive care units (ICUs). Currently, patients in need of oxygen support must rely on conventional methods that use a patient's lungs to deliver oxygen, such as mechanical ventilation. In severe cases where patients' lungs are damaged to a point that they are unable to be supported with mechanical ventilation, currently the only option is extracorporeal membrane oxygenation (ECMO). This method of oxygenation bypasses the lungs and directly oxygenates the blood. However, this is a costly, highly sophisticated treatment typically only available in select large hospitals who have the required resources. The onset of the COVID-19 pandemic made clear that the need for alternative, lung-independent, oxygen delivery methods for patients is a dire need in the medical field. Smaller devices that can be easily deployed, used in more hospitals, and are cheaper to manufacture and administer, would find immediate use in the medical field to help patients who would otherwise not have access to ECMO.

The hyperbaric intravascular oxygenator catheter is a concept that Dr. Tobias Straube (Duke University) conceived in response to this need. The idea behind this

device is to deliver critical levels of oxygen to patients in need with easy to deploy catheter-based devices.

The primary objective of this dissertation was to develop the concept of this hyperbaric intravascular oxygenation catheter as a future treatment option in patients with ARDS. The work consisted of the development of a proof-of-concept device using hollow fiber dense membranes and hyperbaric oxygen to diffuse oxygen at transfer rates greater than previous works. A conceptually accurate mathematical model was developed to investigate system limitations in the early prototype, and guide future investigations. Blood mixing methodologies were developed and tested at the bench scale to determine the feasibility of angular oscillation-based mixing on both transport efficiencies and impacts on bubble formation, and the previous model was used to evaluate the system. Finally, an investigation on the mechanisms behind the angular oscillation was conducted using computational fluid dynamics.

Initial work demonstrated the technical feasibility of providing oxygen to a bulk medium, such as blood, via diffusion across non-porous hollow fiber membranes (HFM) using hyperbaric oxygen. The oxygen transfer across Teflon AF 2400 membranes was characterized at oxygen pressures up to 2 bars in both a stirred tank vessel (CSTR) and a tubular device mimicking intravenous application. Fluxes over $550 \text{ mL min}^{-1} \text{ m}^{-2}$ were observed in well-mixed systems, and just over $350 \text{ mL mL min}^{-1} \text{ m}^{-2}$ in flow through tubular systems. Oxygen flux was proportional to the oxygen partial pressure inside the

HFM over the tested range and increased with mixing of the bulk liquid. Some bubbles were observed at the higher pressures (1.9 bar) and when bulk liquid dissolved oxygen concentrations were high. High frequency ultrasound was applied to detect and count individual bubbles, but no increase from background levels was detected during lower pressure operation. A conceptual model of the oxygen transport was developed and validated. Model parametric sensitivity studies demonstrated that diffusion through the thin fiber walls was a significant resistance to mass transfer. Promoting convection around the fibers should enable physiologically relevant oxygen supply. This work indicated that a device is within reach that is capable of delivering greater than 10% of a patient's basal oxygen needs in a configuration that readily fits intravascularly.

Proof-of-concept work highlighted the need for an active mixing method that would both improve flux while also limiting conditions favoring bubble formation in such a hyperbaric device. We demonstrated that the introduction of angular oscillation as a form of active mixing allowed for fluxes of up to $400 \text{ mL min}^{-1} \text{ m}^{-2}$ at lower pressures than our previous work. This increase of almost $150 \text{ mL min}^{-1} \text{ m}^{-2}$ was achieved despite the use of water maintained at body temperature (37 C°) and at the viscosity of blood (3.5 cP), both of which reduce oxygen transfer rates when compared to the 20 C water used in the previous work. Adaptation of the previously developed mathematical model indicated continued improvements maybe achieved with more active mixing. Future work in blood will investigate the effects of angular oscillation on

oxygen transport and bubble formation in an in vitro system, and to determine if this method of active mixing has any deleterious effects on red blood cells.

A computational fluid dynamics analysis using COMSOL was undertaken on the micro and macro-oscillations used in the active mixing schemes. This analysis revealed reasons why micro-oscillations were reducing the incidence of bubbles on fiber walls in bench testing when the fibers were undergoing rapid small motions, while also producing less overall flux as compared to the large oscillations. This result lends itself to future work to optimize the conditions of micro-oscillations such that bubble formation is reduced in bench top prototypes. Additionally, there is potential to optimize the range of motions used in micro-oscillations to reduce the impact of overall oxygen flux as compared to large consistent motion in real world testing.

Overall, this work demonstrated the feasibility of using hyperbaric pressures in an oxygen delivery catheter and that a mixing methodology using angular oscillation could be employed that would increase flux rates while also limiting bubble formation. Mathematical models were developed that gave insight to a hypothetical catheter's mass transport limitations, and can be used to investigate hypothetical changes to the device. Finally, a CFD model was developed to better understand the angular oscillation mixing that was able to reduce bubble formation in this system.

Dedication

To my family who has supported me through thick and thin.

To my loving wife, Lindsay, who inspires me every day.

Contents

Abstract	iv
List of Tables	xiii
List of Figures	xiv
Acknowledgements	xix
1. Introduction	1
1.1 The motivation for intravascular oxygenation.....	1
1.2 Potential benefits of intravascular oxygenation.....	3
1.3 State of the art in intravascular oxygenation.....	5
1.3.1 IVOX Catheter.....	5
1.3.2 Hattler Catheters	7
1.3.3 Dynamic Intravascular Lung Assist Device	10
1.3.4 Intracorporeal Oxygenator with Woven Tubes	11
1.3.5 Penn State Intravascular Lung.....	12
1.3.6 Intravascular Pumping Oxygenator	13
1.3.7 Polyamide Hollow Fiber Intravascular Oxygenator Device	14
1.3.8 Intravascular Lung Assist Device	15
1.3.9 Highly Integrated Intravascular Membrane Oxygenator.....	16
1.3.10 Previous work conclusions	17
1.4 Requirements of a hyperbaric intravascular gas exchange catheter	21
1.4.1 Safety Considerations	21

1.4.2 Membrane considerations	22
1.4.3 Gas exchange requirements	25
2. Development of a novel intravascular oxygenator catheter: Oxygen mass transfer properties across nonporous hollow fiber membranes	30
2.1 Introduction.....	30
2.2 Materials and Methods	34
2.2.1 Experimental systems	34
2.2.2 Experimental procedure and analytical equipment.....	36
2.3 Data analysis	36
2.3.1 Ultrasound bubble detection	37
2.3.2 Model development.....	38
2.4 Results and Discussion	43
2.4.1 Oxygen transfer: time series and fluxes	43
2.4.2 Bubble investigations.....	49
2.4.3 Modeling oxygen transfer in the devices and model parametric sensitivity	52
2.5 Conclusions	59
3. Oxygenation Catheter mixing via angular oscillation.....	61
3.1 Introduction.....	61
3.2 Materials and methods	64
3.2.1 Angular oscillation.....	64
3.2.2 Water based bench system.....	67
3.2.3 Blood mimic	71

3.2.4 System modeling	71
3.3 Results and discussion.....	74
3.3.1 Effect of angular oscillation on oxygen bubble formation.....	74
3.3.2 Effect of angular oscillation on oxygen flux	79
3.3.3 Ability to mimic blood.....	83
3.3.4 Model insights.....	88
3.4 Conclusions	95
4. Computational fluid dynamic modeling: oscillation investigation.....	98
4.1 Introduction.....	98
4.2 Materials and Methods	100
4.2.1 Model description and assumptions	100
4.2.2 Model physics	106
4.2.3 Model evaluations	109
4.3 Results and Discussion	112
4.3.1 Relative mass flow results.....	112
4.3.2 Maximum wall concentration results.....	116
4.4 Conclusions	124
5. Conclusions.....	126
5.1 Proof of concept work: hyperbaric oxygenation catheter feasibility.....	126
5.2 Angular oscillation active mixing applied to oxygenation catheter	127
5.3 Computational fluid dynamic modeling of micro-scale mixing mechanisms for oxygenator catheter designs	128

5.4 Conclusions	130
Appendix A – Supplemental Information: Development of a novel intravascular oxygenator catheter: Oxygen mass transfer properties across nonporous hollow fiber membranes.....	132
A.1 Oxygen Mass Transport and Model Equations	132
A.2 Supplemental Figures	137
A.3 On-line videos.....	137
Appendix B Oxygenation Catheter mixing via rotational oscillation	139
References	144
Biography.....	151

List of Tables

Table 1: Summary of prior and current intravascular oxygenator research and devices.	19
Table 2: Model parameters used in this study.	42
Table 3: Mixing regimes investigated in this study (Chapter 3).	67
Table 4: Summary of hollow fibers used in angular oscillation testing. Fiber A was previously used in proof-of-concept work (Chapter 2).	69
Table 5: Model parameters used in this study to characterize 4 fibers across various mixing regimes.	73
Table 6: Summary of fitted mass transfer coefficient values for each mix regime modeled.	90
Table 7: Parametric values used in COMSOL model parametric sweeps for micro oscillation analysis.	105
Table 8: List of model symbols and model parameter values (with sources)	132

List of Figures

Figure 1: The IVOX catheter demonstrating intravascular oxygenation catheter insertion via the femoral vein and deployed in the vena cava.	3
Figure 2: Illustration of (A) porous HFM, (B) Coated HFM, and (C) non-porous HFM in contact with blood.....	23
Figure 3: Hypothetical fiber bundle (A) using non-porous HFM to achieve bubbleless (B) oxygenation of blood using the high oxygen gradient of hyperbaric	25
Figure 4: Arterial oxyhemoglobin saturation as a function of theoretical intravascular catheter oxygen delivery.....	27
Figure 5: Process schematic of bench top system and instruments.	34
Figure 6: Conceptual model of the membrane interfaces with high pressure oxygen inside the fiber,	39
Figure 7: Time series of dissolved oxygen for single fiber tubular device (30 cm fiber) and CSTRs (20 cm fiber) at two different average oxygen pressures.....	44
Figure 8: Subset of instantaneous oxygen flux vs. liquid partial pressure of oxygen for the selected single fiber CSTR and tubular experiments shown in Figure 7.....	45
Figure 9: Experimentally determined fluxes at select liquid partial pressures for CSTR systems.	47
Figure 10: Experimentally determined flux at select liquid partial pressures for tubular devices (a and b are replicate experiments).	48
Figure 11: Experimental observation of gas bubbles in the tubular device using ultrasounds.	51
Figure 12: Model fitting for the convective mass transfer coefficient for the CSTR (A) and the tubular device (C) for a single replicate, and model predictions	53
Figure 13: Sensitivity of instantaneous oxygen flux to the mass transfer coefficient k and to membrane oxygen pressure.....	55

Figure 14: Sensitivity of instantaneous flux to membrane wall thickness of the CSTR model and to the convective mass transfer coefficient (0.001 to 0.1 cm s ⁻¹)	56
Figure 15: Sensitivity of instantaneous flux to membrane permeability of the CSTR model and to the convective mass transfer coefficient (0.001 to 0.1 cm s ⁻¹)	57
Figure 16: Contour plot for total oxygen transfer rate as a function of pressure and total fiber area, for two different mass transfer coefficients (k).	58
Figure 17: Fiber bundle consisting of Fiber A (88.9 μm wall thickness, 406 μm diameter) used in experiments.....	65
Figure 18: Illustration of individual fiber motion undergoing macro steps (A) and macro + micro step (B) oscillations.	65
Figure 19: Example of angular position over time for an example mixing regime	66
Figure 20: Process schematic of bench top system using water and blood mimic.	70
Figure 21: Oxygen flux vs average fiber pressure for single fiber loops (34 cm) of fibers A, B, C, and D using mix 1 (3200 deg/s 180 degrees) at 0.5 LPM system flow.....	74
Figure 22: Number of bubbles counted on fibers versus average fiber pressure.	77
Figure 23: Number of bubbles formed vs average fiber pressure for a single loop of fiber C.....	78
Figure 24: Flux of fiber bundle C (32 total fibers, 14.6 cm each) at various mix regimes at high (5 PSI) and low (2.125 PSI) pressures under two flow conditions (0.5 and 2.0 LPM).	79
Figure 25: Flux of fiber bundle A (30 total fibers, 16.2 cm each) at various mix regimes at high (5 PSI) and low (2.125 PSI) pressures	80
Figure 26: Flux vs angular speed for fiber C bundle at 0.5 (solid) and 2.0 (dashed) LPM with macro and macro + micro oscillation regimes at 2.125 PSI average fiber pressure..	81
Figure 27: Flux vs angular speed for fiber C bundle at 0.5 (solid) and 2.0 (dashed) LPM with macro and macro + micro oscillation regimes at 5.0 PSI average fiber pressure	82

Figure 28: Flux vs angular speed for fiber A bundle at 0.5 LPM with macro and macro + micro oscillation regimes at 2.125 and 5.0 PSI average fiber pressure.	83
Figure 29: Close-up image of fiber A bundle after being tested in blood mimic solution consisting of sodium sulfite (0.014 M), cobalt(II) (0.0005 M), in 37 °C water at 3.5 cP.	84
Figure 30: Time series outlet DO data collected for fiber bundle A during sodium sulfite blood mimic testing demonstrating no increase in DO as the system is operating.	85
Figure 31: Time series outlet DO data for fiber bundle A collected during sodium sulfite blood mimic testing	86
Figure 32: Time series outlet DO data collected for fiber bundle A after a visible coating deposited on surface.....	87
Figure 33: Time series dissolved oxygen (black) and model fit (red) data for fiber bundle C at 2 LPM flow rate.....	89
Figure 34: Dissolved oxygen model data vs actual for the reactor outlet with fiber bundle A at 2 LPM.....	91
Figure 35: Dissolved oxygen model data vs actual for the reactor outlet with fiber bundle C at 2 LPM. This data was used to train the model.....	92
Figure 36: Fitted mass transfer coefficients (k) vs angular speed of mixing for macro and macro + micro oscillation mix methods.....	93
Figure 37: Mass transfer coefficient (k) versus estimated oxygen flux from model data at 0.147 bar.....	94
Figure 38: Model-simulated oxygen flux vs. mass transfer coefficient (k) at various pressures for fiber A and C.....	95
Figure 39: 2D model geometry of five 1 cm fiber segments within a 1 cm diameter tube.	102
Figure 40: Triangle wave depicting fiber 'bundle' displacement as a function of time for a typical study	103
Figure 41: Triangle wave depicting fiber 'bundle' displacement as a function of time for a typical study analysis that includes a macro step movement.	104

Figure 42: Triangular wave function for a frequency of 5 Hz for 3 different amplitudes.	105
Figure 43: Example of extra frequency included in analysis to ensure that data is generated using the same velocity of motion for different total micro movements.	106
Figure 44: Mass flow out of the model over run time for various model runs (unlabeled) showing psuedo-steady states reached after roughly 2-3 seconds.	110
Figure 45: Cumulative mass out over time plotted after integration via MATLAB. Time- series are a subset of all model runs (unlabeled).	110
Figure 46: Relative mass value derived after normalizing cumulative mass out over time data to the worst-case model.	111
Figure 47: 2D geometry with center fiber walls highlighted in red, indicating boundary at which the maximum wall concentration data is monitored.	112
Figure 48: Relative total mass out of 2D model after 20 seconds for 0.05 LPM flow condition for fiber-fiber spacing between 100 and 400 μm versus average travel velocity.	114
Figure 49: Relative total mass out of 2D model after 20 seconds for 0.1 LPM flow condition for fiber-fiber spacing between 100 and 400 μm versus average travel velocity. Macro steps vary between off (1 μm) and on (500 μm).	115
Figure 50: Time series data of maximum [right side] fiber wall DO concentration for 0.05 LPM and 100 μm fiber-fiber spacing.	117
Figure 51: Time series data of maximum [right side] fiber wall concentration for 0.05 LPM and 200 μm fiber-fiber spacing.	118
Figure 52: Time series data of maximum [right side] fiber wall concentration for 0.05 LPM and 400 μm fiber-fiber spacing.	119
Figure 53: Time series data of maximum [right side] fiber wall concentration for 0.1 LPM and 100 μm fiber-fiber spacing.	120
Figure 54: Time series data of maximum [right side] fiber wall concentration for 0.1 LPM and 200 μm fiber-fiber spacing.	121

Figure 55: Time series data of maximum [right side] fiber wall concentration for 0.1 LPM and 400 μm fiber-fiber spacing.	122
Figure 56: Conceptual model of the membrane interfaces with high pressure oxygen inside the fiber,	133
Figure 57: Schematic of discretization of tubular system model (single fiber).	135
Figure 58: Model fitting for the convective mass transfer coefficient for the CSTR at 400 rpm CSTR (A) and the tubular device at 0.5 L min ⁻¹ (B) for a single replicate.	137
Figure 59: Conceptual model of the membrane interfaces with high pressure oxygen inside the fiber,	139
Figure 60: Schematic of discretization of tubular system model (single fiber looped). ...	142

Acknowledgements

This work was undertaken with contributions from many colleges, friends, and even family. I first must thank my advisor, Professor Marc Deshusses. I began my PhD journey under Dr. Deshusses investigating odors and bioaerosols related to fecal sludge management, and when I began work on the medical device research detailed in this dissertation, he continued to be an invaluable advisor to myself and others. His mentorship in planning, conducting, and importantly reporting research is immeasurable, and has made me a better researcher. I also want to thank my committee Professors Mark Wiesner, Michael Bergin, and Bruce Klitzman for their involvement in strengthening this research.

I would like to thank Dr. Tobias Straube, who came up with the idea for hyperbaric oxygen-based catheters as a means to save the lives of neonates and young children in the pediatric intensive care unit. He believed in my ability to contribute to this project, which allowed me to start working in this exciting field of research. Dr. Travis Vessel should also be thanked as a collaborator in this work, providing invaluable feedback and guiding the project to be clinically relevant. I especially want to thank Dr. Paolo Maccarini for his support in multiphysics modeling, providing access to computers, and his time spent answering questions related to this effort.

I would also like to thank my former Masters thesis advisor, Dr. Robert Borden, who gave me my first opportunity to work in a research lab as an undergraduate

student. His early mentorship in research developed a curiosity that continues to this day.

I would also like to thank my many current and former fellow students, shared office space users, cohort, and fellow Deshusses lab mates: Thank you for inspiring me, encouraging me, and providing a firm wall to bounce ideas off of at any time!

I want to say a special thanks to the people that run our department, Ruby Nell Carpenter and Dwina Martin. Ruby has helped with any question I have ever had, and made sure I was on track for important things from class registration to this dissertation defense. Dwina has been absolutely amazing during this work, answering questions, helping get to the bottom of problems, tracking down orders, but most importantly, she has willing to listen any day of the week to problems that arose ranging from DI water to the current crop in my vegetable garden.

1. Introduction

The following chapter is modified from a draft review journal article planned for submission in April 2021 titled *“Intravascular Gas Exchange: Physiology, Literature Review, and Current Efforts”* authored by Tobias L. Straube, Stewart Farling, Marc A. Deshusses, Bruce Klitzman, Ira M. Cheifetz, Travis P. Vesel

1.1 *The motivation for intravascular oxygenation*

Respiratory diseases affect millions of people every year, and include illnesses such as asthma, bacterial and viral pneumonias, chronic obstructive pulmonary disease (COPD), and pulmonary interstitial diseases amongst others [1], [2]. Chronic respiratory disease is a top 5 leading cause of death worldwide, and the 4th leading cause in the US alone [1], [3], [4]. Treating these diseases accounts for a significant portion of all health care spending in the US, amounting to over \$132 billion dollars in 2013 [1], [5].

Acute respiratory distress syndrome (ARDS), a subset of hypoxic respiratory failure with acute lung injury, is a leading cause of admission to intensive care units (ICU) in both children and adults, often requiring significant medical interventions to address patient oxygen needs. ARDS was present in 7% of adult ICU patients and represented 1-10% of pediatric ICU (PICU) admissions [6]–[9] before the COVID-19 pandemic. Following the onset of the pandemic there has been further increases in ARDS cases in ICUs [10], [11].

While the prevalence, morbidity, and mortality related to ARDS is high, there are few treatment options that exist beyond conventional mechanical ventilation. When mechanical ventilation fails to adequately oxygenate these patients, they can be supported with veno-venous extracorporeal membrane oxygenation (VV-ECMO). VV-ECMO is the only available therapy that directly oxygenates blood independent of the lungs and, therefore, is capable of fully supporting a patient regardless of degree of lung injury. Unfortunately, VV-ECMO is associated with many serious complications, including hemorrhage, thrombosis, infection, and end-organ injury [12]. ECMO is available only in approximately 3% of hospitals in the United States [13], and fewer worldwide. The complexity of ECMO, associated morbidity, and availability limit the benefits of this life-saving technology. There is an urgent need for safe alternative technologies that support patients with severe respiratory failure that function independently of diseased lungs.

1.2 Potential benefits of intravascular oxygenation

An intravascular respiratory assist catheter is a central venous catheter that participates in gas exchange to support patients with respiratory failure via placement in into a central vein such as in the IVOX device shown in **Figure 1** [14].

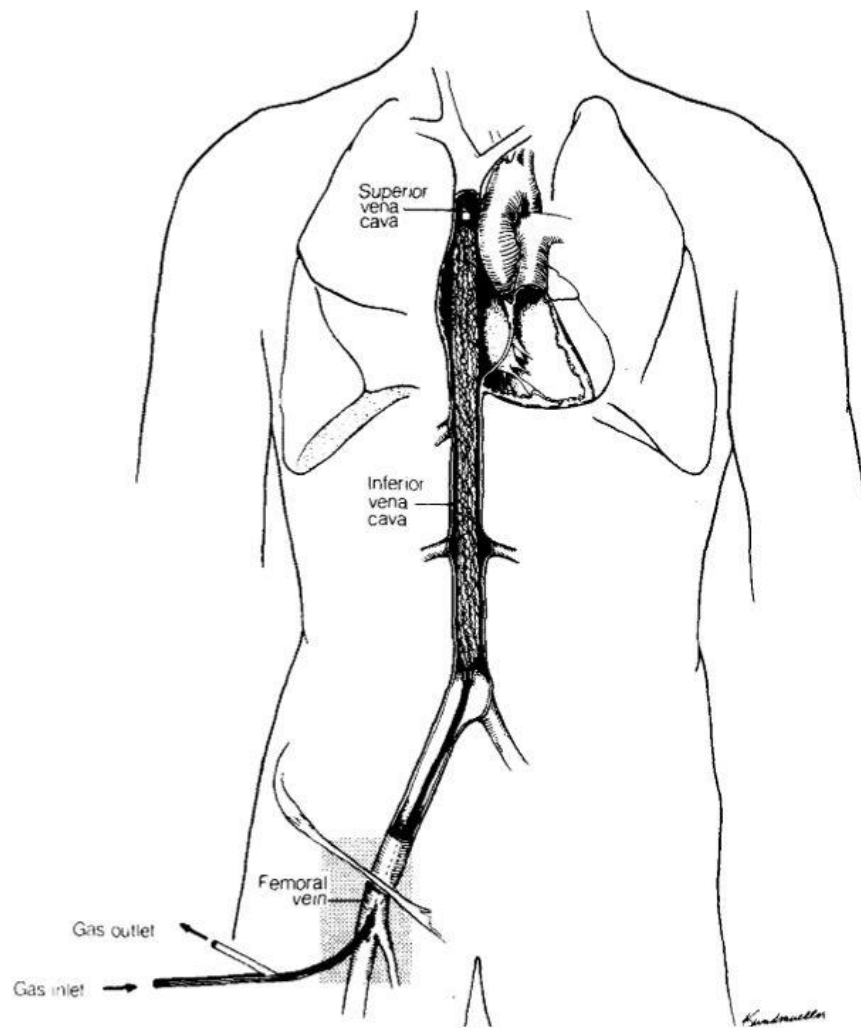


Figure 1: The IVOX catheter demonstrating intravascular oxygenation catheter insertion via the femoral vein and deployed in the vena cava.

The expectation for these catheters is that they could be placed in patients at the bedside, in an ambulance, or even in the field. Ideally, once inserted, operation would involve basic titration of the gas flowing through the device. The benefits of an intravascular respiratory assist catheter would exist on a spectrum dependent on its efficiency at gas exchange and risk profile. A complete respiratory assist catheter must be effective at both delivering oxygen and removing carbon dioxide (CO₂).

Alternatively, devices, such as the proposed device developed in this work, could be designed with the goal to predominantly deliver oxygen or to remove CO₂. For lung disease with resultant hypoxic respiratory failure, either a complete respiratory assist catheter or a device whose purpose is to solely deliver oxygen would be useful. Such a catheter could be used in isolation, with or without supplemental oxygen, or in conjunction with mechanical ventilation. When combined with mechanical ventilation this catheter may allow for reduced ventilator support, which may reduce ventilator-induced lung injury (VILI) due to reduction in ventilator settings that could cause damage to lungs. Hattler et al. suggested that providing approximately 20% of an adult's basal oxygen needs (50 mL O₂ min⁻¹) would achieve an arterial oxygen saturation of 90% in patients with only 50% of their native lung function intact [15]. Clinically, Conrad et al. showed that when the IVOX catheter, the only intravascular respiratory assist catheter to be tested in a human clinical trial, delivered 40-70 mL O₂ min⁻¹ it

allowed for reduction of mechanical ventilation by 25% or more in approximately 50% of patients [16].

1.3 State of the art in intravascular oxygenation

In the following sections, the characteristics of previous attempts at developing respiratory assist catheters are presented in chronological order. Lessons learned from these previous attempts at intravascular gas exchange are highlighted and discussed. A summary of the main characteristics of each device is presented in **Table 1**.

1.3.1 IVOX Catheter

The only intravascular gas exchange device tested in human clinical trials has been the IVOX device developed by Mortenson and colleagues beginning in the 1980s at CardioPulmonics Inc. (Salt Lake City, USA) [17]. The IVOX device was an oxygenator composed of hollow fiber membranes (HFM) with surface areas between 2,100 and 5,000 cm². It was designed for use within the vena cava, where venous blood could flow passively around the external surfaces of the fibers. Sub-atmospheric pressure oxygen was pulled via vacuum through the lumens of the hollow fibers [14]. The fiber membranes were composed of porous polypropylene covered with an ultrathin, selectively gas permeable, siloxane membrane that allowed gas transfer, but no water nor plasma exchange. These fibers were crimped to minimize fiber clumping and to disrupt blood flow to enhance efficiency. The device was surgically inserted via

venotomy into either the right internal jugular or femoral vein [14]. Various sizes were tested clinically ranging from 38 to 48 Fr (1.26 to 1.6 cm) in diameter in the furled insertional configuration and 30 to 40 cm in length.

The IVOX device was tested in a clinical trial from 1990 to 1993 in 160 patients with acute hypoxic and/or hypercapnic respiratory failure receiving positive pressure ventilation [16]. Patients were selected for testing if they remained hypoxic ($\text{PaO}_2 < 60$ mmHg) despite $\text{FiO}_2 > 0.5$. On average the device was capable of transferring 40 – 70 mL min^{-1} of oxygen and carbon dioxide into or out of the circulating venous blood, which is approximately 20-30% of a patient's baseline metabolic requirement [16]. At these rates of gas transfer, mechanical ventilation was reduced by 25% or more of pre-IVOX level of intensity in approximately 50% of clinical trial patients. Clinically recognized IVOX-related complications such as bleeding during insertion or removal, venous thrombosis, or vascular obstruction were reported in 24.5% of the clinical trial patients. The effect of device insertion on hemodynamics was appreciable with a 12.5% decrease in average cardiac index (cardiac output per minute per body surface area) noted upon insertion of device (4.0 to 3.5 L $\text{min}^{-1} \text{m}^{-2}$). 17.7% of IVOX devices were reported as having significant mechanical and/or performance malfunction problems (broken fibers, failed potting, furling malfunction) [16].

Unfortunately, there was no control arm in the clinical trial to determine the effect of IVOX on survival. Ultimately, the risks associated with the IVOX catheter seemed too high to justify use when balanced with the benefit of gas exchange provided. The IVOX device failed to gain FDA approval. Cardiopulmonics Inc. eventually discontinued the attempt for FDA approval and halted further device development. Their experience highlighted the need to increase the gas exchange efficiency of intravascular devices in order to make them smaller or exchange more gas to offset the risks associated with their size.

1.3.2 Hattler Catheters

The Hattler Catheter, developed by Hattler and Federspiel beginning in the late 1980s at the McGowan Institute for Regenerative Medicine at the University of Pittsburgh, was a total respiratory assist catheter composed of a bundle of hollow fiber membranes with sub-atmospheric oxygen flowing within [18]. This group developed several prototype iterations that incorporated various methods to enhance gas exchange efficiency. They accomplished some of the highest gas fluxes reported in the literature.

One of their early prototypes consisted of 600 polypropylene hollow fiber membranes (240 and 300 μm inner and outer diameter, respectively) bundled around a pulsating balloon capable of inflating and deflating at 300 beats per minute [15]. This pulsating balloon pumped blood through and around the bundle of HFM at greater

velocities than would otherwise be achieved with passive flow in the vena cava. It was the first device to incorporate “active mixing” into a respiratory assist catheter. The pumping action of the balloon increased the gas transfer efficiency of the device by about 200-300% depending on vessel sizes, blood flow rates, and pulsation rates when tested *ex vivo* and *in vitro* [15], [19]. However, when these catheters were tested *in vivo* in large animal models they found a more modest increase in gas exchange of only 30 to 40% with balloon pulsation [20]–[22]. In water this device was capable of delivering 140 mL O₂ min⁻¹ m⁻² of catheter diffusing surface area, corresponding to 24 mL O₂ min⁻¹ total oxygen delivery. They were unable to accurately measure oxygen delivery *in vivo*. The CO₂ transfer efficiency *in vivo* was 305 mL min⁻¹ m⁻² with a total gas exchange of 52 mL CO₂ min⁻¹. They found that their largest balloon (40 mL during inflation) resulted in a significant reduction in cardiac output when implanted in 90 to 100 kg calves. This device never made it to human clinical trials [15].

Another iteration of the Hattler Catheter developed in the 2000s, the Percutaneous Respiratory Assist Catheter (PRAC), consisted of 525 HFMs potted within a manifold capable of rotating at 12,000 RPM [23]. Rotation was intended to induce mixing and convection of oxygenated blood away from the fiber bundle into the bulk and increase the relative velocity of blood flow past the fiber surfaces, thereby enhancing gas exchange efficiency. Using this rotational design, they were able to

construct a device with a smaller insertional diameter of 8.3 mm [23]. The efficiency of oxygen exchange increased to $370 \text{ mL min}^{-1} \text{ m}^{-2}$ in blood when compared to their pulsating balloon device. Preliminary hemolysis results associated with operation of the PRAC device was similar to that of a commercially available intra-aortic balloon pump used as a control, though they noted high variability of these results. Given the concern for vascular endothelial damage due to the rotating fiber bundle within the vena cava, Hattler and Federspiel engineered a 3rd device composed of an impeller within the hollow fiber bundle[24]. This Impeller Percutaneous Respiratory Assist Catheter (iPRAC) was a 30 cm long 250 HFM bundle wrapped around a wire coil/cage containing mounted impellers of various geometries. The impeller was capable of rotating up to 20,000 RPM. This design demonstrated CO_2 exchange efficiency of $523 \text{ mL min}^{-1} \text{ m}^{-2}$ in vivo, an increase of 70% when compared to their original balloon pulsating catheter. The oxygenation data was not reported for the iPRAC device as the team began shifting their focus to CO_2 removal (in part due to the continued imprecision for in vivo oxygen delivery measurements). The iPRAC did not progress beyond large animal studies.

These devices developed by Hattler and Federspiel represented an important advance in respiratory assist catheter technology. They were able to increase oxygen flux by about 70% compared to the IVOX catheter with their ability to incorporate methods of mechanical mixing. Even with these methods of mechanical

mixing, they were able to engineer and test prototypes with much smaller diameters than the IVOX catheter (~ 8 vs 12-16 mm, respectively). However, due to the overall low total oxygen transfer of these prototypes, Hattler and Federspiel focused efforts on CO₂ removal, as well as development of total artificial extracorporeal lungs.

1.3.3 Dynamic Intravascular Lung Assist Device

At the same time that Hattler and Federspiel were developing the balloon pulsating respiratory assist catheter, a group from Northwestern University developed the Dynamic Intravascular Lung Assist Device (D-ILAD). This device was the first to use movement of the gas diffusing surface of the catheter as a means to enhance the gas exchange efficiency. The D-ILAD used rotation and oscillation to increase gas transfer and reduce resistance to blood flow across the device[25], [26]. This device preceded that of the rotating catheter developed by the Hattler group by about a decade. Similar to the other gas exchange catheters, the D-ILAD was intended to be placed within the vena cava. The device was composed of between 2,000 and 3,800 microporous polypropylene fibers potted in a manifold forming a sheet (or sheets) which was twisted around a supporting shaft, forming a screw-like configuration. Surface areas of prototypes ranged from 0.3 to 0.5 m² depending on the configuration. The rotation of the fibers enhanced gas transfer and also served to pump blood forward thereby decreasing its resistance to flow. Their most efficient device could exchange 208 mL O₂ min⁻¹ m⁻² when tested in

vitro using bovine blood. They showed that oscillatory motion increased gas exchange when compared to continuous rotation of the fiber bundle, however, the pumping effect of the screw-like configuration was lost with oscillation. Despite this device having “active” mixing, it did not result in an increase in oxygen flux when compared to the stationary IVOX catheter ($208 \text{ mL O}_2 \text{ min}^{-1} \text{ m}^{-2}$ compared to $142 - 219 \text{ mL O}_2 \text{ min}^{-1} \text{ m}^{-2}$ respectively). However, it did represent a significant advance in that there was no pressure drop across their screw-like device, even with blood flow at 5.9 L/min [26]. This achievement is particularly important as respiratory assist catheters are intended function in the vena cava, where passive blood flow under low pressure is easily disrupted.

1.3.4 Intracorporeal Oxygenator with Woven Tubes

Beginning in the 1990s, a group from Keio University in Japan, in collaboration with others at Penn State and Brown University, developed a prototype intravascular oxygenator device using large woven hollow tubes as a means to induce convective mixing amongst blood flow streams. This device consisted of eight large 1.8 mm diameter microporous PTFE tubes with an approximate insertional diameter of 1 cm . Interestingly, they tested this device with blood flowing external to the tubes (with oxygen flowing internally) and vice versa. Despite the finding that the woven design improved gas exchange compared to straight tubes, this design only achieved an oxygen

transfer efficiency of $40 \text{ mL O}_2 \text{ min}^{-1} \text{ m}^{-2}$ at low blood flow rates of 25 mL min^{-1} [27].

Increasing blood flow beyond this slow rate did little to increase the oxygen exchange efficiency due to the high ratio of blood priming volume to gas exchanging surface area within the test conduit. This high ratio highlights the importance of minimizing “shunting” of blood past respiratory assist catheters to ensure maximal contact of blood with gas diffusing surface area.

1.3.5 Penn State Intravascular Lung

The Penn State Intravascular Lung (PENSIL) was developed in the mid-1990s and was designed to be deployed into the vena cava, right atrium, right ventricle, and the pulmonary artery to maximize exposure to the entire venous return [28]. Placing the catheter within the pulsatile flow of the right ventricle and pulmonary artery was proposed to enhance mixing. The 100 to 150 cm long catheter was composed of 10 or more manifold segments that each contained 198 fibers ($380 \text{ }\mu\text{m}$ OD, $50 \text{ }\mu\text{m}$ wall thickness) of blind-ended microporous polypropylene HFM attached radially to a catheter through which oxygen flowed. It was hypothesized that fibers only attached to a manifold on one end could reduce the insertional size of the device and reduce areas of tight packing, which theoretically could diminish thrombus formation. Oxygen was cycled in and out of the blind-ended fibers, or pressure held continuously in some, while a vacuum was placed in others to help with CO_2 clearance. A device with 0.5 m^2

diffusing surface area tested in vitro was only capable of transferring 15-20 mL O₂ min⁻¹ (or a flux of 35 mL O₂ min⁻¹ m⁻²) [28]. The PENSIL catheter is the only catheter in the literature to use blind-ended hollow fiber membranes rather than loops of hollow fibers with a gas inlet and outlet. Despite efforts at pressure cycling, the buildup of desorbed gas (CO₂) and stagnation of gas within the blind-ended fibers reduced the driving forces for gas exchange in this device. This work demonstrated the importance of maintaining adequate “sweep” flow through the HFMs so as not to diminish the oxygen concentration from back diffusion of water vapor or CO₂. Testing did not progress beyond benchtop in vitro studies and no further attempts at intravascular gas exchange utilized blind-ended fibers.

1.3.6 Intravascular Pumping Oxygenator

The Intravascular Pumping Oxygenator developed at Hiroshima University by Sueda and colleagues in the late 1990s was a respiratory assist catheter combined with a balloon pumping-action for circulatory support [29]. This unique device was composed of 40 nonporous silicone hollow fiber “balloons” that expanded when gas was delivered into them. Each expanding fiber was 1 mm in diameter (when deflated) with 50 μm wall thickness. This device consisted of fewer and larger fibers than most attempts at intravascular gas exchange in order to facilitate its pumping action. An artificial “heart” driver delivered oxygen into the fibers during the balloon inflation phase with a

maximum pressure of 120 mmHg while a vacuum pulled gas out of them during the deflation phase [29]. It is the first device reported in the literature that used a nonporous material to prevent gas emboli, which allowed positive pressure oxygen to inflate the silicone balloons during “systole”. It appears they designed this device to operate to a maximum of 120 mm Hg of oxygen pressure during balloon inflation to prevent catastrophic rupture of the membrane, and to keep pressures generally equivalent to that of normal adult systolic blood pressures (which could reduce amount of gas emboli by preventing convective gradient if there was membrane rupture). The device had a total gas diffusion surface area of 0.035 m² during the inflated phase and was able to deliver 6.3 mL O₂ min⁻¹ for a total flux of 179 mL O₂ min⁻¹ m⁻² in an experimental ex vivo model. It was able to transfer 4.2 mL CO₂ min⁻¹ at maximum pumping blood flows of 250 mL min⁻¹. The gas exchange provided was too low to be clinically significant.

1.3.7 Polyamide Hollow Fiber Intravascular Oxygenator Device

In the late 1990s a group from Tokyo Metropolitan University developed a novel asymmetric fluorinated polyimide hollow fiber membrane intended for intravascular gas exchange [30]. This work appears to be the first reported in the literature where a polymer was developed specifically for the application in an intravascular gas exchange device. This hollow fiber membrane had a defect-free outer skin as thin as 10 nm to prevent plasma wetting with a microporous inner surface to enhance gas transfer.

Mathematical modeling showed this material superior to the microporous polypropylene used by others with possible oxygen transfer rates 2 to 3 times higher [31]. This group reported they had implanted these polyimide hollow fibers in a large animal model without evidence of thrombus formation or fibrin deposition, though the gas exchange data were not reported [30].

1.3.8 Intravascular Lung Assist Device

In the early 2000s a group from Chonbuk National University in South Korea began work on intravascular oxygenation that culminated in prototypes utilizing high frequency vibration to enhance gas exchange. They were the first and only reported in the literature to use high frequency vibration in this application. Intravascular Lung Assist Device (IVLAD) prototypes consisted of microporous polypropylene hollow fiber membranes wrapped around a multi-layer bender piezoelectric actuator. Vibration was intended to decrease the thickness of the blood boundary layers, which by this time was well-known to be a key area of resistance to gas mass transfer in intravascular gas exchange devices. They developed proof-of-concept extracorporeal prototypes with bundles ranging from 100 to 675 hollow fiber membranes placed in a 30 mm diameter conduit. Maximum oxygen transfer efficiency occurred when vibrating the bundle of HFM at 7 Hz, with a gas exchange improvement of 52% when compared to static fibers [32]. Oxygen delivery of 57 mL O₂ min⁻¹ was obtained in blood with the largest

prototype. Importantly, they showed that while hemolysis did occur with their vibrating HFM bundles, it was approximately within the range of commercially available centrifugal blood pumps used in extracorporeal mechanical circulatory support (normalized index of hemolysis of 36 -95 compared to 34- 61 respectively)[33]. Work has continued on the development of IVLAD, though the focus has shifted to improving gas delivery by development of a microencapsulated hemoglobin hemosome that has a high affinity for oxygen binding, intended for simultaneous intravenous infusion during device operation [34].

1.3.9 Highly Integrated Intravascular Membrane Oxygenator

The Highly Integrated Intravascular Membrane Oxygenator (HIMOX) device was developed by a group at the Helmholtz Institute in Germany in the early 2000s [35]. This device was the first to integrate a pump within a catheter to overcome the pressure drop and resistance to flow produced by tightly packed HFMs. This device combined a microaxial blood pump upstream of a bundle of disc-shaped polyolefin HFM. They constructed four prototype bundles containing 480 to 624 hollow fibers to investigate the effects of fiber density and porosity on gas exchange, though notably none these proof-of-concept devices included the microaxial pump. At 3 L min^{-1} of blood flow, the device achieved oxygen transfer efficiency of $450 \text{ mL O}_2 \text{ min}^{-1} \text{ m}^{-2}$, though only a total gas delivery of $6 \text{ mL O}_2 \text{ min}^{-1}$ due to the small surface area. At the time this represented the

highest reported flux in the literature. CO₂ clearance was not investigated. Despite the impressive oxygen exchange efficiency, it appears that further development of HIMOX was halted due to the low overall total oxygen delivery.

1.3.10 Previous work conclusions

Physicians and biomedical engineers have collaborated over the past forty years to develop devices intended for intravascular gas exchange through various technical approaches. Most had limited success with only one device, the IVOX catheter, tested in human clinical trials before development was halted without FDA approval. Each attempt at intravascular gas exchange provided insight on how to optimize conditions affecting gas transport allowing subsequent generation devices to overcome these technical challenges. In particular the previous work has shown that current membrane technology with or without active mixing methodologies have not been able to overcome the mass transfer limitations to achieve clinically relevant oxygen transfer rates with devices small enough for intravascular use. The potential to increase flux with a third external force, hyperbaric pressure, to improve the transport characteristics is therefore a promising next step to further increase oxygen delivery in such devices.

Respiratory assist catheters that are highly efficient and provide a moderate amount of gas exchange could play an important role in preventing the need for more invasive support such as VV-ECMO. The benefits of such intravascular devices capable

of supporting patients with clinically significant gas exchange would be enormous. If successfully developed, their use would represent a major conceptual shift in the way physicians currently treat respiratory failure, as they could provide patients with a minimally-invasive alternative treatment capable of providing gas exchange independent of diseased lungs.

Table 1: Summary of prior and current intravascular oxygenator research and devices

Device	Construction/Design/Materials	Insertional Diameter (mm)	Total Surface Area (m ²)	O ₂ Flux (mL O ₂ /min/m ²)	O ₂ Transfer (mL/min)	CO ₂ Removal (mL/min)	Type of Studies
IVOX [16], [36]	200 μm ID porous polypropylene crimped hollow fiber membrane covered in siloxane coating	12.6 - 16	0.2 to 0.5	142 - 219	43.8 – 71 (blood)	40.3 - 72.5 (blood)	Bench, large animal, human
Hattler Balloon Pulsating Catheter [15], [18]	240 μm ID, 300 μm OD porous polypropylene hollow fiber membrane bundled together around pulsating balloon	9	0.17	140	24 (water)	52 (blood)	Bench, large animal
Percutaneous Respiratory Assist Catheter [37]	240 μm ID, 300 μm OD porous polypropylene hollow fiber membrane potted within manifold capable of rotating at 12,000 RPM	8.33	0.1	370	37 (blood)	52 (blood)	Bench
Impeller Percutaneous Respiratory Assist Catheter [24]	240 μm ID, 300 μm OD porous polypropylene hollow fiber membrane wrapped around wire cage containing several impellers on flexible shaft capable of rotating 20,000 RPM	8.33	0.07	Not reported	10-36 (estimate described in literature)	36 (blood)	Bench, large animal
Dynamic Intravascular Lung Assist Device [25], [26]	3800 microporous polypropylene hollow fiber membranes formed in sheets folded and woven into screw-like configuration capable of rotation and oscillation	< 30	0.29	208	60 (blood)	~50	Bench
Intracorporeal Oxygenator with Woven Tubes [27]	Eight microporous PTFE tubes 1.8 mm in diameter woven together	10	0.05	40	2 (calculated using data provided)	Unknown	Bench

Device	Construction/Design/Materials	Insertional Diameter (mm)	Total Surface Area (m ²)	O ₂ Flux (mL O ₂ /min/m ²)	O ₂ Transfer (mL/min)	CO ₂ Removal (mL/min)	Type of Studies
Penn State Intravascular Lung [28]	280 μm ID, 380 μm OD microporous polypropylene blind-ended hollow fiber membranes attached to central catheter with periodic gas cycling	unknown	0.5	35	15-20 (blood)	Unknown	Bench
Intravascular Pumping Oxygenator [29]	1 mm silicone hollow fiber balloons with 50 μm wall thickness which inflated and deflated to provide pumping action	unknown	0.035	160	6.3 (blood)	4.2	Bench, large animal
Polyamide Hollow Fiber Intravascular Oxygenator Device [30], [31]	novel asymmetric fluorinated polyimide hollow fiber membrane with 10 nanometer defect-free outer skin and microporous inner surface	unknown	unknown	unknown	unknown	unknown	Bench, large animal
Intravascular Lung Assist Device [32]	380 μm ID, 430 μm OD microporous polypropylene hollow fiber membrane bundle wrapped around multi-layer bender piezoelectric actuator capable of high frequency vibration	intravascular prototype never made	unknown	Unknown	57 (blood)	26	Bench
Highly Integrated Intravascular Membrane Oxygenator [35], [38]	220 μm OD tightly packed polyolefin hollow fiber membranes able to be unfurled into disc shaped configuration with integrated microaxial pump	intravascular prototype never made	0.0125	450	6	Not reported	Bench
IntraVascular Membrane Oxygenator [39]	406 μm OD amorphous fluoropolymer hollow fiber membrane bundle with hyperbaric oxygen flowing within	intravascular prototype not yet completed	0.05 to 0.1 (predicted)	350 - 550	17.5 - 55 (predicted)	N/A	Bench

1.4 Requirements of a hyperbaric intravascular gas exchange catheter

1.4.1 Safety Considerations

Safety considerations include risks associated with any intravascular catheter, such as thrombus (blood clot) formation, thromboembolism, infection, and bleeding. Bleeding and infection risks can be minimized with adherence to standard aseptic and hemostasis techniques upon insertion of the device. Regardless of insertional technique, an intravascular respiratory assist catheter will likely have an increased risk of thrombus formation when compared to a standard central venous catheter, as it is assumed it would have a much larger effective diameter and surface area. Catheter design, therefore, should minimize resistance to blood flow in order to mitigate this risk. Other methods to improve hemocompatibility should be considered such as application of heparin-bound surface coatings [40]. Another inherent risk of respiratory assist catheter includes gas embolism. Such emboli could occur either with catastrophic device failure, small bubble formation due to a highly efficient device that results in oxygen supersaturation of the blood, or if a porous gas exchanging HFM was inadvertently placed under excessive pressure. While the effects of pure oxygen emboli are not well understood, every effort should be made to design a device that minimizes the risk of their formation given the known risks of air emboli [41].

1.4.2 Membrane considerations

The lungs have evolved such that they are highly efficient at exchanging gas between the atmosphere and bloodstream. The transport of gasses through this system is a function of the partial pressure gradient across the respiratory membrane, the diffusion coefficient of the membrane, and inversely proportional to the thickness of the membrane. The total rate of diffusion of a given gas is then the product of the flux multiplied by the surface area of the membrane. The human lung has evolved to maximize this gas exchange by utilizing a large surface area to volume ratio combined with a thin respiratory membrane. The respiratory surface area of the adult lung is 50-100 m² (approximately half the size of a tennis court) with only 4 L of total volume[42]. The alveolar-capillary membrane is also extremely thin at ~0.3 μm, reducing resistance to transport across the membrane. The heart is also continuously pumping deoxygenated blood through the pulmonary vasculature to maintain an oxygen diffusion gradient favoring transport from the alveolus to hemoglobin. Additionally, hemoglobin has high oxygen binding affinity, removing oxygen from solution in blood plasma, further maximizing this diffusion gradient.

Reproducing the efficacy of the lung remains a daunting task, particularly when trying to accomplish significant gas exchange within the confines of the intravascular space. As noted, previous attempts focused on achieving the desired oxygen transport by maximizing total membrane surface area while reducing limitations to transport

across the membrane via membrane thickness, porosity, or transport properties of the gas being targeted. When incorporating the largest diffusing surface area possible must be balanced by the inherent size constraints of the vessel in which the catheter is placed so as not to significantly reduce blood flow [15], [43]. The catheter material used for gas exchange should have the highest O₂ and CO₂ diffusion coefficients, and membrane thickness should be minimized [44]. The diffusion gradient can be maximized by using 100% oxygen sweep gas flowing within the hollow fiber membranes (HFM). Further, this work considers can further be increasing the driving force to transport by using hyperbaric pressures [39]. With this in mind, there are several considerations for the type of membrane to use in a given system.

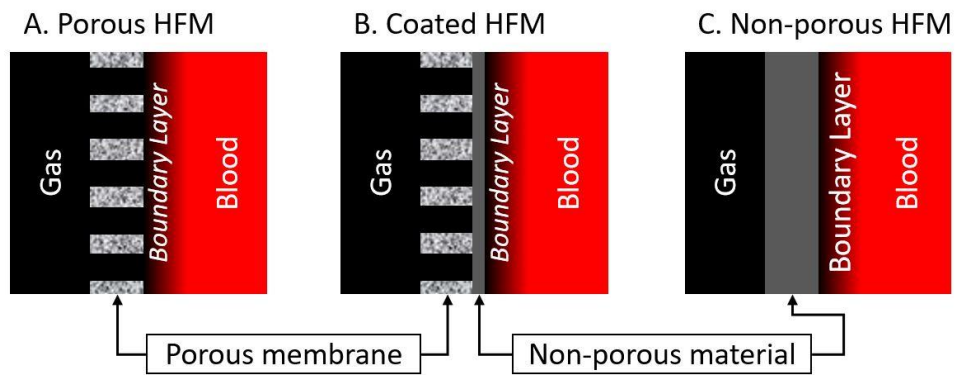


Figure 2: Illustration of (A) porous HFM, (B) Coated HFM, and (C) non-porous HFM in contact with blood.

Porous materials (**Figure 2a**) inherently have high gas permeability and the risk of bubble formation via convective gas transfer limits the sweep gas to sub-atmospheric pressures with their use. Using a porous material with a thin-skinned composite (**Figure**

2b) enhances gas permeability while also limiting plasma leakage or “wetting” into the pores which can diminish efficiency [44]. Nonporous material (**Figure 2c**) allows for high pressure sweep gas to be used safely both because of its increased tensile strength, as well as, the fact that gas transfer occurs solely via diffusion reducing the risk for convective bubble formation. Gas exchange will be greatest when the catheter is in contact with blood that has the lowest oxygen concentration (P_{O_2}), i.e. the venous system. Therefore, such a device should be deployed in a large central vein, ideally spanning the right atrium, to be exposed to the maximum amount of venous return. Finally, previous work has shown incorporating mechanisms to enhance mixing to disrupt laminar blood flow around the catheter, thereby reducing boundary layers, will further increase gas transfer [23], [25], [29], [38], [45]. A proposed hyperbaric catheter bundle developed in this study would could utilize non-porous HFMs and a mixing mechanism to drive oxygen transport as shown in **Figure 3**.

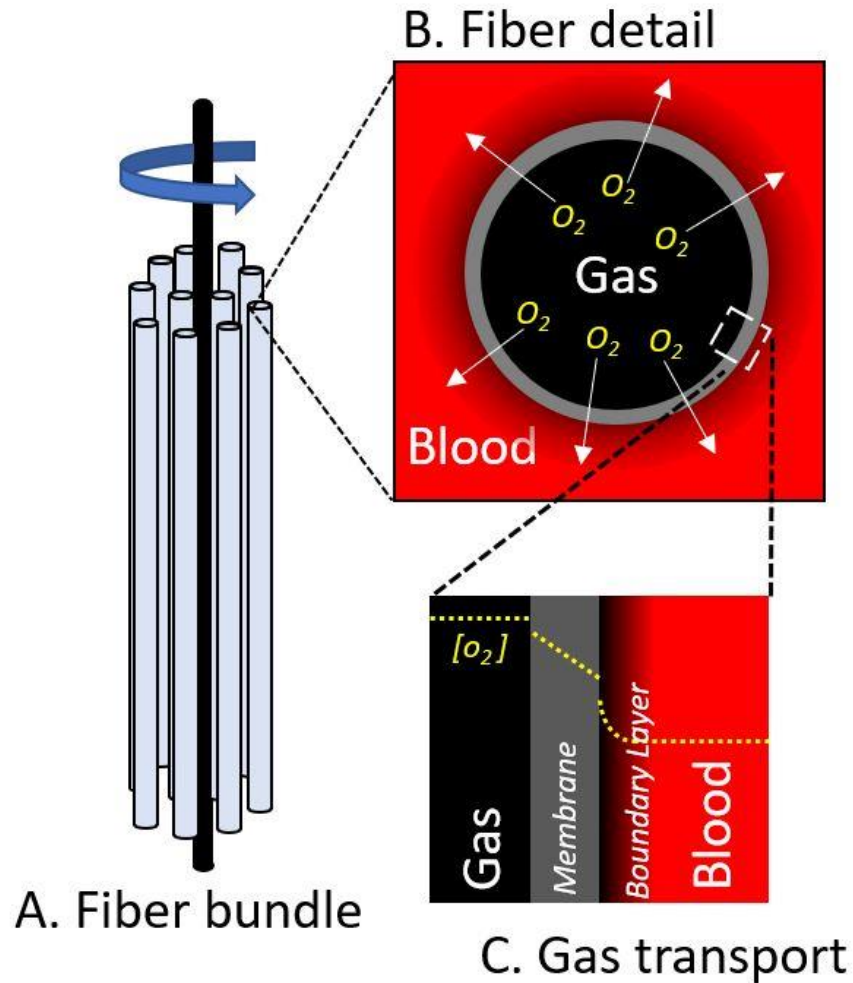


Figure 3: Hypothetical fiber bundle (A) using non-porous HFM to achieve bubbleless (B) oxygenation of blood using the high oxygen gradient of hyperbaric oxygen (C)

1.4.3 Gas exchange requirements

The benefits of an intravascular gas exchange catheter exist on a spectrum dependent on the efficiency of gas exchange coupled with its risk profile. As carbon

dioxide typically has a higher permeability than oxygen, and since previous work has shown it to be an easier gas to remove than oxygen is to add, this study focuses on oxygen delivery as the limiting factor in catheter design. Using the pulmonary shunt fraction equation:

$$\frac{Q_s}{Q_t} = \frac{(C_{CO_2} - C_{aO_2})}{(C_{CO_2} - C_{vO_2})} \quad (1.1)$$

Where Q_s is the blood flow through the shunt, Q_t is the total cardiac output, C_{CO_2} is the pulmonary end capillary oxygen content, C_{aO_2} is the arterial oxygen content, and C_{vO_2} is the mixed venous oxygen content.

We estimate the resultant increase in arterial oxyhemoglobin saturation in varying degrees of lung dysfunction (as modeled by shunt fraction) with the addition of intravascular oxygen to the venous system (**Figure 4**).

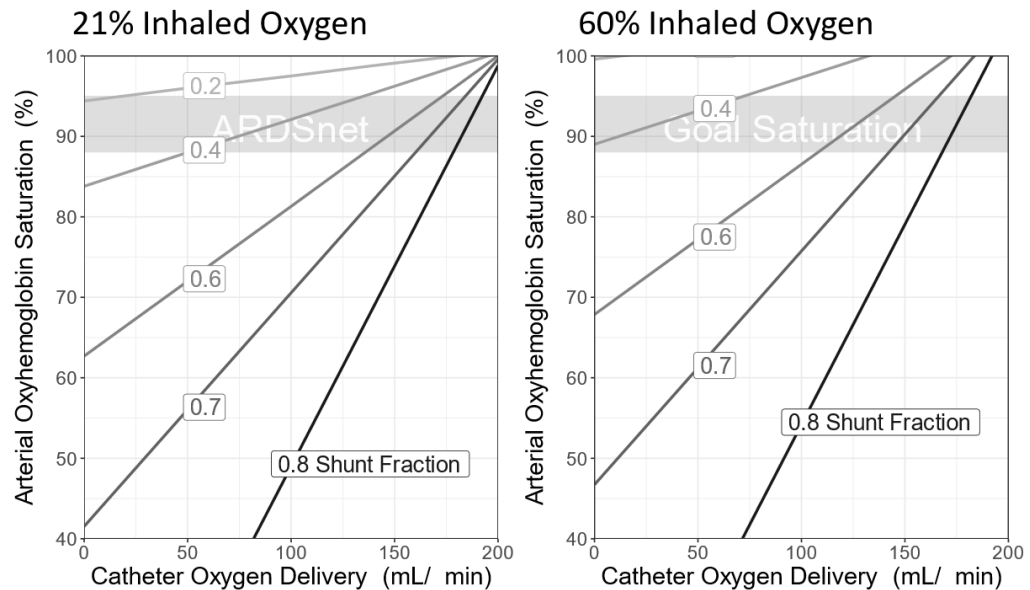


Figure 4: Arterial oxyhemoglobin saturation as a function of theoretical intravascular catheter oxygen delivery. Shunt fractions are used to represent varying degrees of lung disease. A) Patient breathing F_{IO_2} 0.21. B) Patient receiving supplemental oxygen with F_{IO_2} 0.6.

For simplification, we assume a normal adult cardiac output (5 L min^{-1}), hemoglobin (12 g dL^{-1}), and arterial-venous extraction of 25%. In an intravascular venous respiratory assist catheter, the net result of oxygen added by the catheter is an increase in the mixed venous oxygen saturation. A catheter providing $50 \text{ mL O}_2 \text{ min}^{-1}$ would increase the arterial oxygen saturation to 88%, the goal in ARDSnet studies, in a patient breathing room air (F_{IO_2} 0.21, **Figure 4a**) with lung disease represented by a shunt fraction of 0.4 [46]. When combined with supplemental oxygen (F_{IO_2} 0.6, **Figure 4b**) a catheter providing approximately $100 \text{ mL O}_2 \text{ min}^{-1}$ would raise the arterial oxygen saturation to 88% in a patient with more severe lung disease (shunt fraction of 0.6). In patients with lung disease resulting in shunt fractions >0.6 , catheters would need to

deliver $> 150 \text{ mL O}_2 \text{ min}^{-1}$, or be used in conjunction with positive pressure mechanical ventilation to reach target oxyhemoglobin saturation of greater than 88%. Using these examples, we estimate a minimum of approximately $50 \text{ mL O}_2 \text{ min}^{-1}$ is required to be delivered intravascularly for a clinically impactful device. Delivering intravascular oxygen in this amount should allow for decreased reliance on other modes of respiratory support as previously described. This is in line with the previous findings of Conrad et al. who showed the clinical benefits of the IVOX device that delivered 40-70 $\text{mL O}_2 \text{ min}^{-1}$ [16].

The primary objective of this dissertation was to develop the concept of hyperbaric intravascular oxygenation as a future treatment option in patients with ARDs. The work consisted of the development of a proof of concept for a device that is capable of operating at oxygen transfer efficiencies greater than previous works. This is described in Chapter 2, together with a conceptually accurate mathematical model developed to investigate system limitations in the early prototype, and guide future investigations. Mixing methodologies were developed and tested at the bench scale to determine the feasibility of angular oscillation-based mixing on both transport efficiencies and impacts on bubble formation, and the previous model was used to evaluate the system. The results are presented and discussed in Chapter 3. Finally, an investigation on the transport enhancement mechanisms caused by the angular oscillation was conducted using computational fluid dynamics. These results are

presented in Chapter 4. Overall, the work presented in this dissertation provides the foundation for a hyperbaric oxygenation device that should be able to safely operate without bubble formation by using a novel mixing approach.

2. Development of a novel intravascular oxygenator catheter: Oxygen mass transfer properties across nonporous hollow fiber membranes

The following chapter was published in the January 2021 issue of *Biotechnology and Bioengineering* [39]

2.1 Introduction

Hypoxic respiratory failure is a common reason for hospitalization and intensive care unit (ICU) admission for children and adults. A subset of hypoxic respiratory failure resulting from acute lung injury, acute respiratory distress syndrome (ARDS), is present in 7% of patients admitted to ICUs worldwide with a mortality ranging from 34-44% [9], [47], [48]. Despite the prevalence and morbidity associated with hypoxic respiratory failure, treatment options remain relatively few beyond supplemental oxygen and/or traditional mechanical ventilation, which can carry risks. When mechanical ventilation is insufficient, clinicians turn to veno-venous extracorporeal membrane oxygenation (VV-ECMO). ECMO is the only treatment option that delivers oxygen directly to the bloodstream independent of lung function but is associated with adverse events including intracranial hemorrhage, ischemic stroke, acute kidney injury, and infection [12]. ECMO also carries a large economic burden and is only available in specialized centers in developed nations, which greatly limits its use [13], [49]. The need for alternative methods of support for severe hypoxic respiratory failure that function independent of the lungs is becoming evident. This has become particularly apparent at

the time of writing this manuscript as the COVID-19 pandemic progresses worldwide causing hypoxic respiratory failure in those most severely affected. COVID-19 is straining healthcare systems with their limited ability to provide mechanical ventilation and even scarcer capability to offer ECMO.

In this light, novel therapies that can safely deliver oxygen directly into the blood are an attractive option as they may reduce the need for mechanical ventilation and/or ECMO. Such devices ideally would be no more invasive than a large central venous catheter and, more importantly, be equally available to physicians and medics worldwide. Previous groups have attempted direct intravascular oxygenation, though no device has succeeded due to their reliance on a large surface area for oxygen delivery that resulted in bulky catheters that impaired cardiac return [15], [16], [26], [28].

The first and only such intravascular device to reach human clinical trials was the IVOX catheter, which was composed of over 1000 microporous polypropylene hollow fibers coated in siloxane furled together to fit in the vena cava with sub-atmospheric oxygen flowing within. While this device delivered a measurable oxygen amount, its large size (12.6 to 16 mm diameter in furled insertion configuration, containing 0.21 to 0.51 m² of diffusing surface area) was cumbersome and led to a 24.5% clinically recognized complication rate, including bleeding during insertion, thrombophlebitis, and hemodynamic instability [16], [36]. IVOX did not gain FDA approval and device development was halted [50]. Hattler et al. improved upon this

concept with the addition of a balloon pulsating mixing mechanism that allowed a 0.17 m² device to deliver 23.8 mL min⁻¹ of oxygen in water. However, this device still had a 10.6 mm outer diameter in the insertion configuration, and they predicted needing a total of 0.4 m² of HFM diffusing surface area to accomplish their CO₂ clearance and oxygenation goals [15]. These previous attempts at intravascular gas exchange were limited in their oxygen delivery due to their reliance on a large surface area for gas exchange (especially as they were trying to exchange both oxygen and carbon dioxide) which made for large impractical catheters.

In contrast to the previous attempts at intravascular gas exchange, our team is developing an intravascular oxygenator catheter that relies on hyperbaric oxygen to generate a large driving gradient across a non-porous diffusing surface, greatly increasing O₂ transfer, rather than relying on a large surface area. Our device is intended only to deliver oxygen, the primary deficit in most forms of acute lung injury. This approach requires less total HFM surface area and allows for a more compact device amenable to intravascular use, overcoming the challenges faced by previous groups. It is the first intravascular device to use such a method to deliver oxygen. This approach to optimizing oxygen transport from non-porous HFMs into a bulk medium may have many other non-medical applications, such as in biotechnology and wastewater treatment (e.g., bubbleless aeration and membrane aerated bioreactors (MABRs)).

Previous work by Hattler et al. showed that providing approximately 20% of an adult's basal oxygen needs (about 50 mL O₂ min⁻¹) would achieve a life-sustaining arterial oxygen saturation of 90% (P_aO₂ of 60 mmHg) in patients with only 50% of their native lung function intact [15]. Our goal, therefore, is for our device to deliver 25 -100 mL O₂ min⁻¹ (a minimum of 10% of an adult's basal oxygen needs). At this oxygen delivery rate, our device would allow for decreased reliance on mechanical ventilation to support the patient. Conrad et al, demonstrated that delivering 40-70 mL O₂ min⁻¹ with the intravascular respiratory assist catheter, IVOX, allowed for reduction of mechanical ventilation by 25% or more of pre-IVOX insertion levels of intensity in about 50% of their patients [16].

In this work, we report on foundational mass transfer experiments used in the development of our intravascular oxygenation device. Experiments were conducted in-vitro with single and multiple hollow fiber configurations in both a stirred tank vessel (CSTR) and a tubular device mimicking intravenous application to quantify and characterize the rate of oxygen delivery as a function of the operating conditions. The purpose of this study was to develop an analytical model of the oxygen mass transfer via HFMs and validate it through in-vitro experimental testing. Our work indicates that a device capable of delivering greater than 10% of a patient's basal oxygen needs in a configuration that readily fits intravascularly is within reach.

2.2 Materials and Methods

2.2.1 Experimental systems

A schematic of the experimental setup is shown **Figure 5**.

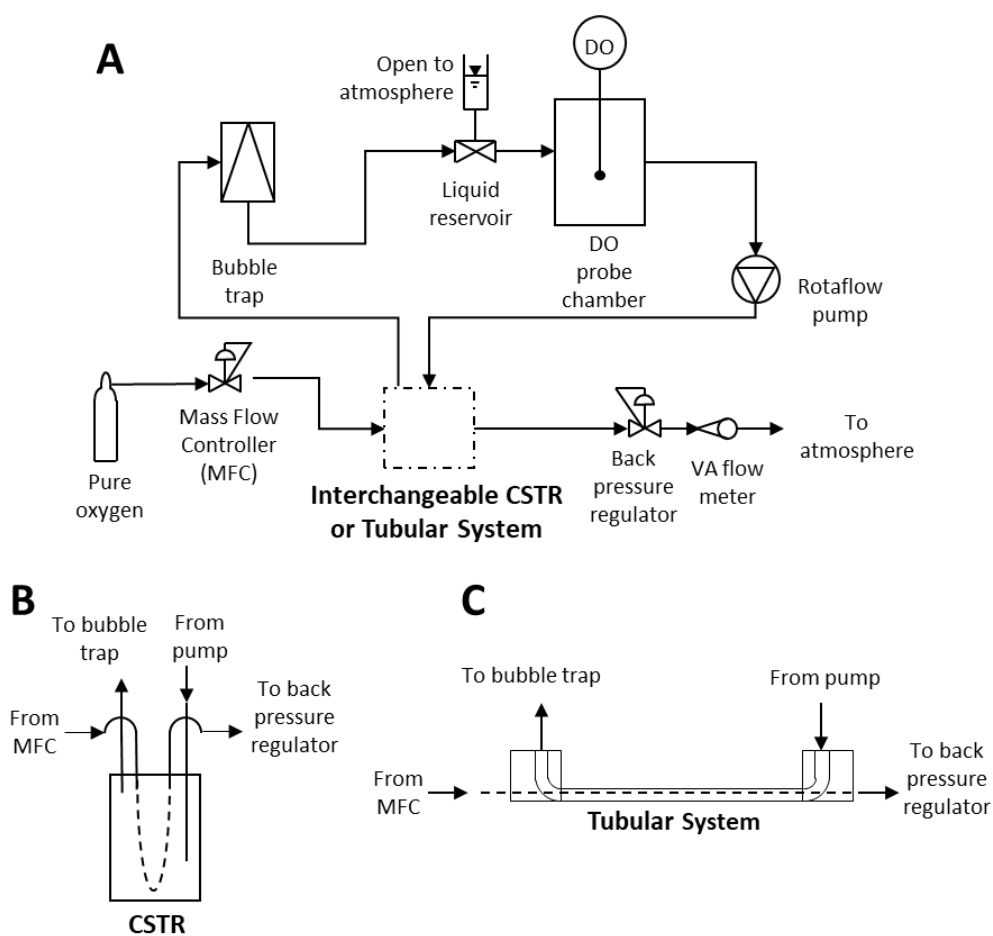


Figure 5: Process schematic of bench top system and instruments. A) System layout showing interchangeable chamber location, B) CSTR chamber detail, C) tubular system detail.

Continuously stirred tank reactor (CSTR) batch systems were constructed using gas tight glass vessels fitted with a single 20 cm fiber. The fibers in this study were made of polytetrafluoroethylene (PTFE); specifically, Teflon AF2400 polymer, chosen for its

high oxygen gas permeability (even higher than PDMS, another polymer commonly used in medical applications, and recently deployed in artificial lung prototypes) of $9.9 \times 10^{-8} \text{ cm}_2 \text{ s}^{-1} \text{ cmHg}^{-1}$, and sufficiently high burst strength (theoretically $> 130 \text{ bar}$) (The Chemours Company, 2016). The membrane used had an outer diameter of $406.4 \text{ }\mu\text{m}$ and a wall thickness of $88.9 \text{ }\mu\text{m}$ (Biogeneral, Inc., San Diego, CA). The oxygen pressure at the inlet of the fiber(s) was controlled using a mass flow controller (MFC) (Alicat Scientific, Tucson, AZ), while a manual backpressure regulator (Airtrol RV-5300-90, New Berlin, WI) regulated the outlet pressure. The fiber(s) effluent was connected to a gas flow meter (Dwyer Instruments, Michigan City, IN) to ensure a minimum outlet oxygen flow (generally about 20 mL min^{-1}), thus avoiding any effects of back diffusion of water vapor and water condensation inside the fibers. The circuit was composed of Tygon tubing with a Rotaflow centrifugal console pump (Getinge AB, Goteborg, Sweden). The CSTR was mixed using a magnetic stirrer at 400 (low speed) and 1200 rpm (high speed). A medical grade gas bubble trap (Terumo Cardiovascular Group, Ann Arbor, MI) was installed after the oxygenator to collect any bubbles that formed during operation prior to the water being recirculated back through the pump. Dissolved oxygen was recorded with an optical DO probe (Vernier, Beaverton, OR) housed in a custom chamber and connected to a data logger. A flush outlet and inline pressure relief reservoir were included in the closed loop to expose the system to atmospheric pressure.

A second series of experiments was conducted in a custom-made tubular chamber with water flowing parallel to the long axis of the fiber(s) to create a counter-current oxygen transfer system (**Figure 5**) mimicking intravascular flow. The acrylic tube was 30 cm in length with a 1.0 cm internal diameter. Different tubular chambers were fitted with 1, 4, and 16 fibers. The closed loop system described above was used for tubular systems by replacing the batch reactor with the appropriate tubular assembly.

2.2.2 Experimental procedure and analytical equipment

All experiments were conducted at room temperature (23-25° C) and atmospheric pressure. The closed loop circuit was flushed with at least 1.5 L of nitrogen sparged water such that the starting dissolved oxygen concentration was 1.5 mg L⁻¹ or less. At this point, oxygen (100% O₂, Airgas, Radnor, PA) was introduced into the fiber(s) at the prescribed pressure (0.24-1.9 bar) and the increase in dissolved oxygen (DO) was monitored using the DO probe connected to a data logger.

2.3 Data analysis

For all experiments, the oxygen transfer flux was calculated as the total mass of the oxygen transferred to the liquid between two data points, while the dissolved oxygen concentration at which this flux occurred was taken as the average between the two points. A moving average was used to smooth each dissolved oxygen time series; 5 sample points (50 to 75 seconds span) were used for experiments conducted with the tubular systems and 9 sample points (90 to 135 seconds span) for those with the CSTRs.

Each pressure and flow combination tested was conducted in triplicate for tubular systems and duplicate for CSTRs. A linear regression with confidence intervals of 95% for the true mean was used to calculate the average flux at a given bulk water gas partial pressure for oxygen over the range of 30 to 100 mmHg.

2.3.1 Ultrasound bubble detection

As a complement to measurements of dissolved oxygen, bubble formation was studied downstream of the prototype oxygenators using high frequency ultrasound imaging. A Vantage 256 research scanner (Verasonics Inc., Kirkland, WA) was used with the L22-14 linear array (Vermon S.A., Tours, France) to perform high frame rate imaging through a CDI blood parameter monitoring acrylic 3/8 inch cuvette (Terumo Cardiovascular Group, Ann Arbor, MI) to directly detect the presence of gas bubbles. Plane wave transmissions[51] with a center frequency of 18 MHz were performed in a tubular system at 0.24 bar average fiber pressure and 2 L min⁻¹ flow rate. First, the imaging plane was aligned along the direction of flow, and high-resolution imaging was performed (five plane waves steered at -8 to 8 degrees in 4-degree increments) at 4 kHz frame rate for 100 milliseconds. Second, the imaging plane was placed in cross-section of the flow and high-speed imaging was performed (a single plane wave) at 20 kHz for 100 milliseconds. In both cases, channel data sets were acquired for offline processing at approximately 5-minute intervals for the duration of the experiments.

Gas bubbles were detected in the image frames using automated bubble counting after suppression of background noise using spatial coherence beamforming. We performed mid-lag spatial coherence processing[52] to remove specular reflection and to isolate air bubbles from background and noise. Bubbles were identified in individual frames using thresholding and blob analysis. Identified bubbles from each frame were paired through time to fit a motion model and provide an estimate of unique bubbles observed during each observation period.

2.3.2 Model development

A conceptually accurate dynamic model describing oxygen mass transfer in our experimental systems was developed. The model assumes that Fick's first law applies for oxygen flux across the membrane wall via diffusion, while convective mass transport occurs from the outer surface of the membrane into the bulk liquid (**Figure 6**). Partial differential equations were written describing the transport of oxygen and were then solved numerically.

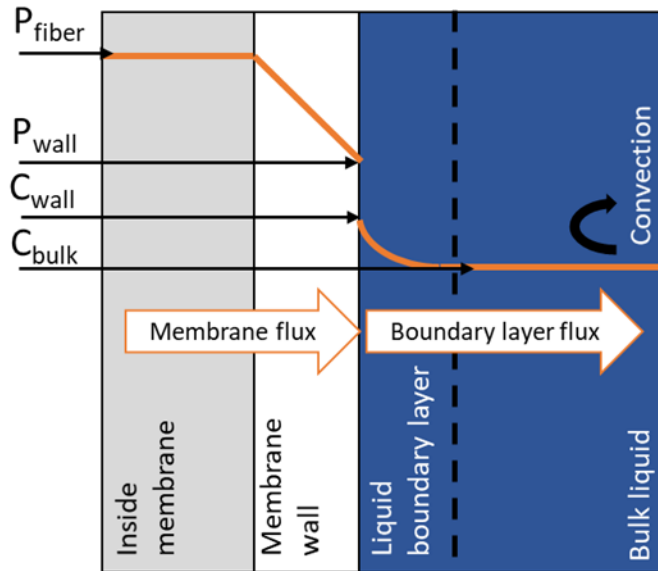


Figure 6: Conceptual model of the membrane interfaces with high pressure oxygen inside the fiber, diffusion through the non-porous membrane, liquid boundary layer, and bulk liquid. See SI [Appendix A] for detailed model equations.

For device modeling purposes, the liquid in the stirred batch systems was assumed to be ideally mixed (which was verified experimentally), whereas spatial discretization for the liquid was applied along the axial direction for the tubular systems to account for the axial gradient of DO and its effect on the transfer flux. Tubular system models were discretized in the direction of flow only; no gradient was assumed in the liquid along the radial direction (except for the boundary layer). In both CSTR and tubular models, the fiber was discretized along the axial direction with the partial pressure inside the fiber (P_{fiber}) assumed to drop in a linear fashion from the inlet, as set by the MFC, to the outlet, as set by a back-pressure regulator. The partial pressure of oxygen (P_{wall}) at the membrane-liquid interface was calculated using the Henry's

constant for oxygen and solving a mass balance at the interface (Equations 1 - 4 in SI). Because the fibers are continuously purged using low humidity 100% oxygen, the impacts of any back diffusion (e.g., of CO₂ or water vapor leading to condensation) into the HFMs is estimated to be negligible. Additionally, previous authors have shown that the effects of back diffusion on closed end fibers used for bubbleless aeration were negated with relatively short venting periods (20 s every 30 min)[53]. Detailed model equations can be found in SI.

The model also incorporated intrusion of small amounts of oxygen from the atmosphere into the system by diffusion occurring through the Tygon circuit tubing (determined separately in independent experiments) which was relevant, especially for experiments at low fluxes, i.e., those with low membrane surface area and low pressures. This oxygen intrusion into the system was removed for all sensitivity analyses.

The partial differential equations were solved numerically using a Runge-Kutta 4th order algorithm. Model parameters (**Table 2**) included both physical constants taken from the literature and system specific parameters. The latter were determined experimentally. In particular, the model was fit to the DO time series (see Results section) using the mass transfer coefficient of the liquid boundary layer (k_{boundary}) as the fitting parameter. Sensitivity analyses were conducted with each model on the CSTR

and tubular systems while maintaining a constant pressure along the fiber length (i.e., no pressure drop inside fiber).

Table 2: Model parameters used in this study.

Parameter	Value	Unit	Source
Fiber length	CSTR: 20	cm	Measured
	Tubular:30*	cm	Measured
Fiber inner diameter	228.6	μm	Manufacturer
Fiber wall thickness	88.9	μm	Manufacturer
Fiber O ₂ permeability	9.9×10 ⁻⁸	cm ² s ⁻¹	Manufacturer[54]
		cmHg ⁻¹	
Convective mass transfer coefficient	CSTR#: 9.54 x10 ⁻³ , 1.45	cm s ⁻¹	Fitted to experiment
	x10 ⁻²		
	Tubular#: 3.65x10 ⁻³ ,	cm s ⁻¹	Fitted to experiment
	6.42 x10 ⁻³		
Number of discrete fiber elements	CSTR: 11	-	Assumed
	Tubular: 30	-	Assumed
Circuit flow rate	CSTR: 0.5	L min ⁻¹	Measured
	Tubular: 0.5 - 2.0	L min ⁻¹	Measured
Oxygen pressure range	0.24 - 1.9	bar	Measured, independent parameter

* Tubular devices length varies slightly (31-33 cm) between the different units.

#400 and 1200rpm,

¥0.5 and 2.0 L min⁻¹, respectively.

2.4 Results and Discussion

2.4.1 Oxygen transfer: time series and fluxes

Selected time series for oxygen transfer are reported in Figure 3. They show a typical saturation behavior (Figure 3 inset) caused by the decrease of the DO gradient over time as DO in the liquid increases. Comparison of the different curves in **Figure 7** reveals that oxygen transfer is limited by both the gradient across the fiber (DO increase is faster at 1.9 bar vs. 0.24 bar) as well mixing in the system (DO increase is faster at 1200 rpm vs. 400 rpm mixing). Note that the tubular system shown in Figure 3 cannot be directly compared to the CSTR since the devices have different fiber lengths (20 cm for the CSTR vs. 32.4 cm for the tubular device shown). To conduct a direct comparison, calculation of the oxygen transfer flux is needed. These results are shown in **Figure 8** where the instantaneous oxygen transfer flux is reported as a function of the partial pressure of oxygen in the liquid during selected experiments.

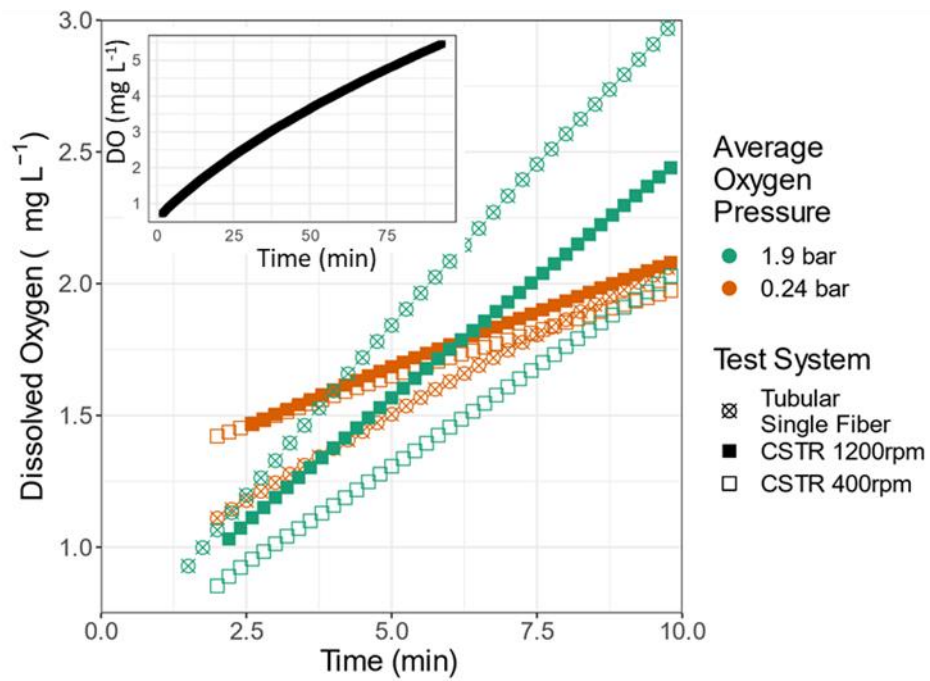


Figure 7: Time series of dissolved oxygen for single fiber tubular device (30 cm fiber) and CSTRs (20 cm fiber) at two different average oxygen pressures. The inset shows an extended time scale run for a select tubular single fiber illustrating decreased transfer as oxygen saturation increases.

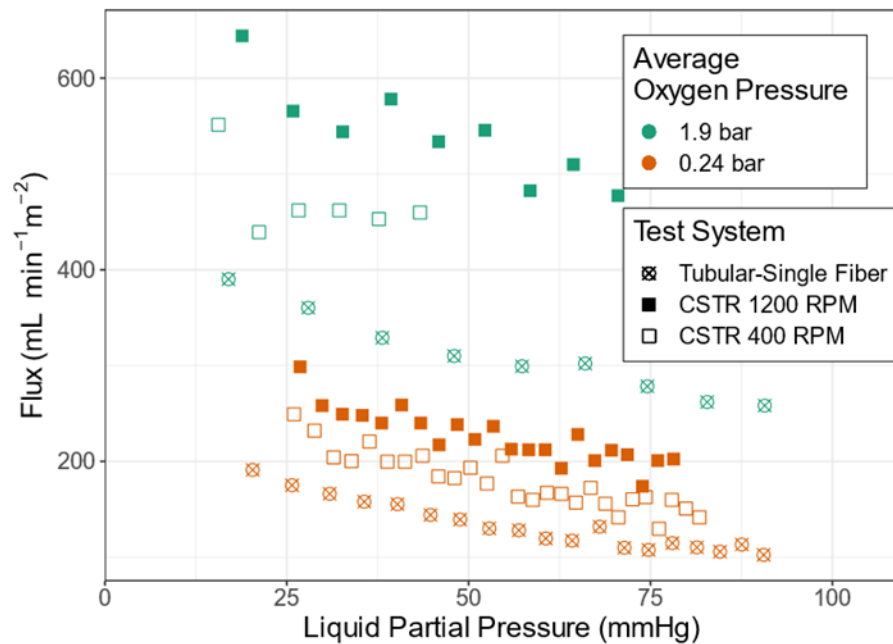


Figure 8: Subset of instantaneous oxygen flux vs. liquid partial pressure of oxygen for the selected single fiber CSTR and tubular experiments shown in Figure 7.

Overall, high oxygen fluxes were observed compared to earlier reports of related devices, even in the tubular device at lower water flows[15], [23]. The general trend downwards in **Figure 8** was expected, caused by the decrease in the driving force for oxygen transfer as the liquid DO increases. The tubular device was less performant than the CSTR, since the parallel flow fiber orientation with no additional mixing mechanism resulted in greater resistance to oxygen transfer. However, the results show that increasing the system pressure within the fiber could greatly improve oxygen transfer, consistent with our hypothesis that hyperbaric conditions are a possible means to achieve physiologically relevant oxygenation rates in a compact device.

Summaries of all fluxes at physiologically relevant liquid partial pressures of oxygen are shown in **Figures 9** and **10** for the CSTR and tubular systems, respectively. CSTR results in **Figure 9** show the potential for very high fluxes using the non-porous fibers when external mass transfer is not a limiting factor (1200 rpm mixing). In the low mixing CSTR (400 rpm), results show small decrease in flux at times as the pressure increases. This is likely caused by fiber touching the glass vessel wall during low mixing as the pressure within the fiber increased. Another possibility is the supersaturation of water with oxygen at the outer surface of the HFM during low mixing leading to formation of small oxygen bubbles on the fibers and a decrease in the overall transfer. The effect of bubbles on oxygen transfer remains to be defined and is further discussed below. Regardless, the fluxes in the CSTR remained higher than in the tubular systems. For the tubular systems, examination of **Figure 10** reveals that increasing the fiber density from one fiber to four, and from four fibers to sixteen resulted in a slight decrease in the flux. This is likely due to a combination of fiber to fiber touching (thus reducing area for transfer), as well as local oxygen gradients being lower within the bundle of fibers (gradients overlapping). Well mixed CSTRs (**Figure 9**) had higher fluxes than all tubular devices at the same system pressures due to higher mixing rates increasing the convective mass transfer coefficient.

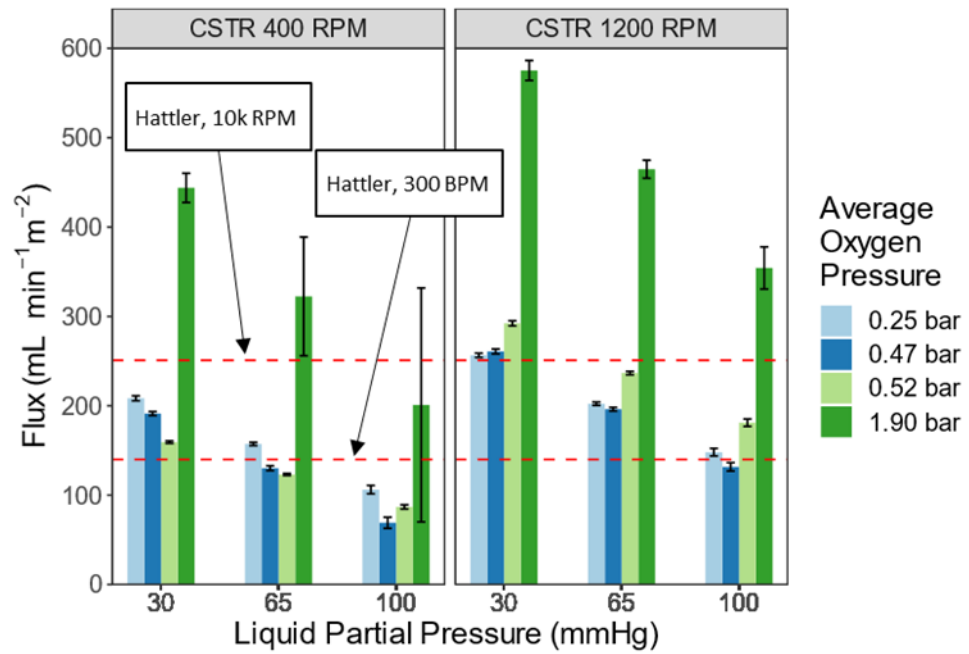


Figure 9: Experimentally determined fluxes at select liquid partial pressures for CSTR systems. Dashed lines show highest flux efficiency achieved by previous authors with extreme mixing (10,000 rpm) and more modest pulsing methods (300 BPM).

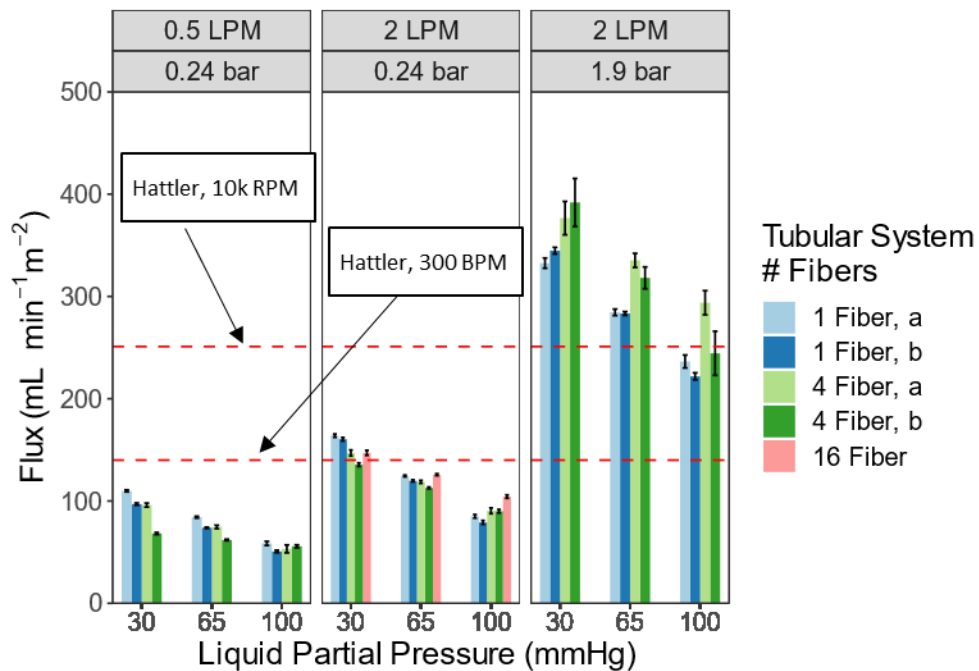


Figure 10: Experimentally determined flux at select liquid partial pressures for tubular devices (a and b are replicate experiments). Low flow high pressure (0.5 L min⁻¹ at 1.9 bar) was not included due to bubble formation in system. Dashed lines show highest flux efficiency achieved by previous authors with extreme mixing (10k rpm) and more modest pulsing methods (300 BPM).

As mentioned, the fluxes observed in both the CSTR and tubular systems are significantly higher than those reported by previous groups [25], [26], [28], [55], [56] who developed devices for intravascular gas exchange, including Hattler et al. whose team designed and tested some of the most efficient devices to date. The Hattler catheter systems relied on oxygen pulled through porous polypropylene membranes by a vacuum, remaining at sub-atmospheric pressures, with a variety of mixing mechanisms included to improve mass transfer. Figure 5 and 6 include two benchmarks, 140 [15] and 251 [23] mL min⁻¹ m⁻² flux, representing a device with a balloon rapidly

inflating/deflating at 300 beats per minute (BPM) and their other device with fibers rotating up to 10,000 rpm respectively. These comparisons illustrate that non-porous hollow fiber membranes (which allow for hyperbaric oxygen flowing within) can achieve greater fluxes than previously obtained with porous fibers that require low (and even sub-atmospheric) pressure oxygen to be used to prevent convective flux of gaseous oxygen and bubble formation.

2.4.2. Bubble investigations

It is well known that large vascular air emboli (bubbles) cause significant morbidity, such as cardiovascular collapse if venous gas migrates to the pulmonary circulation, or tissue ischemia and necrosis if gas is lodged in the arterial vessels. However, the impacts of air micro-emboli, particularly pure oxygen micro-emboli, are not well understood. To our knowledge, no studies have examined the effect of pure oxygen gas micro-emboli in vivo, with only some case studies of large oxygen gas emboli with varying degrees of morbidity[41], [57]. At the conditions reported herein, bubbles were only observed visually on some fibers when one of the following occurred: 1) two or more fibers were touching in the multifiber cartridges, 2) the high pressure (1.9 bar) was used, 3) when low water flow (0.5 L min^{-1}) was used in the tubular system (which inherently has less mixing), 4) when the bulk liquid DO was higher than $>2 \text{ mg L}^{-1}$.

These observations serve as the foundation as we develop prototype devices and define safe operating parameters for our system. Our experiments show that future prototypes will require HFM spacing such that fiber-fiber interactions are accounted for, and limited as is feasible, which will reduce bubble risks and allow for higher operational pressures. Periodic fiber movement, bulk mixing, or even fiber physical features or coatings in key areas are potential ways to limit the areas of highest fiber-fiber interaction (such as the beginning and end of the fiber bundles). Additionally, methods to enhance mixing in and around the fibers will be required not only to further increase oxygen flux, but also to enhance convective transfer of oxygen to the bulk liquid to reduce bubble formation. Finally, the bubbles seen with experiments performed at 1.9 bar show that enhanced mixing of the bulk and/or reduction of nucleation sites during higher oxygen fluxes may be an important improvement of future prototypes to ensure safe operation. However, it is likely that pure oxygen in small bubbles would be quickly bound by hemoglobin or metabolically consumed.

Beyond direct (visual) observation of bubbles, a proof-of-concept of high frequency ultrasound imaging for bubble detection was conducted during testing of the tubular system. Results are reported for one condition (tubular device, 2.0 L min⁻¹ and 0.24 bar) in **Figure 10**. They revealed the presence of a low concentration of small bubbles in the experimental circuit at baseline even before the introduction of oxygen (**Figure 11**). Further, bubble counts remained below the maximum baseline in all but one

data point during the hyperbaric oxygenation (**Figure 11B**). Videos of bubble tracking and their motion are shown in SI [**Appendix A**]. They show our ability to track and quantify bubbles in real time. A ~3 mL bubble was released into the circuit (not from the HFM) and broken down into smaller bubbles by the circulation pump resulting in a clear increase in the bubbles detected by ultrasound prior to being caught in the bubble trap. This served as a positive control for bubble detection. This ultrasound work confirms the delivery of oxygen from the HFM is solely possible via dissolved oxygen rather than through nucleated bubbles under select hyperbaric conditions. Secondly, this demonstrates that our bubble quantification method provides a quantitative means to monitor bubbles in future experiments especially in in-vitro blood testing where direct bubble visualization in the system will be difficult given the opaque nature of blood.

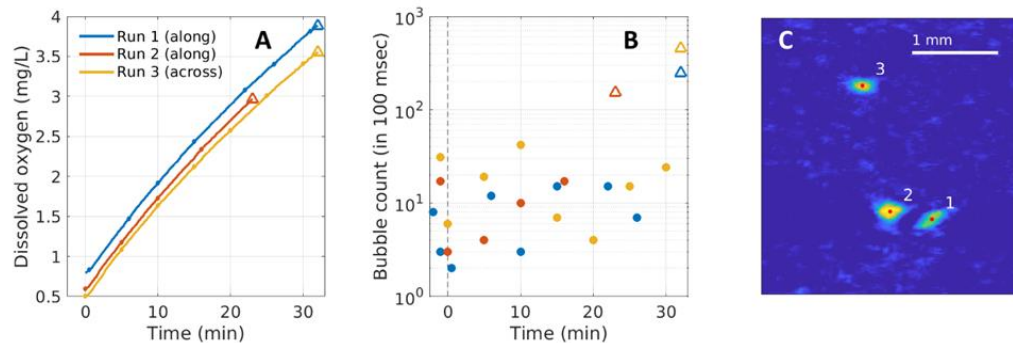


Figure 11: Experimental observation of gas bubbles in the tubular device using ultrasounds. A) DO evolution vs. time during the test runs (2.0 L min^{-1} 0.24 bar). Markers indicate times for ultrasound bubble assessment. B) Unique bubbles counted within 100 ms sampling window. Baseline prior to oxygenation shown at time <0 . Positive control of bubble detection shown at end of each run (triangle symbols). C) Sample image after non-linear coherence processing with three identified bubbles.

2.4.3 Modeling oxygen transfer in the devices and model parametric sensitivity

The conceptual model of the device was used to determine the convective mass transfer coefficients for the CSTR and tubular systems. A set of replicate runs was used in each case (CSTR 400 rpm, CSTR 1200 rpm, tubular device 0.5 and 2 L min⁻¹), and the model was fitted to the experimental DO data with the mass transfer coefficient k as the fitted parameter and averaged across the replicates. The mass transfer coefficients values obtained were 9.54×10^{-3} and 1.45×10^{-2} for the CSTR at 400 rpm and 1200 rpm, respectively and 3.65×10^{-3} and 6.42×10^{-3} cm s⁻¹ for the tubular device at 0.5 and 2 L min⁻¹, respectively. These values illustrate the impacts of external transport and the fact that the tubular device was subject to more external mass transfer limitations than the CSTR. **Figure 12A** and **12C** demonstrate the model fit to a single replicate condition. The fitted k values were then used to predict DO time series for other pressure conditions (**Figure 12B** and **12D**). The results illustrate the model predictability for select CSTR and tubular experiments, showing good match with the experimental data especially below 3 mg L⁻¹ which is most physiologically relevant. However, the model did not predict the 400 rpm CSTR well. The poor fit for the 400 rpm CSTR is potentially the result of external forces providing oxygen to the system not taken into account in the model, which is magnified under low total oxygen flux into the system. The other conditions tested had higher total oxygen transfer from HFMs, thus reducing this impact.

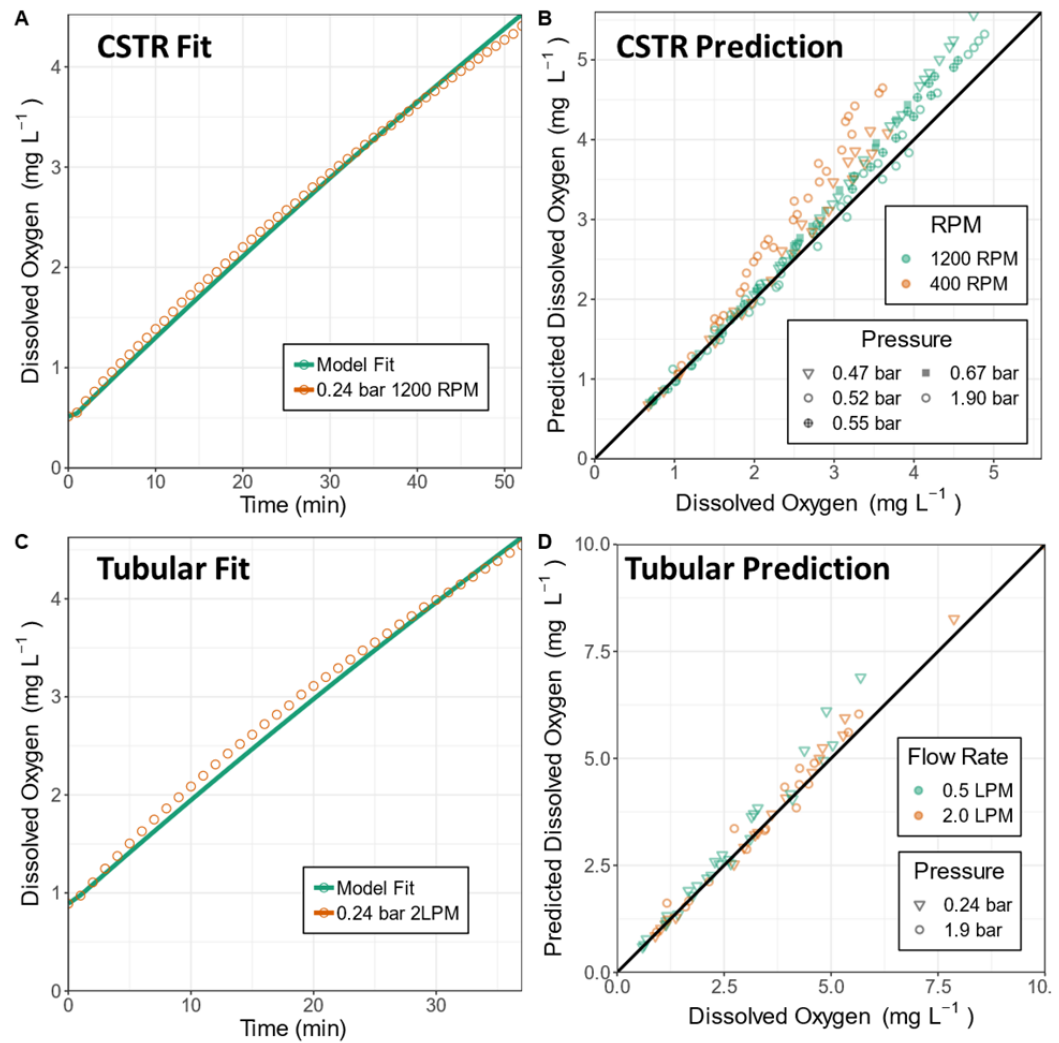


Figure 12: Model fitting for the convective mass transfer coefficient for the CSTR (A) and the tubular device (C) for a single replicate, and model predictions vs. experimental data for experiments with the CSTR (B) and tubular device (D). Figures B and D use a fraction of the total data set to increase clarity. Model fitting used replicates of 0.24 bar experiments to find an average k value (one set of CSTR and tubular) for each mixing scenario (400/1200 rpm and 0.5/2.0 L min⁻¹). Figures for the 400 rpm and 0.5 L min⁻¹ fit are provided in SI.

The sensitivity of the model to key parameters was investigated next. **Figure 13** reports the sensitivity of both the CSTR (A) and tubular (B) systems to changes in the convective mass transfer coefficient (k) for lumen pressures ranging from 0.25 to 2 bar of

oxygen. Examination of the results highlights the different mass transfer limitation regimes. At low k values, the oxygen flux is sensitive to increases in k , an indication that external mass transfer is in part limiting, and that mixing will increase the oxygen flux. On the other hand, at high k values, the flux becomes independent to k values, as oxygen transport is primarily limited by diffusion through the membrane. For all conditions, as expected, the flux increases with increases in pressure, as it increases the overall driving force for oxygen transfer. The vertical bars in **Figure 13** indicate the nominal values for the actual experiments. They highlight that all the systems tested would benefit from greater mixing. The difference between the CSTR and tubular systems sensitivity was not discernable. This is because the DO increase along the tubular device remains relatively low, thus that the impact of the axial decrease of the oxygen gradient driving the transfer is insignificant for single fiber systems.

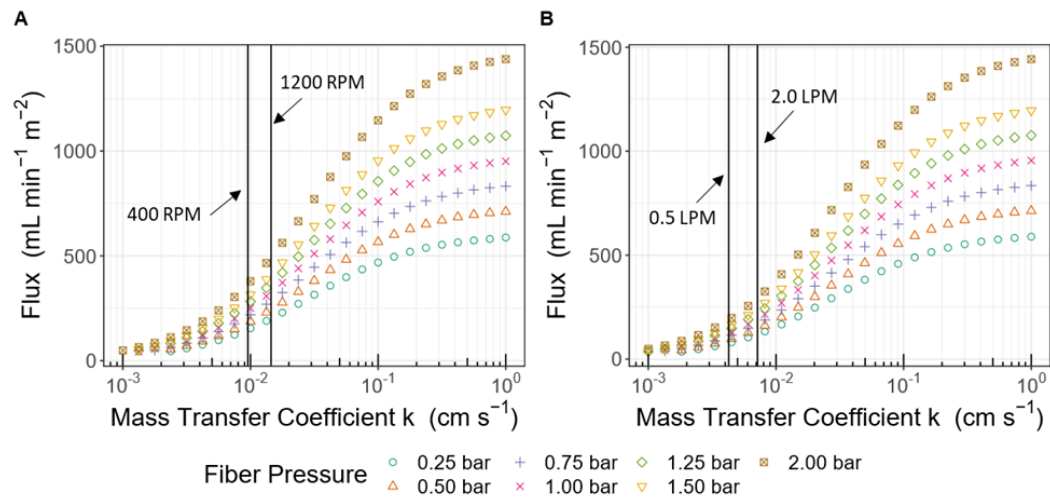


Figure 13: Sensitivity of instantaneous oxygen flux to the mass transfer coefficient k and to membrane oxygen pressure. The reported fluxes are for a bulk (CSTR) or outlet liquid (tubular) partial pressure of 30 mmHg. The fiber length was set to 30 cm in both cases while pressure inside the fiber was held constant across the entire length. Vertical lines represent actual mass transfer coefficients for CSTR (A) and tubular (B) systems at fitted rpm or flow rate. Note the log scale for the x axis.

Figure 14 illustrates the potential benefits of reducing membrane wall thickness for various convective mass transfer conditions ($k = 0.001$ to 0.1 cm s^{-1}). As expected, when the external mass transfer becomes less limiting (higher k values), reducing the wall thickness has a greater impact on the system flux. Conversely, for thick membranes ($>70 \text{ }\mu\text{m}$), the resistance to transport is higher in the membrane than liquid boundary layer, and the impacts of k are limited. This figure also shows that there will be significant benefits to decrease the membrane thickness in the current prototypes.

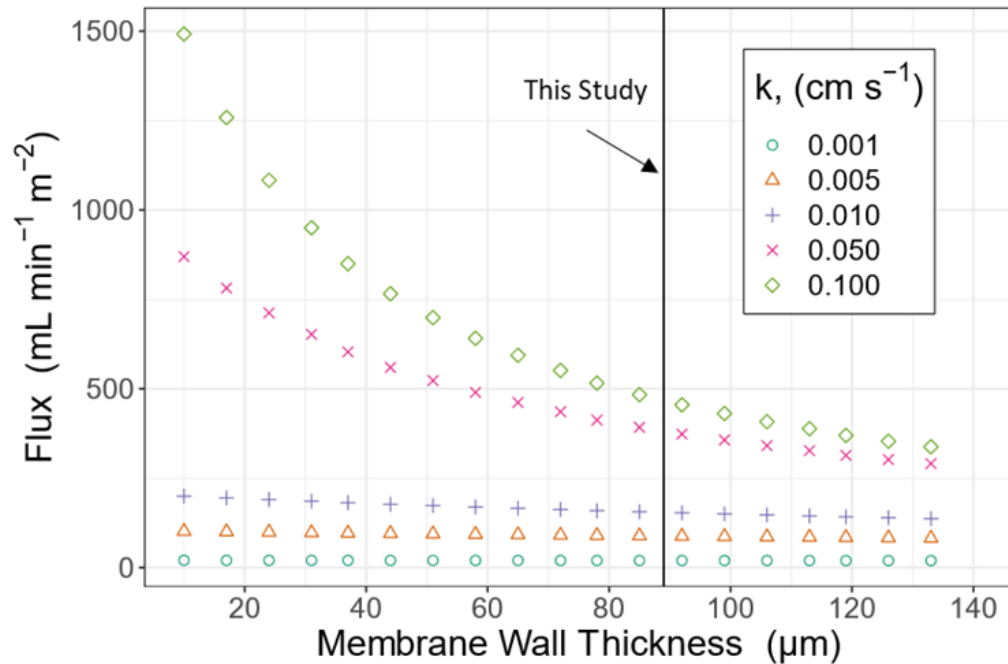


Figure 14: Sensitivity of instantaneous flux to membrane wall thickness of the CSTR model and to the convective mass transfer coefficient (0.001 to 0.1 cm s⁻¹) at a bulk liquid partial pressure of 30 mmHg. The fiber oxygen pressure was held constant across the length of fiber at 0.25 bar. Actual membrane wall thickness of prototypes was 89 μm (vertical bar).

The sensitivity of oxygen transfer to the membrane material permeability to oxygen is reported in **Figure 15**. The material used in this work was Teflon AF 2400, which has one of the highest permeabilities to oxygen. Thus, limited increases can be expected, although **Figure 15** shows that improvements to permeability would result in much greater oxygen fluxes when convective transport is high. Altogether, **Figure 14** and **15** show that the total resistance to mass transfer from the membrane will be a key factor in sizing intravascular oxygenation devices. In particular lowering of the

membrane wall thickness will both increase the flux across the fiber as well as reduce the total volume of fibers required to achieve a target oxygen flow.

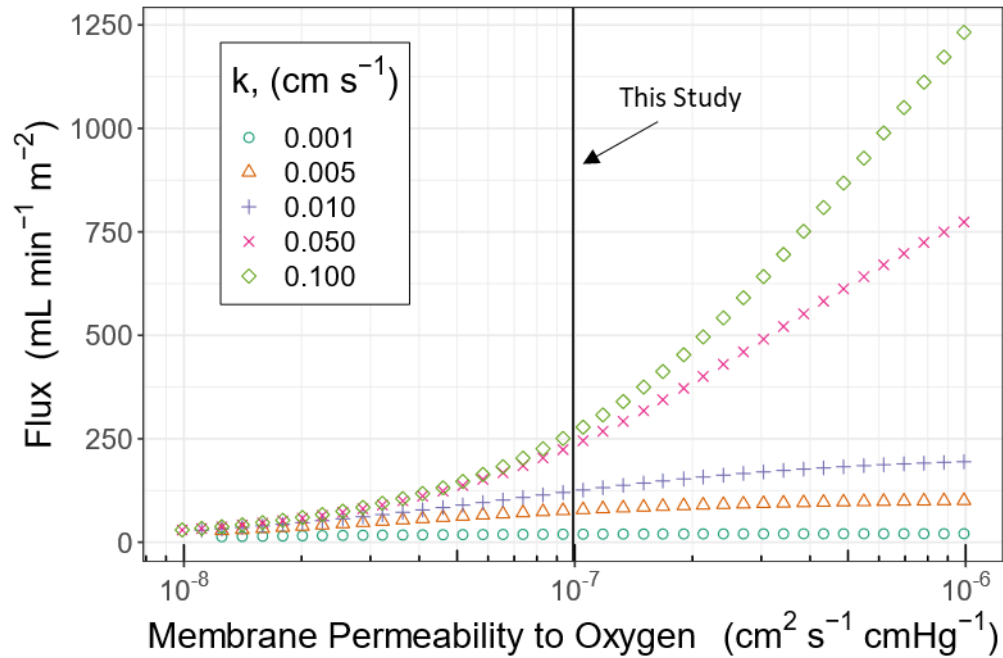


Figure 15: Sensitivity of instantaneous flux to membrane permeability of the CSTR model and to the convective mass transfer coefficient (0.001 to 0.1 cm s⁻¹) at a bulk liquid partial pressure of 30 mmHg. The fiber oxygen pressure was held constant across the length of fiber at 0.25 bar and membrane thickness was 89 μm. The vertical bar shows the permeability of the Teflon AF 2400 membrane (9.9 × 10⁻⁸ cm² s⁻¹ cm-1Hg).

Finally, we used the model to determine if a device using high pressure oxygen could potentially achieve physiologically relevant levels of oxygen transfer, while maintaining low total surface area. **Figure 16** shows two contour plots reporting the total system oxygen transfer rate at 30 mmHg oxygen partial pressure in water, over a range of membrane surface area and lumen pressure. At a low mass transfer coefficient

(tubular system value used), representing low mixing, oxygen transfer rates as high as 35 mL min⁻¹ are predicted while staying under 0.15 m² total surface area and below 2.0 bar of oxygen pressure (A). A hypothetical increase in the mass transfer coefficient by 10 times by a simulated increase in mixing more than triples that to over 100 mL min⁻¹. These model results show the potential of introducing hyperbaric oxygen through non-porous HFM as a means to deliver a clinically significant amount of oxygen. This novel approach to intravascular oxygenation allows for a more compact device with higher oxygen transfer rates when compared to previous works.

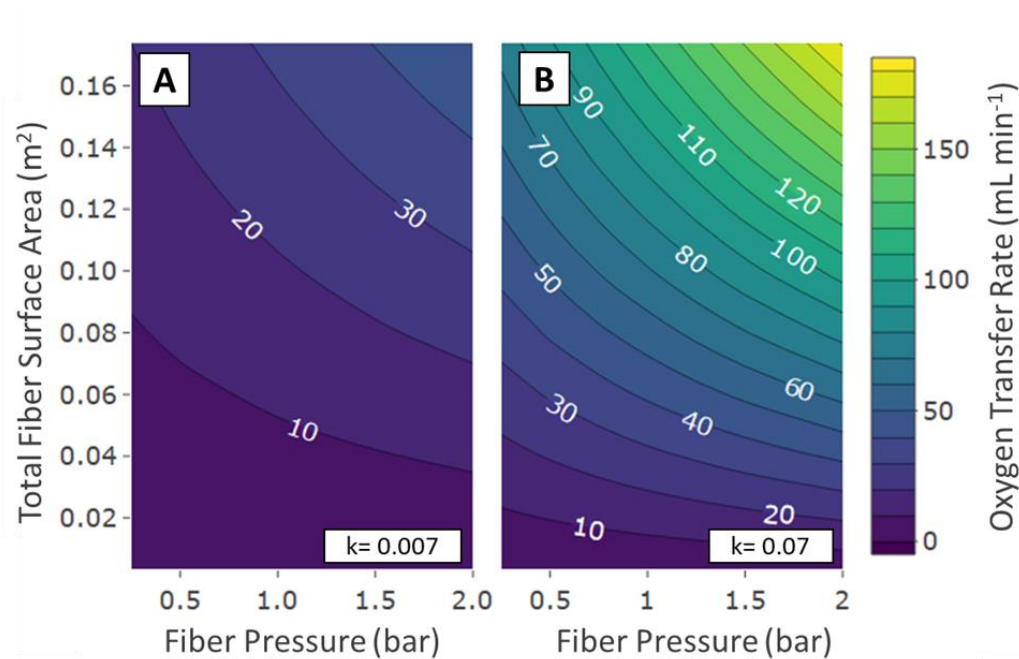


Figure 16: Contour plot for total oxygen transfer rate as a function of pressure and total fiber area, for two different mass transfer coefficients (k). A) k value for fitted tubular system at 2 L min⁻¹. B) 10-fold increase simulating significant increased mixing.

2.5 Conclusions

Alternative treatments for hypoxic respiratory failure that function independently of the lungs are clearly needed. This has become more apparent with the worldwide COVID-19 pandemic which has overwhelmed ICUs around the world. An inexpensive, easy to deploy device that provides oxygen directly to the bloodstream, augmenting mechanical ventilation and possibly reducing the need for ECMO, would find broad and immediate use in a variety of clinical settings.

The work presented here describes fundamental engineering research in support of such a device which could be deployed intravascularly and provide a portion of a patient's oxygen needs irrespective of the degree of lung injury. High oxygen fluxes were observed with our non-porous membrane devices reaching over $550 \text{ mL min}^{-1} \text{ m}^{-2}$ under hyperbaric oxygen supply. The work presented here demonstrates that operation under hyperbaric conditions allowed us to achieve oxygen fluxes greater than any previous work. Experiments showed that factors limiting the transfer of oxygen were both internal (diffusion through the membrane) and external (convection around the fibers). The amount to which these factors affected flux could be captured in a conceptually correct analytical model of the system. The model facilitated the conduct of a sensitivity analysis on the system and was used in a predictive fashion to determine the surface area required for a clinically meaningful device. Sensitivity analyses to model parameters showed differentiation between key mass transfer regimes and

demonstrated that such a system will need significant mixing to take advantage of higher oxygen pressures. Our model predicts this approach has potential to deliver significant amounts of oxygen in a device that readily fits intravascularly. As we scale up, it can be expected that the membrane efficiencies will decrease as surface area increases though the system will be able to compensate for some amount of this lost efficiency by increasing oxygen pressure. We show that an important limitation in any intravascular oxygenation device that achieves such high fluxes is the risk of bubble formation, which will ultimately limit the maximum pressure at which a device could safely operate and, therefore, limit the upper bounds of safe oxygen transfer. These studies constitute the foundation for a new generation of intravascular oxygenation devices which could supply clinically significant amounts of oxygen to patients with hypoxic respiratory failure by overcoming mass transfer limitations with the use of hyperbaric pure oxygen flowing through non-porous hollow fiber membranes

3. Oxygenation Catheter mixing via angular oscillation

3.1 Introduction

Acute Respiratory Distress Syndrome (ARDS), a form of acute lung injury resulting in hypoxic respiratory failure is a frequent and often lethal indication for admission to both adult and pediatric intensive care units (ICUs). Prior to the current COVID-19 pandemic, ARDS was present in 7% of adult ICU patients and represented 1-10% of pediatric ICU (PICU) admissions [6]–[9]. However, due to the COVID-19 pandemic, the incidence of ARDS is much higher [10], [11]. Despite the prevalence, morbidity, and mortality related to ARDS, the treatment options remain relatively few beyond conventional mechanical ventilation. When mechanical ventilation fails to adequately oxygenate patients with ARDS, clinicians may turn to veno-venous extracorporeal membrane oxygenation (VV-ECMO). VV-ECMO is the only available therapy that directly oxygenates blood independent of the lungs and, therefore, is capable of fully supporting a patient regardless of degree of lung injury. Unfortunately, VV-ECMO is associated with many potentially serious complications including hemorrhage, thrombosis, infection, and end-organ injury [12]. VV-ECMO is only available in approximately 3% of hospitals in the United States,8 and even less worldwide. The complexity of VV- ECMO, its associated morbidity, and limited availability lessen the benefits of this life-saving technology. There is an urgent need for

alternative technologies that support patients with severe hypoxic respiratory failure that function independently of diseased lungs.

To address this need, previous groups attempted to develop respiratory assist catheters capable of providing intravascular gas exchange. However, none of them proved successful due to their reliance on large gas exchanging surface areas resulting in bulky catheters [14], [15], [28], [37]. The only such device to make it to human clinical trials was the IVOX device, a large catheter (insertional diameter of 1.3-1.6 cm) composed of many porous polypropylene hollow fiber membranes (HFMs) bundled together (totaling 2,100 to 5,000 cm²) with sub-atmospheric oxygen pulled through their lumens by vacuum [14], [17].

Previous work has also used active mixing methods to increase the oxygen flux of their devices by incorporating various mechanisms to enhance mixing of the blood through their HFM bundle with varying degrees of success [15], [24]–[26], [37]. Hattler and colleagues showed that incorporating a pumping balloon within their bundle of porous HFMs increased the gas exchange by 30 -40% when it was tested in a large animal model [15]. By spinning their densely packed HFM bundle up to 12,000 RPM, Hattler's team was able to further increase their oxygen flux up to threefold in benchtop studies, achieving as high as 370 mL O₂ min⁻¹ m⁻² [37]. These works highlighted the importance of incorporating active mixing of blood throughout a HFM bundle to

diminish blood boundary layer formation around individual fibers, a significant external barrier to oxygen mass transfer.

This thesis is focused on the development of a novel approach to membrane oxygenation that relies on high pressure oxygen flowing through non-porous oxygen permeable hollow fiber membranes (HFMs), generating a large gradient driving diffusion, rather than relying on a large diffusing surface area[39]. The proof-of-concept work previously completed reported higher oxygen flux ($350 - 550 \text{ mL O}_2 \text{ min}^{-1} \text{ m}^{-2}$) than the Hattler catheters in initial pilot studies using this approach. The work described in this chapter expands on the earlier feasibility studies of Chapter 2 and explores the addition of an active mixing method to both enhance total oxygen flux and also reduce bubble formation in the system. This investigation was done in water; however, it was maintained at body temperature ($37 \text{ }^\circ\text{C}$) and actual blood viscosity (3.5 cP). This was done so that the fibers would operate at a temperature similar to actual use, and so that mixing characteristics were similar to that of blood, which is slightly more viscous than water.

In the previous work (Chapter 2), the higher flux rates were achieved under the conditions of the highest flow and mixing rates (2 LPM or 1200 RPM). Also, the fewest instances of bubbles were observed under these same mixing regimes, notably fewer in the CSTR style chamber. This series of experiments was conducted because we hypothesized that combining a high-pressure oxygen gradient across non-porous HFM

undergoing angular oscillation, thereby overcoming both internal and external barriers to oxygen mass transfer, will achieve the high oxygen transfer efficiencies required for clinically significant intravascular oxygen delivery while also reducing bubble formation. Specifically, we believe that the angular oscillation will provide mixing similar to that of a well-mixed CSTR as previously tested, but also rapid changes in direction will minimize boundary layer formation, helping prevent bubbles from forming.

3.2 Materials and methods

3.2.1 Angular oscillation

Active mixing was employed using angular oscillation, rotating a fiber bundle secured to a central shaft, that was rotated at various speeds over 180 degrees of total rotation. A stepper motor and controller (Tic T249) (www.pololu.com, Las Vegas, Nevada) were used to set the motors rotational speed (deg s^{-1}), total arc traveled, and oscillation settings. The bundles of fiber were created to fit within a 1.5 cm diameter using a mesh spacer at two locations. An example of a completed bundle is shown in **Figure 17**. Travel of an individual fiber is illustrated for macro steps over angle (**Figure 18A**) and macro steps followed by micro-oscillations (**Figure 18B**).

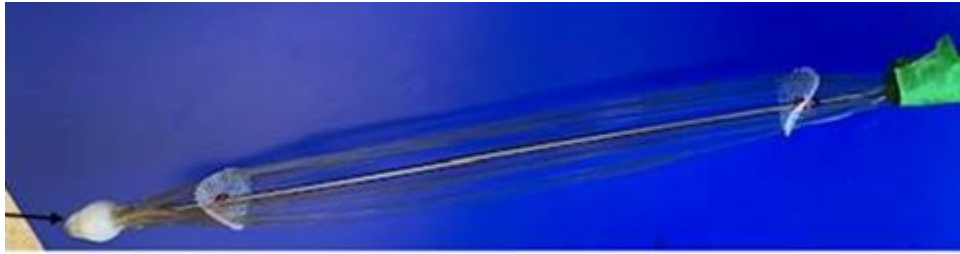


Figure 17: Fiber bundle consisting of Fiber A (88.9 μm wall thickness, 406 μm diameter) used in experiments. Exposed fibers total 16.2 cm with 30 individual fibers end to end. An additional 8 cm of fiber is covered in the potted ends.

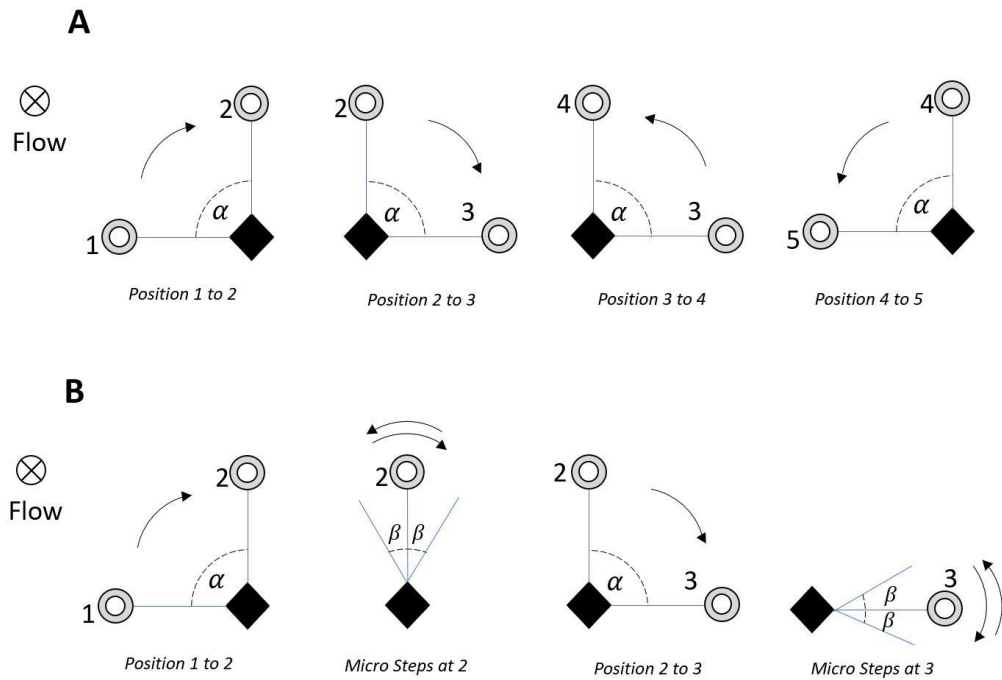


Figure 18: Illustration of individual fiber motion undergoing macro steps (A) and macro + micro step (B) oscillations.

Combinations of macro and micro angles of rotation as well as angular speed to create mixing 8 mixing regimes. An example of one regime is shown in **Figure 19**.

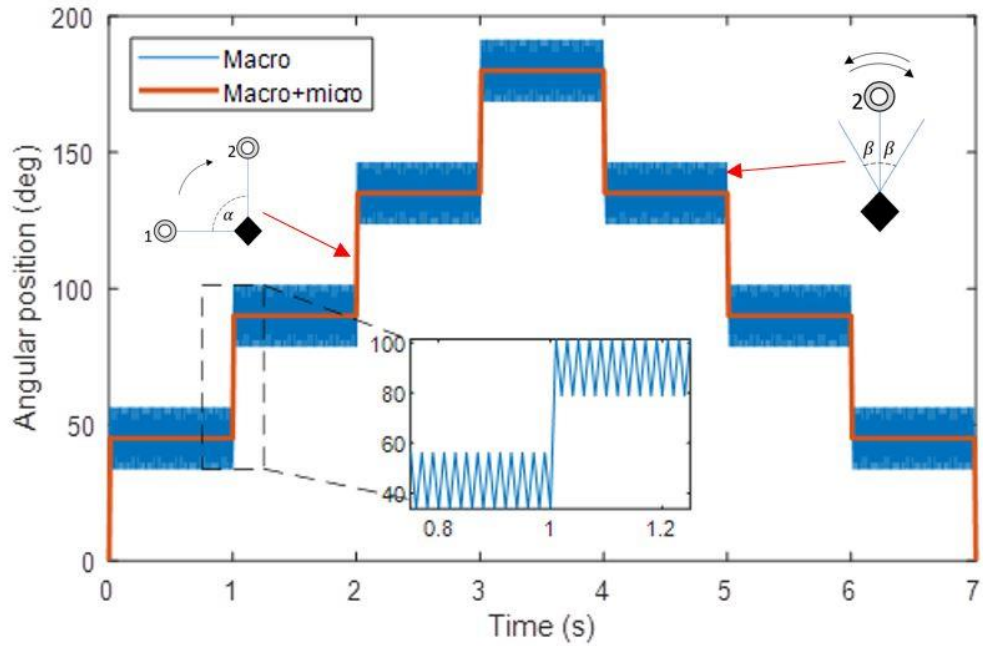


Figure 19: Example of angular position over time for an example mixing regime that uses 45 degree macro steps separated every 1 second with 22.5 degree micro oscillations at a speed of 3200 deg s^{-1}

The mixing settings of each regime tested are listed below in **Table 3**.

Table 3: Mixing regimes investigated in this study (Chapter 3).

Mix	Angular Speed	Macro Angle	Micro Angle
#	<i>deg s⁻¹</i>	<i>deg</i>	<i>deg</i>
1	3200	180	0
2	1600	180	0
3	720	180	0
4	360	180	0
5	3200	22.5	11.25
6	1600	22.5	11.25
7	720	22.5	11.25
8	360	22.5	11.25
9	3200	45	22.5
10	1600	45	22.5
11	720	45	22.5
12	360	45	22.5

3.2.2 Water based bench system

All water-based testing was carried out in a single pass bench top circuit with continuous deoxygenation in line of the circuit (**Figure 20**). The system uses pressurized pure oxygen supplied at the inlet of the fiber(s) using a mass flow controller (Alicat Scientific, Tucson, AZ) with a manual backpressure regulator at the fiber outlet to control the fiber system pressure (Airtrol RV-5300-90, New Berlin, WI). The fiber(s) effluent is also connected to a variable area gas flow meter to record outlet oxygen flow (Dwyer Instruments, Michigan City, IN). The circuit is composed of Tygon tubing with a Rotaflow centrifugal console pump (Maquet Cardiopulmonary, Rastatt, Germany).

Dissolved oxygen is recorded with optical DO probes before and after the reactor chamber that houses the fiber bundles and that are connected to a data logger (Vernier, Beaverton, OR) to record the influent and effluent DO. An ECMO oxygenator (Maquet Quadrox-I, Rastatt, Germany) is included in the circuit allowing for the system to be stripped of oxygen after the reactor with a nitrogen sweep gas. The ECMO cartridge also serves as a heat exchanger for the system with a thermostated water recirculating bath maintained at a temperature of 37 °C. A bypass allows for close-loop testing when needed. The reactor headspace is open to the atmosphere to prevent system pressure effects, and is flushed with nitrogen gas to prevent oxygen intrusion before the device. The reactor is made of two connected chambers, a larger 5.08 cm diameter by 12.2 cm tube where inlet water enters the system, followed by a 1.9 cm diameter by 30 cm chamber that houses the fiber bundles.

Experiments were conducted under 3 regimes, water, water & polyethylene glycol (PEG), and blood mimic (see below). In all cases prior to data collection the system was sparged of oxygen and heated to 37 °C. PEG was added to the system (60 g L⁻¹) to achieve a viscosity of 3.5 cP at 37 °C. Pure oxygen was then allowed to flow through fiber bundles at pressures ranging from 0.14 to 1.38 bar while the inlet and outlet oxygen concentrations were logged. The angular oscillation was turned on prior to data collection and turned off after data collection had ended. Once data collection started, the flow-through system reached a steady state outlet concentration, and data

were logged for at least 5 minutes. If a system parameter was changed, transient data were discarded while reaching a new steady state, followed by sampling for at least 5 minutes of data logging.

Bubble analysis was done by visual inspection of the fibers in the system using a simple bubble count. The number of bubbles appearing on the fibers were counted as they appeared, or at least every 5 minutes if no noticeable change was seen.

Four different diameter fibers all made of Teflon AF2400 were investigated due to off the shelf availability, previous FDA approval for medical use, and high oxygen permeability ($9.9 \times 10^{-8} \text{ cm}^2 \text{ s}^{-1} \text{ cmHg}^{-1}$)[54]. Each fiber is summarized in **Table 4**.

(Biogeneral, Inc., San Diego, CA)

Table 4: Summary of hollow fibers used in angular oscillation testing. Fiber A was previously used in proof-of-concept work (Chapter 2)

Fiber	Internal Diameter	Outer Diameter	Membrane Thickness
-	μm	μm	μm
A	228.6	406.4	88.9
B	609.6	736.6	63.5
C	228.6	304.8	38.1
D	203.2	254	25.4

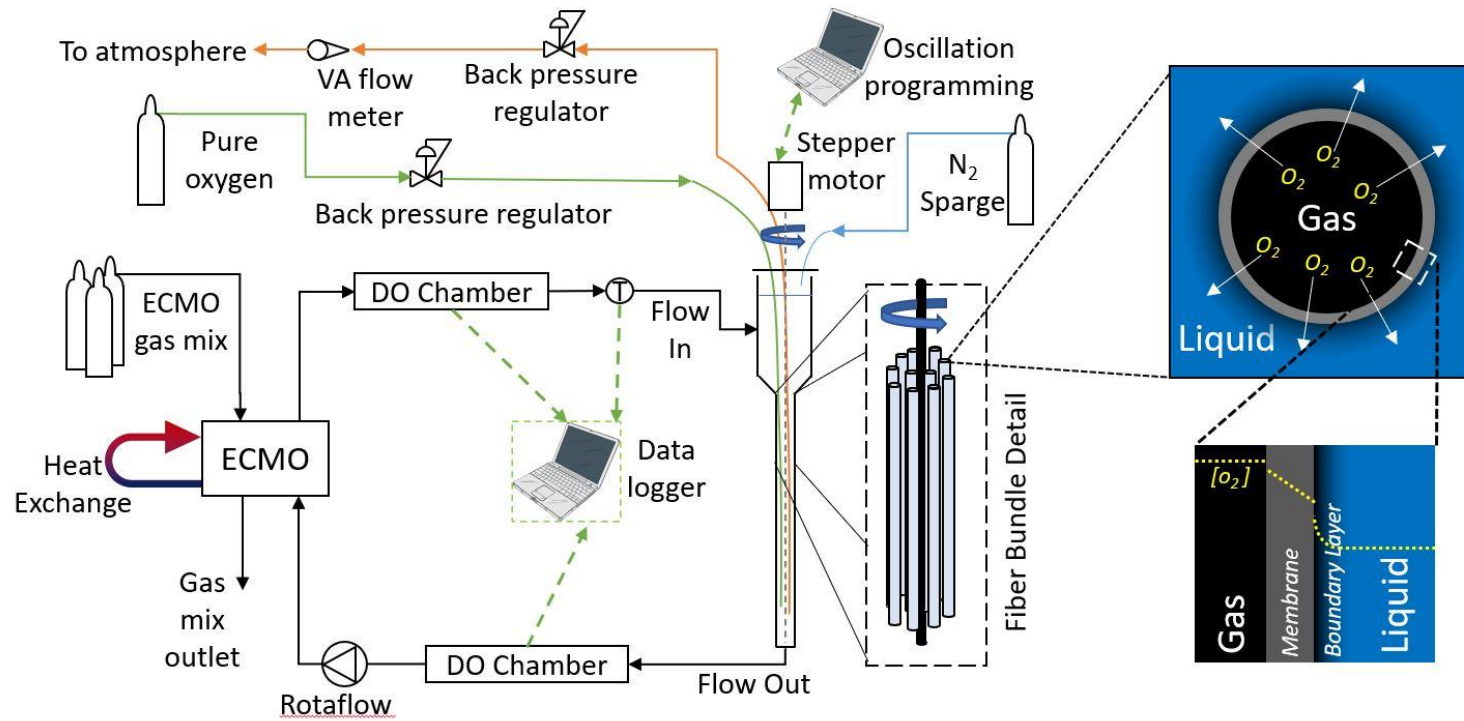


Figure 20: Process schematic of bench top system using water and blood mimic. The ECMO membrane is used to maintain temperature at 37 °C and to remove oxygen before the reactor inlet.

3.2.3 Blood mimic

A blood mimic was created by adding sodium sulfite and cobalt salt catalyst to the system to mimic uptake of oxygen via red blood cells [58]. To achieve this mimic, sodium sulfite and cobalt(II) (in the form of CoSO_4) were added to reach 1.4×10^{-2} M and 5×10^{-4} M respectively. The system was run in the same way as other experiments; however, data was collected using iodometric titration rather than by the DO probes because the transferred oxygen readily reacts with sulfite in the presence of the cobalt catalyst, thus keeping a near zero DO. For the titration, a sample (2 mL) of the system liquid was taken and added to a 5 mL solution of iodine (8×10^{-3} M) which was in excess. This was back-titrated with thiosulfate (0.01 M) to a clear end point using starch indicator. Samples were collected every 5 minutes, allowing for 3 samples for a given set of system parameters.

3.2.4 System modeling

The model which was developed in Chapter 2 was an accurate dynamic model describing oxygen mass transfer in our experimental systems however it did not include active mixing or single pass operation [39]. The model assumes that Fick's first law applies for oxygen flux across the membrane wall via diffusion, while convective mass transport occurs from the outer surface of the membrane into the bulk liquid. Partial differential equations were written describing the transport of oxygen and were then solved numerically. This model was modified to allow for variable inlet concentrations

in the case of incomplete deoxygenation via the ECMO cartridge, as well as a looped fiber bundle configuration.

As in Chapter 2, the liquid in the mixed system was assumed to be ideally mixed, whereas spatial discretization for the liquid was applied along the axial direction for the system to account for the axial gradient of DO and its effect on the transfer flux. The model was discretized in the direction of flow only; no gradient was assumed in the liquid along the radial direction (except for the boundary layer). The hollow fiber was discretized along the axial direction with the partial pressure inside the fiber (P_{fiber}) assumed to drop in a linear fashion from the inlet, as set by the MFC, to the outlet, as set by a back-pressure regulator. The partial pressure of oxygen (P_{wall}) at the membrane-liquid interface was calculated using the Henry's constant for oxygen and solving a mass balance at the interface (**Appendix B**). The impacts of any back diffusion (e.g., of CO_2 or water vapor leading to condensation) into the HFMs was estimated to be negligible because previous authors have shown that the effects of back diffusion on closed end fibers used for bubbleless aeration were negated with relatively short venting periods (20 s every 30 min)[53]. Detailed model equations can be found in **Appendix B**.

The partial differential equations were solved numerically using a Runge-Kutta 4th order algorithm with model parameters (**Table 5**) used in previous work from the literature and system specific parameters. The latter were determined experimentally. In particular, the model was fit to the DO time series (see Results section) using the mass

transfer coefficient of the liquid boundary layer (k_{boundary}) as the fitting parameter. A mass transfer coefficient was fit for each mixing regime simultaneous for a single bundle, and then validated against other bundles. The mass transfer coefficients used in this work were different than previously used (Chapter 2) due to the new mixing method. It should be noted that the lowest coefficient in this work (0.015 cm s^{-1}) was similar to the highest in the previous system (0.0145 cm s^{-1})

Table 5: Model parameters used in this study to characterize 4 fibers across various mixing regimes.

Parameter	Value	Unit	Source
Fiber length	Single: 17	cm	Measured
	Bundle: 14 - 17	cm	Measured
Fiber inner diameter	228.6 - 609.6	μm	Manufacturer
Fiber wall thickness	25.4 - 88.9	μm	Manufacturer
Fiber O ₂ permeability	9.9×10^{-8}	$\text{cm}^2 \text{ s}^{-1} \text{ cmHg}^{-1}$	Manufacturer
Convective mass transfer coefficient	0.015 - 0.030	cm s^{-1}	Fitted to experiment
Number of discrete (axial) fiber elements	10	-	Assumed
Circuit liquid flow rate	0.5 - 2.0	L min^{-1}	Measured
Oxygen pressure range	0.24 - 1.9	bar	Measured, independent parameter

3.3 Results and discussion

3.3.1 Effect of angular oscillation on oxygen bubble formation

Initial work was carried out to investigate differences between the four fibers selected for this study (A -D). This was accomplished by experimentally testing a single fiber loop (2 strands exposed fiber 17 cm each, or 34 cm total length) at the fastest speed (mix 1, 3200 deg/s) with a system flow rate of 0.5 L min⁻¹. This low flow was chosen to increase the DO signal in the single pass system given the use of a single fiber, as well as to reduce bubbles being washed away during this initial testing. **Figure 21** summarizes the oxygen flux vs average system pressure for these single fiber tests.

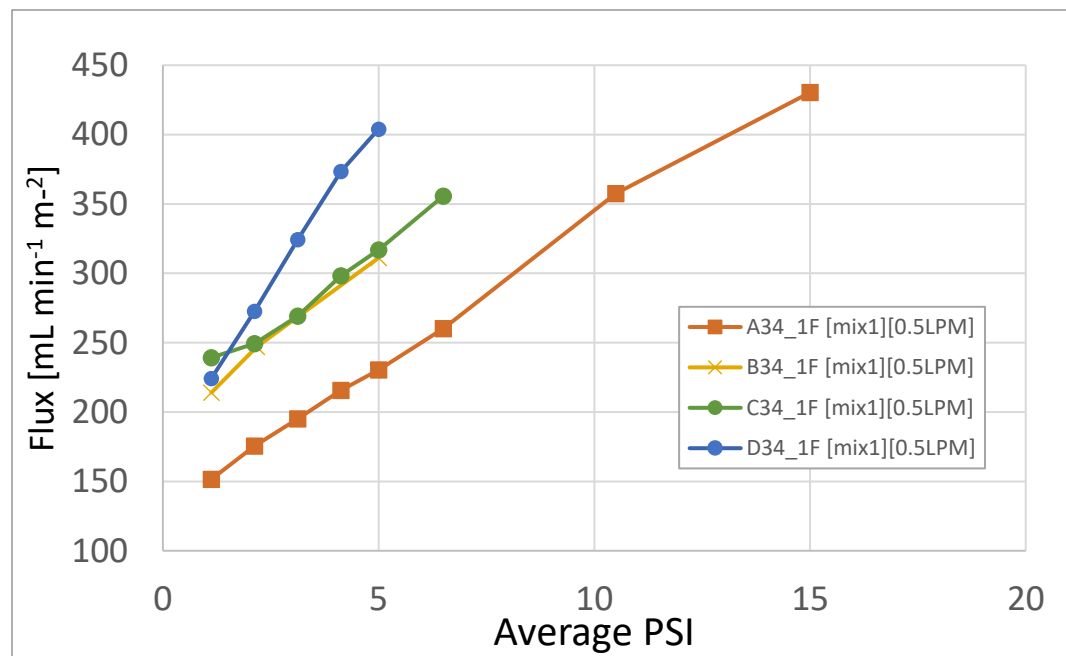


Figure 21: Oxygen flux vs average fiber pressure for single fiber loops (34 cm) of fibers A, B, C, and D using mix 1 (3200 deg/s 180 degrees) at 0.5 LPM system flow.

These data led to the elimination of fibers B and D from this testing for several reasons. Fiber D had an extremely small inner diameter, as well as the smallest outer diameter, leading to extremely low flow rates through the fiber (less than 6 mL min^{-1} at 4 PSI in), as well as early bubble formation (discussed later in this section). These issues are likely part of the reason the trend in flux vs pressure does not follow other fibers for D. Finally, the fiber properties made it extremely prone to kinks, making it difficult for us to currently produce a bundle without severe defects. Fiber B had the largest internal diameter, with a wall thickness between A and C, giving the potential for less pressure drop across the fiber during operation. This fiber had the highest flows of any due to this internal diameter, however it was eliminated due to the difficulty in bending it, leading to kinks, and flattened fiber sections when handled. Further, this fiber produced the most bubbles of any fiber in this testing while only delivering a similar flux as fiber C.

The bubble counts for the flux data in **Figure 21** are shown in **Figure 22**. These bubbles were counted by visual inspection where the number of bubbles (N) stuck to the fiber during mixing was tracked as various pressure settings were applied. To do this each system condition was allowed to get to a steady state as verified on the outlet dissolved oxygen sensor. Pressure was added to the fiber step-wise starting from low inlet pressure with low outlet backpressure, and slowly increased to achieve higher average fiber pressures. Outlet DO concentrations were used to confirm steady state

outlet conditions before any pressure increases. The system was then monitored visually for between 75 and 170 minutes. The short runs were ended once it became apparent bubbles were in excess of 15, while longer runs were continued to achieve higher counts. After a fiber reached 15 or more bubbles on the fiber at a given time, an accurate count was not possible, and therefore no counts higher than 15 are recorded. The initial bubble counting showed that fibers B and D quickly reached 15 or more bubbles during the fastest 180 degree mixing regime (mix 1), and neither was able to stay below 15 at average pressures of 5 PSI. Fibers A and C had similar characteristics for bubble formation, and both were able to avoid rapid bubble formation at average pressures of at least 5 PSI. Fiber A was able to go above 10 PSI before bubbles became uncountable. Fiber C was stopped at an inlet pressure of 10 after other fibers bundles failed at similar pressures due to construction. For these experimental and practical reasons, fibers A and C were chosen to use in bundles for further testing.

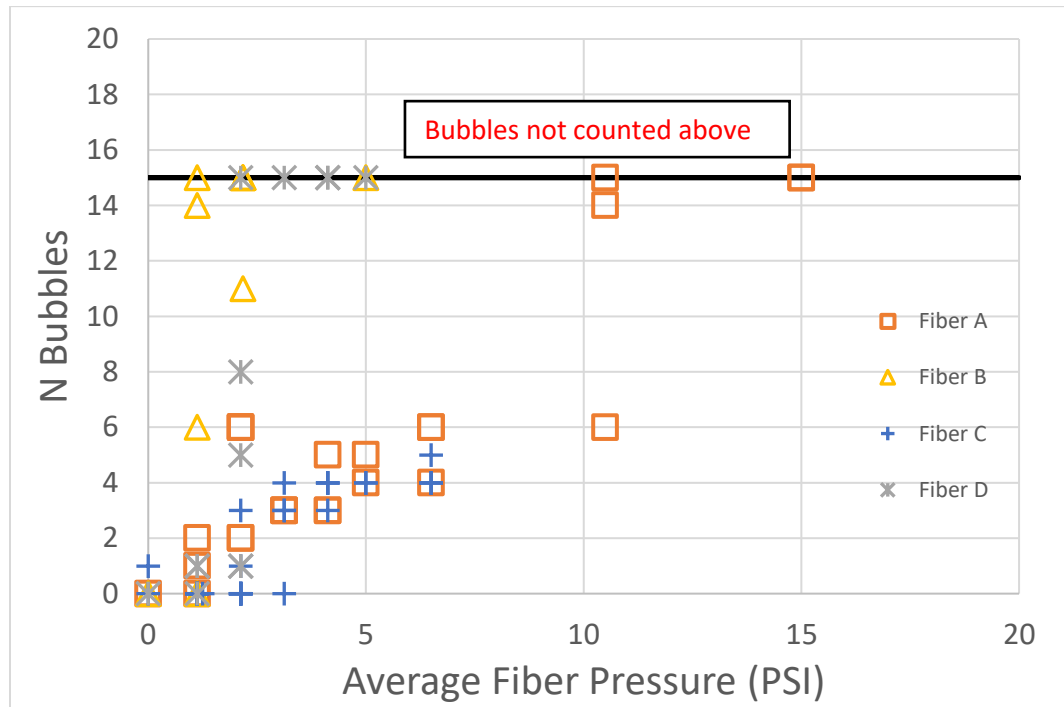


Figure 22: Number of bubbles counted on fibers versus average fiber pressure. All data collected on single fiber looped (34 cm total length) with a system flow rate of 0.5 LPM. Data was collected via visual inspection over the length of the run (75 to 100 minutes total)

Finally, using a single fiber of C, which produced slightly more bubbles than A, 4 mixing regimes were tested for bubble formation. Macro only mixes (1 and 3) were compared to macro and micro mixes (5 and 7), counting bubbles in the same was as previous. As before, the system was deoxygenated, and the fiber bundle was put in the system, mixing was turned on and no oxygen was added for 10 minutes. The inlet and outlet conditions on the fiber bundle were increased and the bubbles were monitored for 10 minutes following steady-state outlet DO concentrations. Bubble formation data is shown in **Figure 23**.

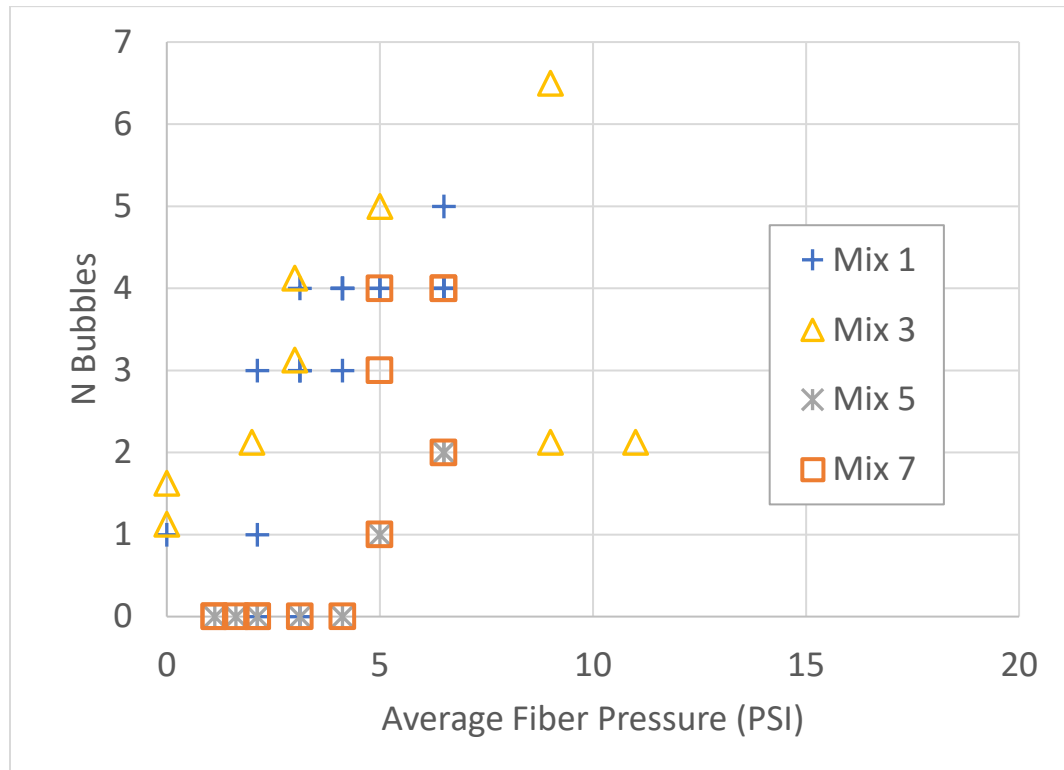


Figure 23: Number of bubbles formed vs average fiber pressure for a single loop of fiber C (34 cm total length) at 0.5 LPM system flow rate under 4 mixing regimes.

While these data are qualitative in nature, they indicate that the macro and micro-oscillation combination can reduce the instances of bubbles on a fiber surface under certain conditions. The fastest speed of this combination (mix 5) was able to limit bubbles to 2 or less on the single fiber over the entire run while maintaining at least 5 PSI average fiber pressure. Mix 7 is $\frac{1}{4}$ the speed of Mix 1 (720 vs 3200 deg/s), and had a slight increase in the number of bubbles. Macro only motion, at any speed, was unable to maintain a zero-bubble state during testing. Data for fiber bundles (A and C) was

unable to be counted in a reasonable way with increased number of fibers (from 1 fiber to 30 fibers).

3.3.2 Effect of angular oscillation on oxygen flux

While the micro-oscillation appears to lead to a reduction in bubbles forming along the fibers, the addition of oscillation appears to also reduce the total flux of a fiber [bundle] as shown in **Figure 24**. Macro only oscillation (Mix 1-3) had higher flux at every mixing and flow regime as compared to the macro + micro (Mix 5-7) fiber C.

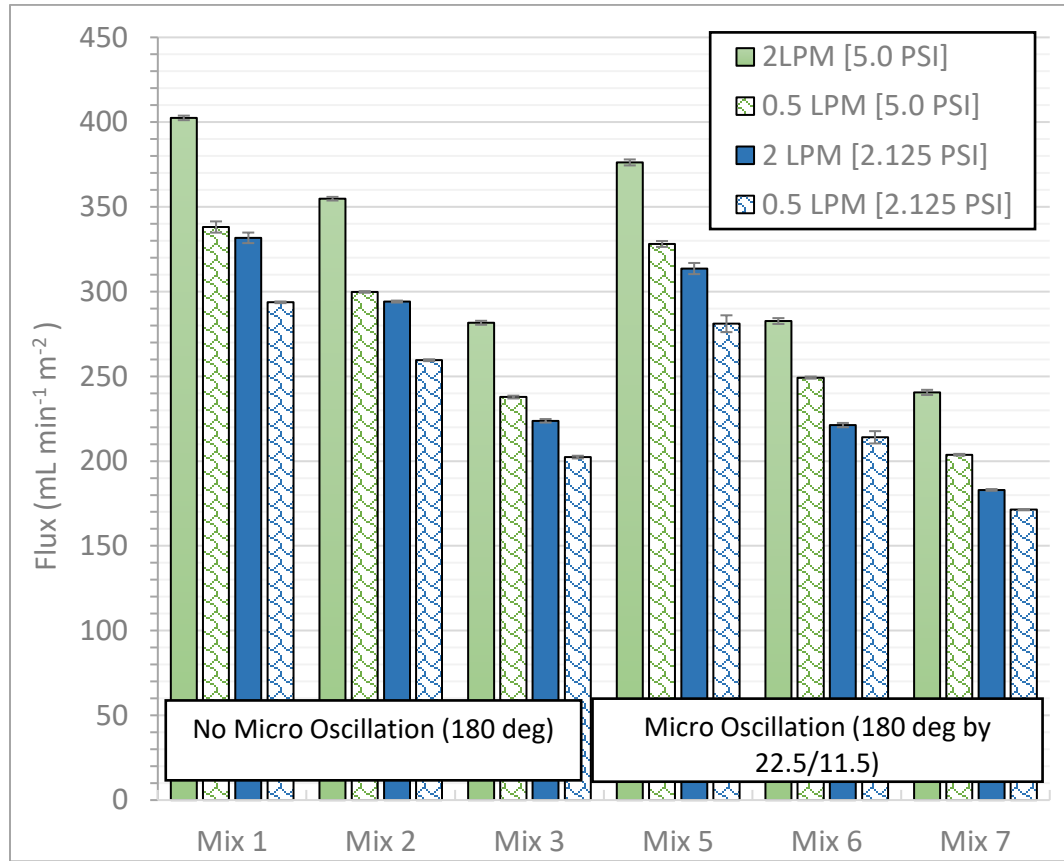


Figure 24: Flux of fiber bundle C (32 total fibers, 14.6 cm each) at various mix regimes at high (5 PSI) and low (2.125 PSI) pressures under two flow conditions (0.5 and 2.0 LPM).

In both macro only and macro + micro scenarios, the higher flow also improves flux regardless of the mixing state, indicating that the system is sensitive to flow conditions around the bundle, even at very high bundle oscillation speeds (up to 3200 deg s⁻¹). In particular this will be important as mixing has been shown to directly impact bubble formation, and it follows that lower flow rates could lead to bubble formation that otherwise would not form (i.e. at higher flow rates). This trend is maintained with fiber bundle A under the same conditions, as seen in **Figure 25**

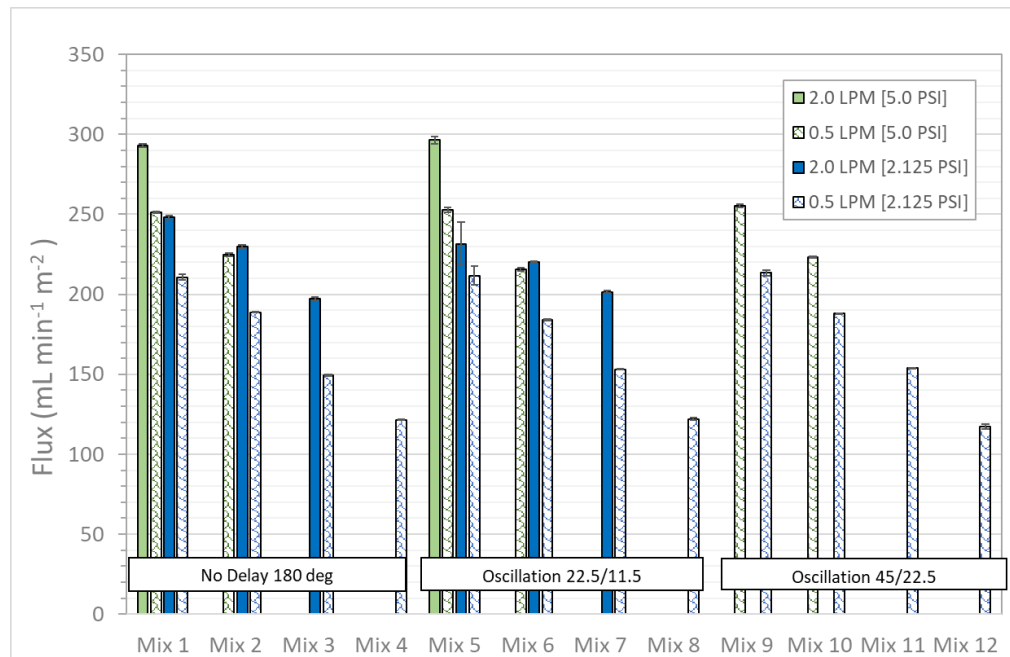


Figure 25: Flux of fiber bundle A (30 total fibers, 16.2 cm each) at various mix regimes at high (5 PSI) and low (2.125 PSI) pressures under two flow conditions (0.5 and 2.0 LPM). Additional mix regimes shown were tested on fiber A and not C.

Looking for trends based on the angular speed of oscillation, **Figure 26** and **27** show that as the speed increases, some diminishing returns on increased flux are

beginning to be observed. The trends also suggest that the combination of macro + micro-oscillations is keeping the trend more linear, and potentially avoiding diminishing returns on flux until a higher angular mixing speed. As a consequence of this, the difference between macro and macro + micro-oscillation at given flow and pressure conditions appears to get smaller for fiber C at the higher angular speeds.

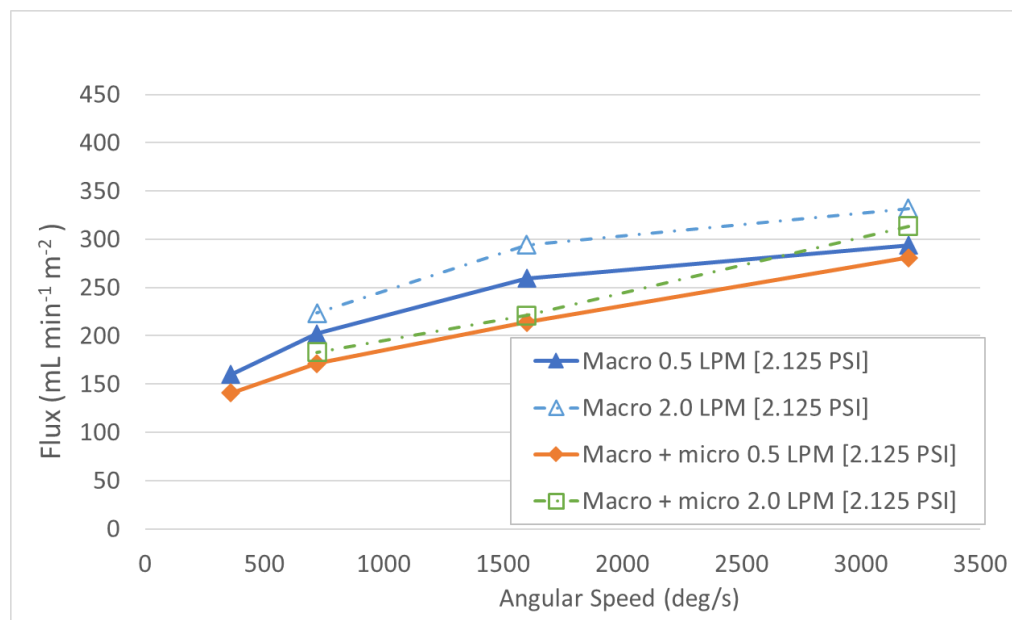


Figure 26: Flux vs angular speed for fiber C bundle at 0.5 (solid) and 2.0 (dashed) LPM with macro and macro + micro oscillation regimes at 2.125 PSI average fiber pressure

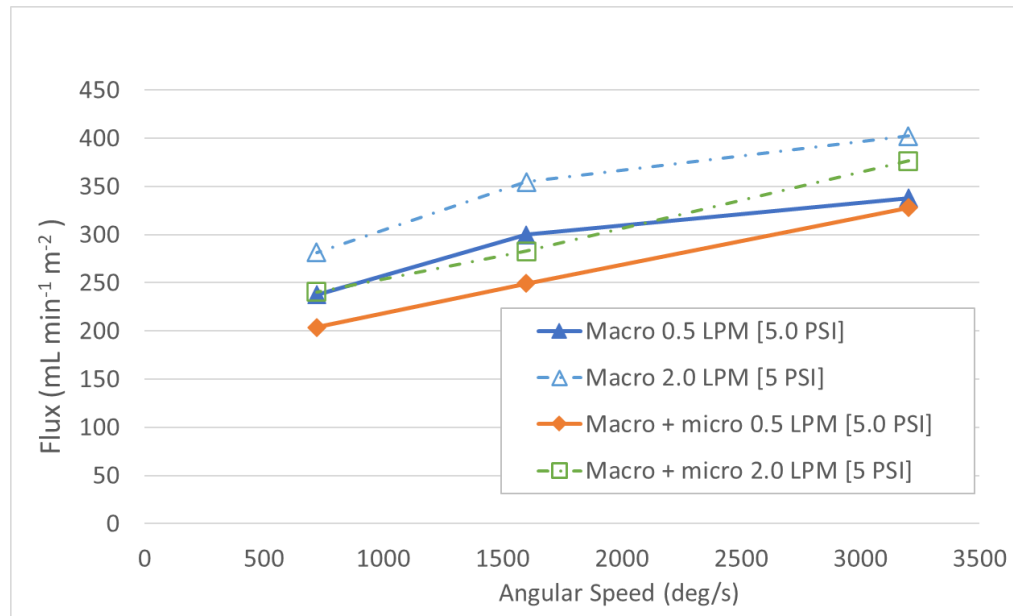


Figure 27: Flux vs angular speed for fiber C bundle at 0.5 (solid) and 2.0 (dashed) LPM with macro and macro + micro oscillation regimes at 5.0 PSI average fiber pressure

In the case of fiber bundle A, at the low flow (0.5 LPM) there was only a difference in flux when the average fiber pressure was increased, seen in **Figure 87**. This is an indication that there is not always a reduction in total flux due to the addition of micro-oscillations, if external transfer is limiting.

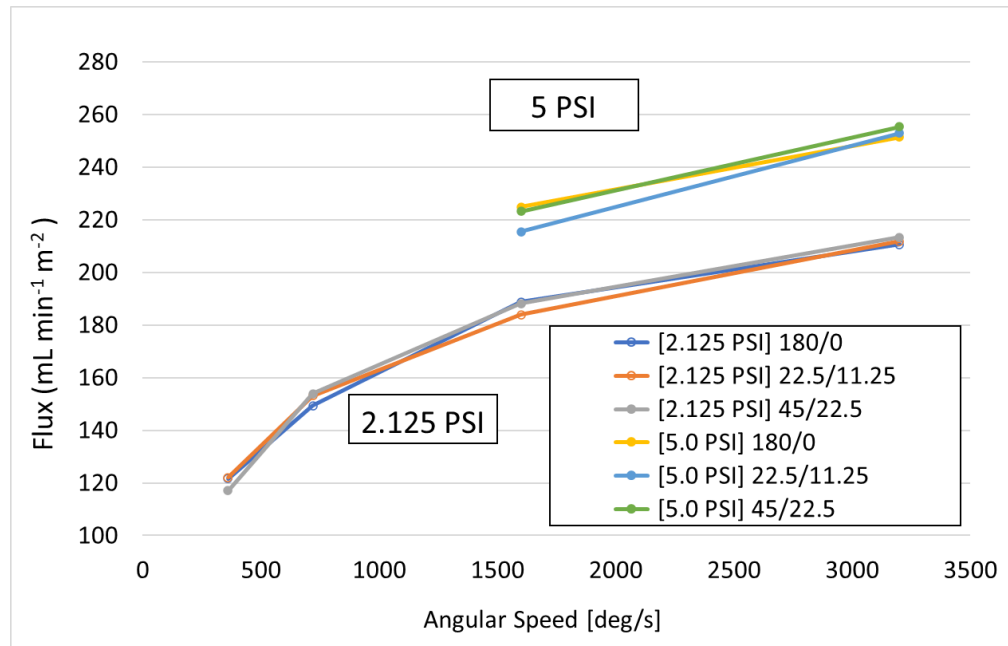


Figure 28: Flux vs angular speed for fiber A bundle at 0.5 LPM with macro and macro + micro oscillation regimes at 2.125 and 5.0 PSI average fiber pressure. 180/0 indicates 180 degree macro oscillation only. 22.5/11.25 indicates 22.5 macro + 11.25 micro oscillation. 45/22.5 indicates 45 macro + 22.5 micro oscillation.

3.3.3 Ability to mimic blood

A sodium sulfite and cobalt(II) catalyst solution was used to attempt a more complete blood mimic by adding an oxygen sink to the system. The use of these chemicals has been shown to previously be a good analog to porcine blood [58]. Our attempts to use this method failed, as a deposit or some sort of film formed on the fiber during operation as soon as oxygen was supplied to fibers (**Figure 29**).



Figure 29: Close-up image of fiber A bundle after being tested in blood mimic solution consisting of sodium sulfite (0.014 M), cobalt(II) (0.0005 M), in 37 °C water at 3.5 cP.

During the data collection process, 2 mL samples were added to a solution with iodine in excess, and back titrated with thiosulfate solution (0.01 M). The titrations with sample from the bench top apparatus did not perform as isolated tests without PEG as a thickener, and appeared to be much cloudier than the testing that did not have PEG.

Continued sampling of the system did not yield significant change in the amount of thiosulfate required to back titrate the solution, indicating a lack of sulfite consumption via oxygen uptake. After over 80 minutes of system run time, no significant signal in sulfite consumption was detected. The system was left running for over 150 minutes while monitoring the outlet DO, with near 0 mg/L readings being recorded. It was expected based on previous oxygen transfer rates that the sulfite would be entirely consumed after 100 - 120 minutes (**Figure 30**).

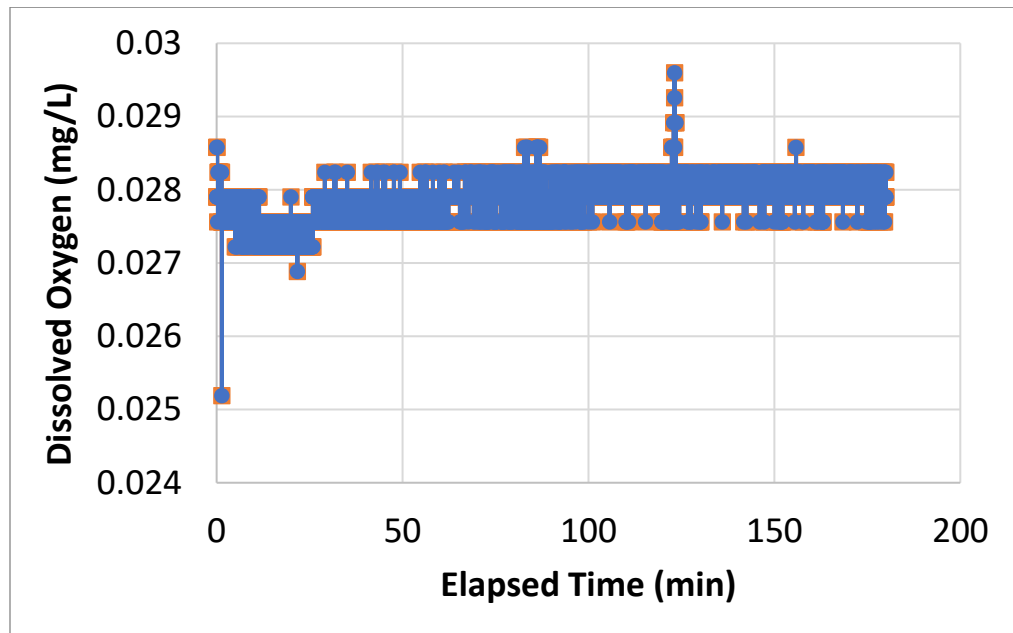


Figure 30: Time series outlet DO data collected for fiber bundle A during sodium sulfite blood mimic testing demonstrating no increase in DO as the system is operating.

In an attempt to see if any oxygen consumption was occurring due to oxygen flux through the fiber, the system was left running for another 100 minutes, with no

increase in DO. Finally, the system was left running overnight while logging DO. After an additional 200 minutes, DO increased as reported in **Figure 31**.

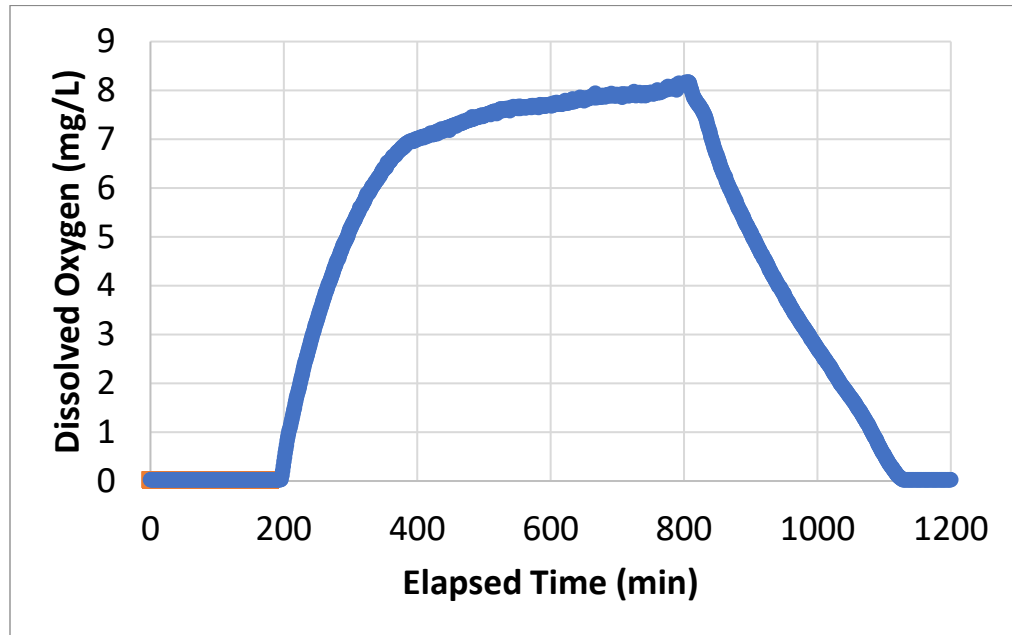


Figure 31: Time series outlet DO data for fiber bundle A collected during sodium sulfite blood mimic testing demonstrating no increase in DO until 200 minutes into the run (previous 300 minutes recorded separately not shown for a total of nearly 500 minutes before DO levels rose)

The increased time to consume the sulfite in excess, as well as the visible coating on the fiber, is believed to have resulted from a notable reduction in oxygen flux due to the fiber coating. A rough estimate would put the flux of the bundle at near $100 \text{ mL min}^{-1} \text{ m}^{-2}$ for the sulfite to be consumed over this period of time, a value lower than any flux tested for this particular bundle in this work, indicating that a significant increase in the resistance to oxygen transfer occurred.

Following this event, the system was purged of all PEG, sodium sulfite, and cobalt(II), and the uncleaned fiber A bundle was tested to see if any notable reduction in oxygen flux remained. These data were collected at 37 °C, however no additional PEG was added back to achieve 3.5 cP viscosity. Surprisingly the flux data was nearly identical to previous bundle runs ($300 \text{ mL min}^{-1} \text{ m}^{-2}$) at an average pressure of 0.345 bar and 2 LPM system flow rates. The time series for this data is shown in **Figure 32**.

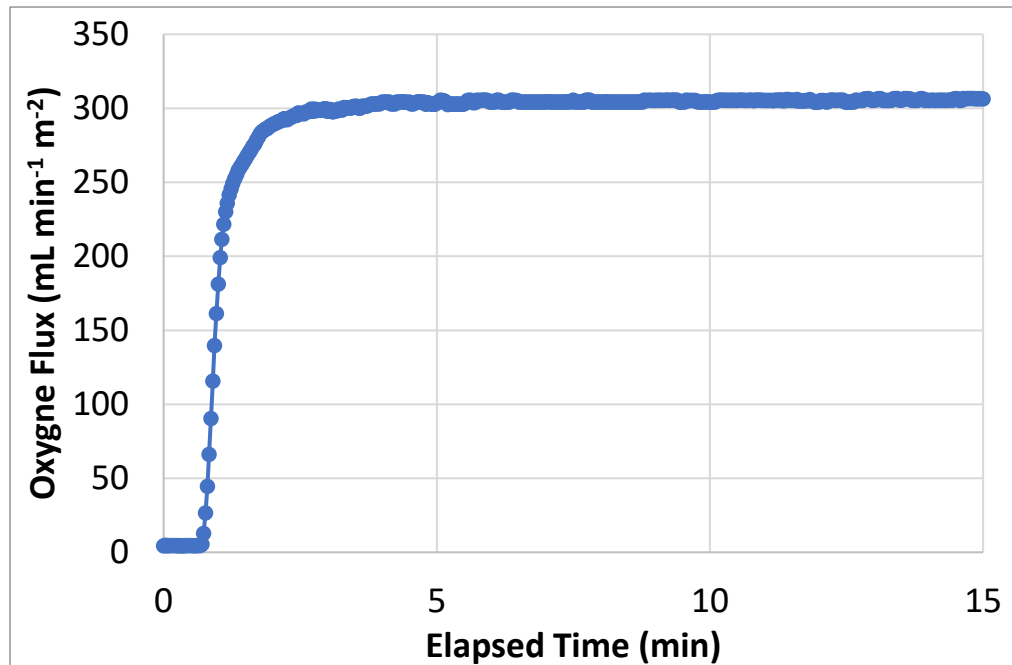


Figure 32: Time series outlet DO data collected for fiber bundle A after a visible coating deposited on surface during sodium sulfite testing using 0.345 bar oxygen at 2 LPM system flow rates. The bundle was able to achieve nearly the same flux as prior to sulfite test ‘coating’.

While the attempt to have a blood mimic failed in this work, the process provided great insight into further reducing bubble formation in a fiber bundle. During the sulfite run, the pressure in the fiber was increased several times in an attempt to get

a signal and confirm oxygen flux was occurring. The pressure was increased to 0.72 bar (10.5 PSI) on average, a pressure in which every fiber tested, to-date, produced bubbles in excess. However, during the sulfite run no visible bubbles were observed. This could potentially be a result of the extremely low flux, or the deposited coating reacting with oxygen. Nevertheless, the result demonstrates that conditions do exist for fibers to operate at much higher pressures than currently possible with no bubble formation. In addition to this, the oxygen transfer flux returned to its nominal value after the system was placed in sulfite free water, where no oxygen sink was present. It should be noted that during the post sulfite water testing at 0.345 bar (5 PSI) no bubbles were observed, which was not the case under previous testing conditions.

3.3.4 Model insights

A modified version of the mathematical model of Chapter 2 was used to further explore the system operating parameters. By running the system in a single pass mode, the model was able to be fitted to steady state data for various mixing and fiber pressures. After initial testing, regimes 4 and 8 were removed from experimental testing due to the extremely low mixing leading to bubble formation. Additionally, because each mixing regime will have fundamentally different mass transfer rates, the model was allowed to fit a mass transfer coefficient for each mixing regime (1 to 3 and 5 to 7). Finally, the data from fiber C was used to train the model in a single pass, with each

mass transfer coefficient fit independent of pressure. The time series dissolved oxygen data and model fit is seen in **Figure 33** below.

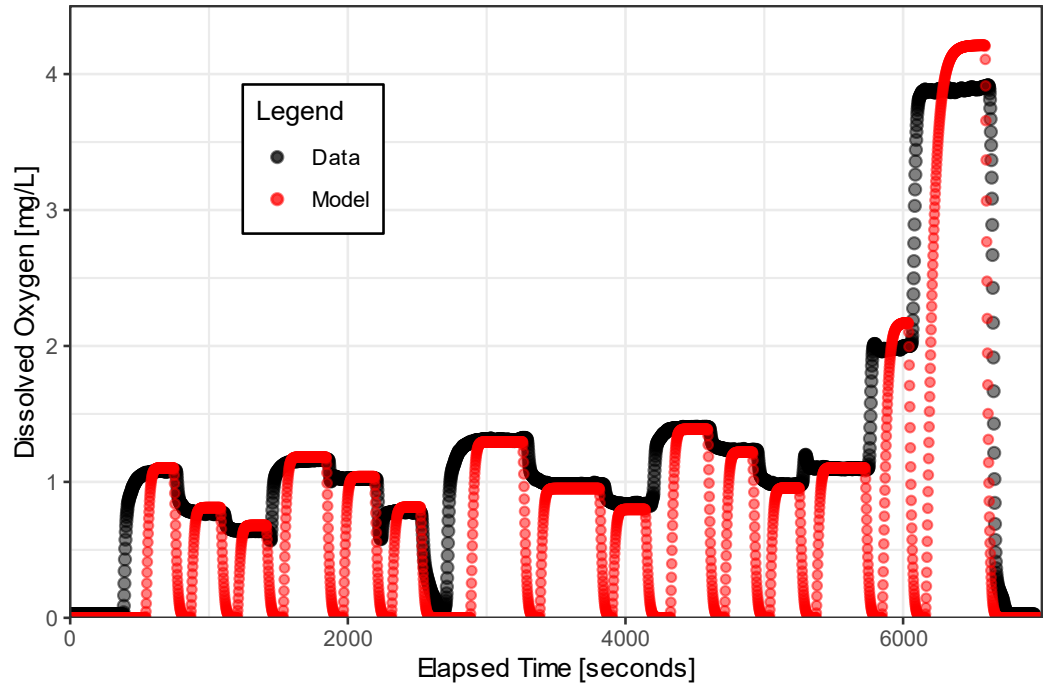


Figure 33: Time series dissolved oxygen (black) and model fit (red) data for fiber bundle C at 2 LPM flow rate. Data is fit only during steady-state portion of data. Data points after ~5500 seconds represent the fit of the model to low flow rates without modifications to mass transfer coefficients.

Each peak in the time series represents a mixing regime at low (0.147 bar) or high (0.345) average fiber pressure. These data points at the end of the series illustrates the model's inability to capture changes in flow rate independent of the mass transfer rate as the flow is decreased. The first high peak (~6000 seconds) attempts to capture a 1 LPM flow, while the last peak is at 0.5 LPM. The discrepancy between the model fit and data indicates that there is a significant reduction in the mass transfer rate due to the flow that is independent of the angular oscillation mixing. The model therefore must be fit to a

given mix scenario under a given flow condition (e.g. Mix 1 at 2 LPM, mix 1 at 0.5 LPM). For this analysis, the model was fit to 2 LPM data, and only data collected under 2 LPM flow rates is compared to model outputs. A summary of each fitted mass transfer coefficient is provided in **Table 6**.

Table 6: Summary of fitted mass transfer coefficient values for each mix regime modeled. Macro angle is the total arc travelled before changing direction, while micro angle is the angle of oscillation after a macro movement if enabled (for 1 second)

Mix #	Mass Transfer Coefficient, k <i>cm s⁻¹</i>	Angular Speed <i>deg s⁻¹</i>	Macro Angle <i>deg</i>	Micro Angle <i>deg</i>
1	0.030	3200	180	0
2	0.025	1600	180	0
3	0.019	720	180	0
5	0.027	3200	22.5	11.25
6	0.018	1600	22.5	11.25
7	0.015	720	22.5	11.25

To validate the model, the model was used with the fitted parameters in **Table 6** to predict outlet concentrations for fiber bundle A. The model-simulated data vs. experimental data for both bundle A and C are shown in **Figure 34** and **35**. Generally, the model predicted the data well, especially in the cases without micro-oscillations. In the case of fiber A predictions, mixing regimes 1, 2 and 3 were predicted within 3%. The fit for the high-speed micro-oscillation was relatively good at both pressures, with under a 7% difference to the steady-state outlet concentration. However, the model was off by 13%

and 19% for mix regime 6 and 7 respectively. It is possible that at lower speeds, the micro-oscillations impart fiber motion that is dissimilar enough to not be captured by the model.

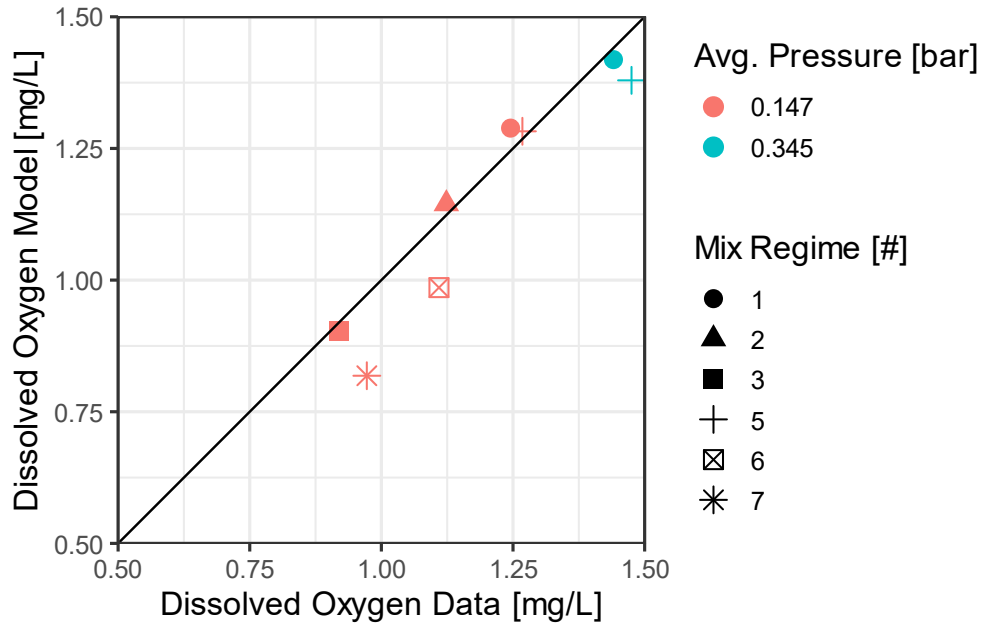


Figure 34: Dissolved oxygen model data vs actual for the reactor outlet with fiber bundle A at 2 LPM. This data was used to validate the model. Mixing with micro oscillations (5, 6 and 7) were notably underpredicted in all but one case.

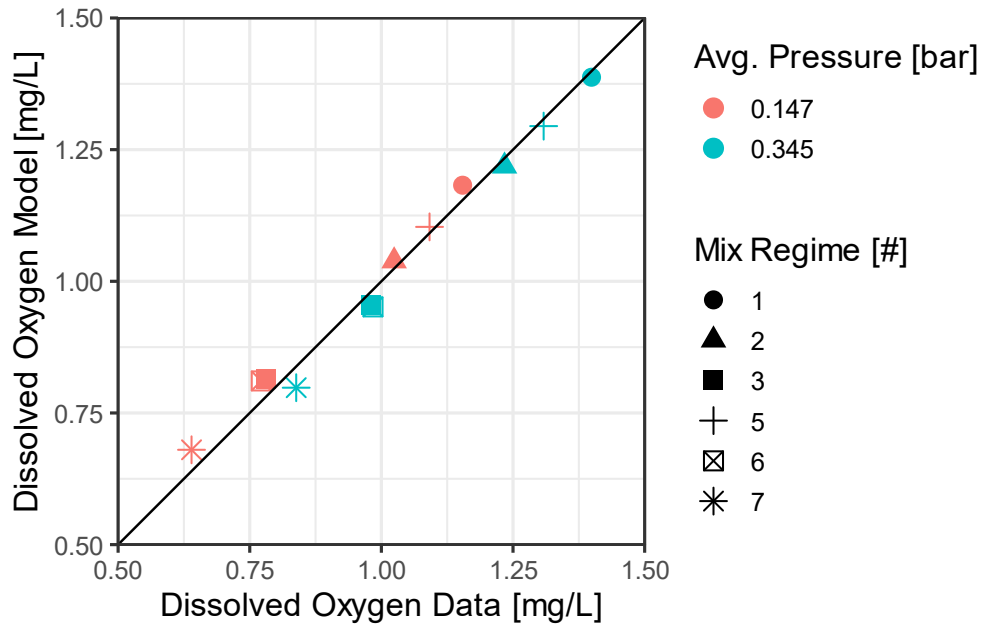


Figure 35: Dissolved oxygen model data vs actual for the reactor outlet with fiber bundle C at 2 LPM. This data was used to train the model.

As evidenced in the flux data (Figure 24 and 25), the micro-oscillation mixing reduced flux compared to the macro-oscillation only. This is manifested in the model via reduced mass transfer coefficients. The percent difference is lowest at the highest mixing speed ($3200 \text{ deg sec}^{-1}$), but not consistent across the three regimes, as shown in Figure 36.

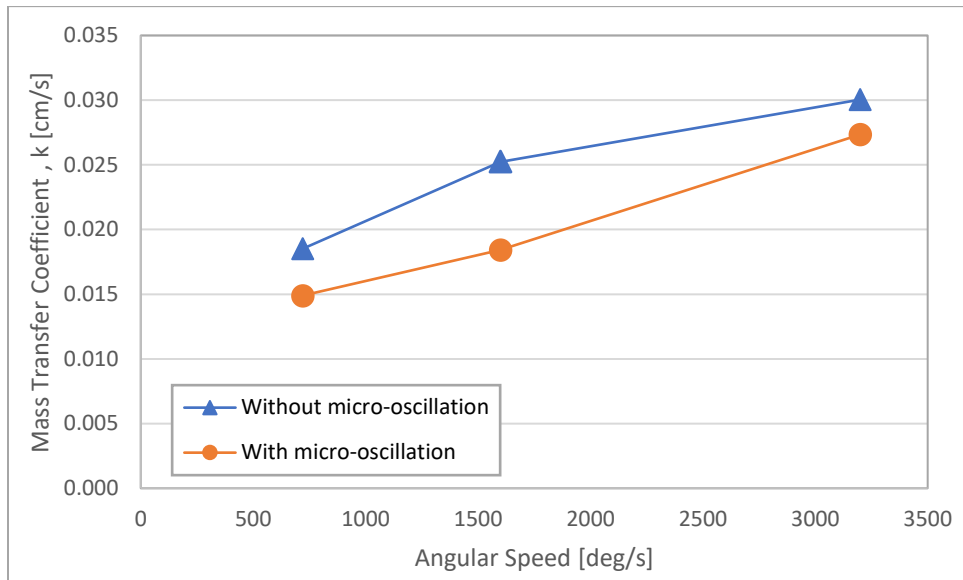


Figure 36: Fitted mass transfer coefficients (k) vs angular speed of mixing for macro and macro + micro oscillation mix methods.

Further investigation should be done on the difference between the macro and macro and micro mixing regimes to fully understand the key differences. This will be important as micro-oscillations have a positive impact on reduced bubbles in the bundles based on visual inspection of fibers during data collection.

Finally, we can use the model to investigate overall mixing performance as it relates to the mass transfer coefficient. **Figure 37** shows the estimated flux for each fiber bundle versus the mass transfer coefficient for the system as it was tested for both fiber bundles at the low pressure (0.147 bar). The model indicates that we are still operating in a mixing regime where further mass flux improvements could be made with additional mixing.

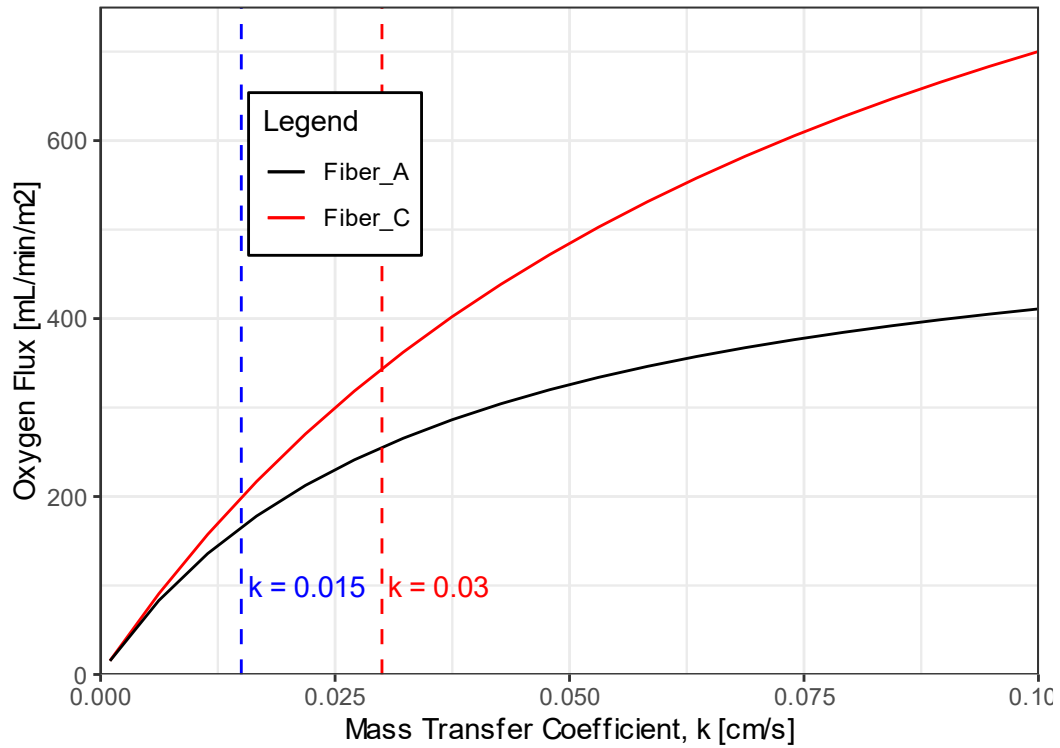


Figure 37: Mass transfer coefficient (k) versus estimated oxygen flux from model data at 0.147 bar. Blue dashed line indicates lowest mass transfer coefficient from model fit (mix7), while the red dashed line indicates the highest mass transfer coefficient that was fitted (mix 1).

Additionally, it indicates that if faster speeds are safe, operation with slightly reduced flux with micro-oscillations on could be an acceptable trade off to prevent bubbles by slight increases in pressure as seen in **Figure 38**.

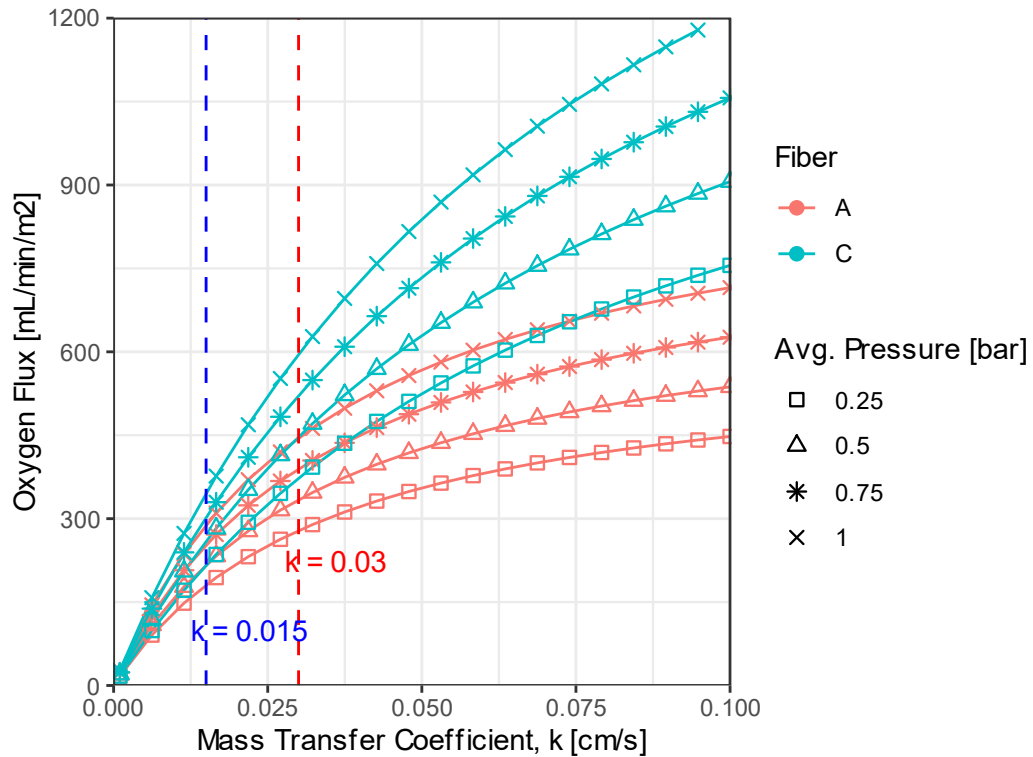


Figure 38: Model-simulated oxygen flux vs. mass transfer coefficient (k) at various pressures for fiber A and C. This simulation illustrates that the system is operating in a region where increasing pressure can improve total flux in a significant way compared to mixing alone. Values generated with constant surface area, flow rate (2 LPM) and average pressure.

3.4 Conclusions

The development of an intravascular oxygenator that can deliver clinically relevant amounts of oxygen directly to the bloodstream to help support neonates, children, and adults with hypoxic respiratory failure is an ambitious goal. Establishing the upper limits of oxygen transfer efficiency without bubble formation will allow us to better predict and scale-up to the required HFM surface area for the construction of alpha prototypes. The work described in this study has expanded on previous water-

based proof-of-concept work using hyperbaric oxygen to deliver oxygen directly to the vascular system. We have shown that the introduction of angular oscillation as a form of active mixing has allowed us to maintain oxygen fluxes of up to $400 \text{ mL min}^{-1} \text{ m}^{-2}$ at lower pressures than our previous work. This increase of almost $150 \text{ mL min}^{-1} \text{ m}^{-2}$ was achieved despite the use of water maintained at body temperature (37 C) and at the viscosity of blood (3.5 cP), both of which reduce oxygen transfer rates when compared to the 20 C water used in our previous work. Adaptation of the previously developed mathematical model indicates continued improvements can be achieved with even more active mixing. Future work in blood will investigate the effects of angular oscillation on oxygen transport and bubble formation in an in vitro system, and to determine if this method of active mixing has any deleterious effects on red blood cells.

Most importantly, we investigated the advent of bubbles in the system undergoing angular oscillation. We found that the active mixing helped to reduce bubbles overall, but micro-oscillations added to the primary macro-oscillations had at least a qualitative reduction in bubbles that appeared on the surface of single fiber configurations when compared to macro-oscillations alone. However, even with a noticeable reduction in bubbles observed on single fiber loops at various oscillation parameters, the higher flux configurations produced bubbles at all mixing regimes. This highlights the need for the future work in blood to incorporate a the ultrasound bubble

detection methods initially tested in the proof-of-concept work (Chapter 2) to better understand how bubbles behave in blood-based systems.

Attempts to use a sulfite solution as a blood mimic to gain insight on how oxygenation would operate in blood were unsuccessful due to precipitation of unknown salts onto the fiber surface during testing, which impacted all data collected in an unpredictable way. However, the testing did provide insight on the potential for bubble formation control via fiber coatings. During the sodium sulfite blood mimic runs, bubbles were not observed in the system under any mixing condition, as well as at pressures twice as high as initially planned (0.72 vs 0.34 bar). Further investigation will be needed to determine if the lack of bubble formation was due to an overall flux reduction, or some other phenomena, as the bundle was tested at normal pressures after the system had consumed all the sulfite, and still no bubbles formed on the surface. At the very least, this finding indicates promise in targeted coatings around regions that will always be prone to bubbles due to the nature of fluid flow around the fiber bundle (such as spacers, fittings, etc.).

4. Computational fluid dynamic modeling: oscillation investigation

4.1 Introduction

The advent of Computational Fluid Dynamics (CFD), has allowed for modeling efforts that go beyond the simple diffusion and convection models presented and discussed in Chapters 2 and 3. Specifically, we can use the power of CFD to seek to understand the limitations of oxygen transport at the scale of individual fibers, for a myriad of existing, or potential oxygenator designs [59]–[63]. In the development of a hyperbaric oxygenation catheter, our group as well as many previous attempts have established that active mixing is a necessity to reach oxygen transfer fluxes of clinical relevance [15], [37], [45]. In the case of previous works, the active mixing was primarily employed to improve overall flux in such a device to help improve its potential efficacy. Our novel approach uses hyperbaric oxygen to overcome mass transfer limitations, reducing the need for active mixing to achieve required oxygen transport rates. However, with greater oxygen transfer fluxes, with the use of hyperbaric oxygen, there could be concerns with bubble formation in the blood. Our previous work has indeed shown that bubble formation occurs under many scenarios in water, both at room temperature and physiological conditions (37 °C 3.5 cP). We therefore investigated the potential of angular oscillations (see Chapter 3) to actively disrupt boundary layers in our system, reducing the overall chance of bubble formation by reducing the formation of ‘steady-state’ conditions in the catheter. The first iteration of this work used two types

of angular oscillation: 1) a macro step that travels up to 180 degrees of rotation back and forth, and 2) a micro step that travelled at half the angle of the macro step used, for a set period of 1 second (e.g., a macro step of 22.5 degrees followed by 1 second of 11.25-degree micro oscillations). This work concluded 3 primary findings: 1) angular oscillations can significantly improve overall oxygen flux without the need for 360-degree rotation, 2) the use of macro and micro-oscillations together reduced observable bubbles on the surface of single fibers, and 3) the superimposed macro and micro-oscillation schemes slightly reduced the overall flux at the expense of fewer bubbles on the fiber surface. To test the micro-oscillations of individual fibers under extremely controlled conditions that maintain fiber-fiber spacing, fiber speed, and fiber deformations, it would be difficult to test at the bench scale. The use of CFD to investigate specific details related to the oscillation motion we propose is therefore an ideal way to gain early insight into future iterations of the methods without the need for extensive benchtop testing. Notably, CFD modeling will save time and expense on the development of the hardware to conduct such tests, allowing for future bench testing to be focused on configurations based on the in-silico prototyping. Previous work using CFD illustrates how it can be used to test designs or configurations computationally without the need for complex bench top testing, as for example, in the case of ECMO-style devices [64].

A complete model approach to such a device would require fluid physics, blood chemistry and complex moving geometry of the fibers. This extremely complex system would require extensive model inputs for both material and blood properties. However, the most difficult task would be the fiber motion within the system. A full-scale 3D in-silica dynamic prototyping modeling effort would therefore need to include significant validation of the model with respect to the fiber motion in such a device. In the case of this work, it is however more useful to focus on the potential relative impacts of fiber motion within a simplified system. The objective of this work is then not the exact simulation of an oxygenation catheter in motion, but instead understanding how fiber movement in a simplified system impacts total oxygen transport.

This work therefore explores a simplified 2D model of a system in which several fiber segments move at predefined speeds and distances. This will allow us to gain insight on the effects certain parameters have on the relative oxygen transport in such a system, helping to focus future bench top work that can be used to validate more complex models in the future.

4.2 Materials and Methods

4.2.1 Model description and assumptions

A conceptual 2D system was created to explore fiber motion within a confined space. A set of 5 fibers was evenly spaced and centered in a 1 cm wide channel that is 2 cm long. The outlet was taken 1 cm away, and the side walls (left and right geometry)

were taken as no slip wall conditions. An example of the geometry is seen in **Figure 39** for a 400 μm fiber-fiber spacing scenario. The oxygen flux was incorporated using a boundary flux condition using the permeability for Teflon AF2400 and the membrane thickness. For the purposes of the model the pressure inside the fiber was assumed to be a constant pressure of ambient air (0.2 bar partial pressure of pure oxygen). Because the model is 2D, changes in fiber diameter would not change the surface area, and were not used in the parametric sweep. Changes to membrane wall thickness were also not used to keep the analysis focused only on the macro and macro + micro-oscillation impacts.

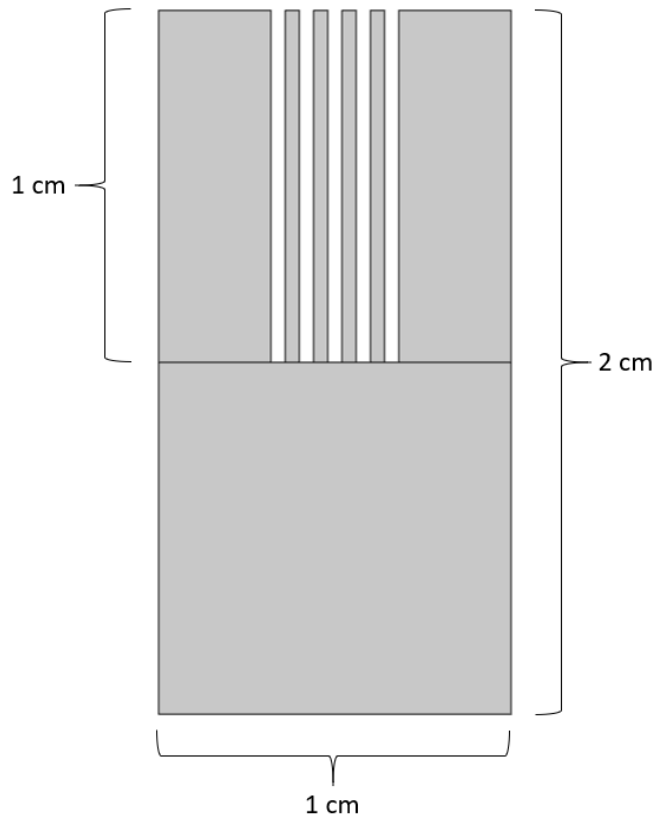


Figure 39: 2D model geometry of five 1 cm fiber segments within a 1 cm diameter tube. Inlet water from the top of the geometry, and an outflow at the bottom of the figure. Inlet flow is assumed laminar, and an average velocity is used across the boundary condition to prevent short circuiting around the fiber geometry due to the absence of additional fibers filling the space.

The model was parameterized to easily change influent flow, fiber-fiber spacing, macro movement distance, and micro movement distance, and the rate at which the micro movements occurred. To simplify the data analysis and reduce run times, the model was run keeping the number of micro-oscillations between macro steps constant instead of holding the pattern for a set time. In other words, a micro step was always 4 if macro steps were included. An example of fiber displacement over time without a

macro step at 5Hz is seen in **Figure 40**. An example of the same settings with an added macro step is seen in **Figure 41**.

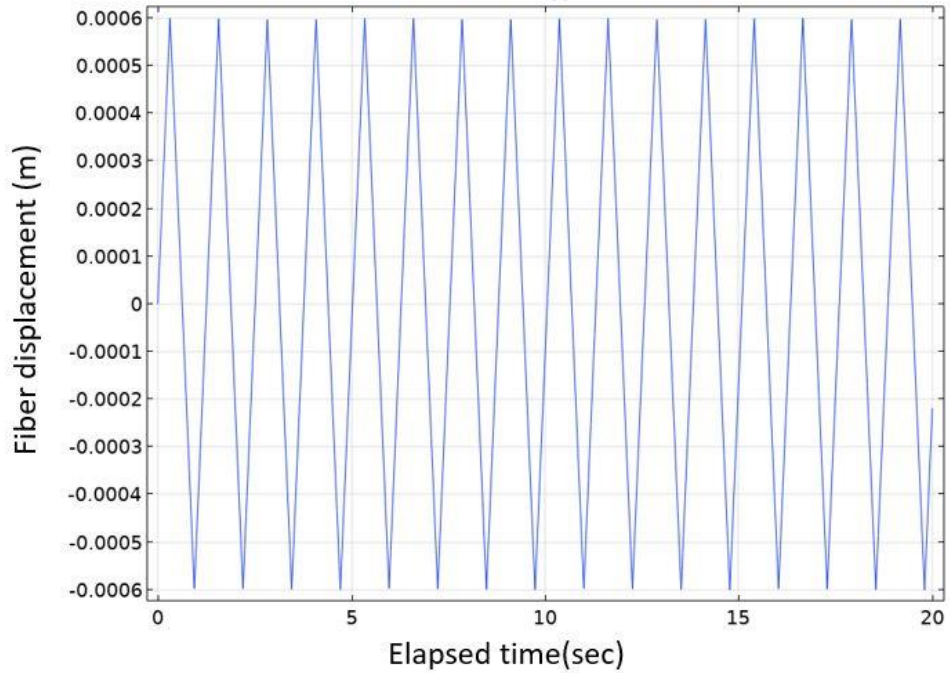


Figure 40: Triangle wave depicting fiber 'bundle' displacement as a function of time for a typical study analysis that does not include a macro step movement. Shown is a 5 Hz frequency of a 600 μm micro oscillation study.

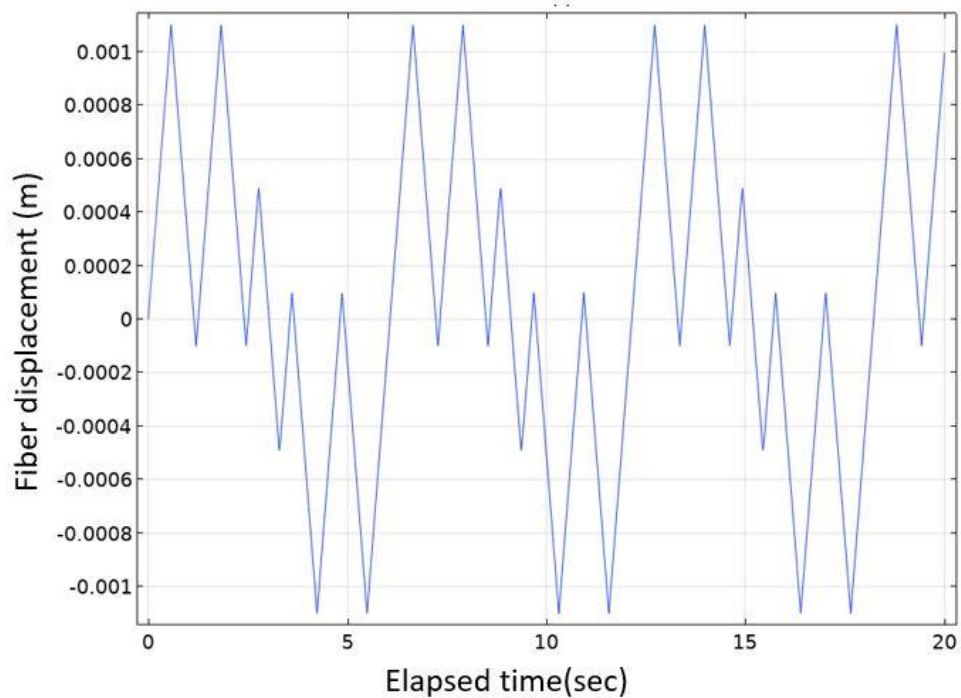


Figure 41: Triangle wave depicting fiber ‘bundle’ displacement as a function of time for a typical study analysis that includes a macro step movement. Shown is a 5 Hz frequency of a 600 μm micro oscillation study with a macro displacement of 500 μm after 4 micro movements.

The use of a set number of oscillations instead of a set time had the added benefit of avoiding differences in total travel distance and instead focuses only on the speed of the movement. The working fluid was taken as room temperature water (20 °C) using built-in COMSOL material properties.

A breakdown of all the parameterized values for the model are shown in **Table 7**. The macro distance was used at 1 in the analysis to prevent mathematical errors related to the triangular wave function generating the fiber movements. A separate

evaluation with no fiber motion (macro and micro distance = 0) was computed to get a base system flux for comparison.

Table 7: Parametric values used in COMSOL model parametric sweeps for micro oscillation analysis.

Parameter	Values	Unit	Description
Fiber Spacing	100,200,400	μm	Fiber-fiber space
micro-Hz	1.25,2.5,5,10	-	Frequency of the micro motion
macro-Hz Factor	4	-	Number of micro-oscillations between macro steps
macro distance	0,1,500	μm	Distance to new oscillation location
micro distance	0,200,400,600		Distance traveled +/- in a micro step
Flow	0.05,0.10	L/min	Flow used to compute average inlet velocity assuming a 1 cm pipe

The fiber movements were incorporated by using the triangular wave function previously discussed, using the amplitude as the total displacement. **Figure 42** illustrates an example of 3 triangular waves at 5 Hz. Because the amplitude is effectively changing the velocity of motion, the results will need to be considered at a given fiber velocity.

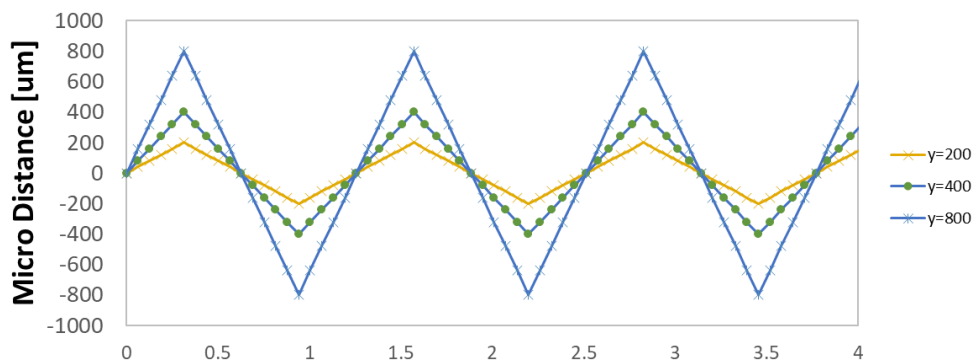


Figure 42: Triangular wave function for a frequency of 5 Hz for 3 different amplitudes. The x-axis represents time elapsed in seconds, and the y-axis represents the left to right movement of the fiber grouping.

To ensure some data points in the analysis at the same velocity, the required frequency to achieve the same fiber velocity was determined for several of the data points by using the ratio of amplitude to frequency, as shown in **Figure 43**.

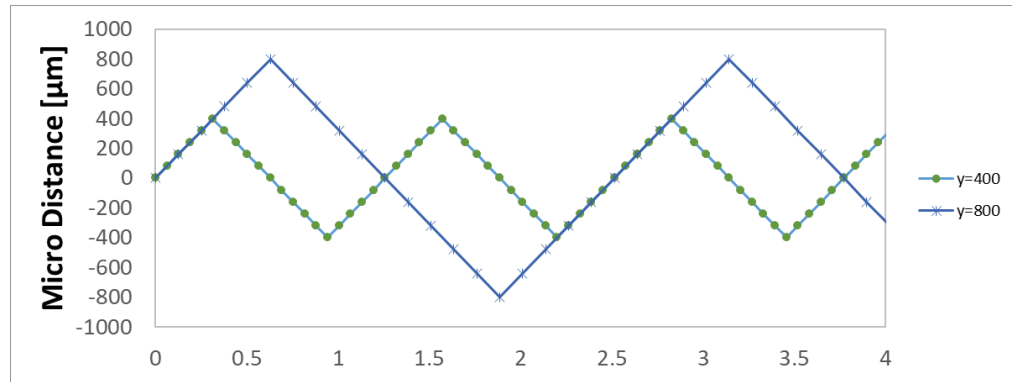


Figure 43: Example of extra frequency included in analysis to ensure that data is generated using the same velocity of motion for different total micro movements. Here showing an example of a 5 Hz 400 μm micro movement overlain with a 2.5 Hz 800 μm movement.

Finally, all of these models were run as time-dependent study due to the non-steady-state nature of the fiber motion, for a total length of time for 20 seconds, which was long enough to get to a steady mass flux rate out of the outlet model boundary.

4.2.2 Model physics

Model fluid physics were determined to be operating under laminar conditions before parametric sweeps were conducted by calculating the Reynolds number (Re) assuming pipe flow in a tube 1cm in diameter. Re can be calculated via 4.1:

$$Re = \frac{\rho v D}{\mu} \quad (4.1)$$

Where ρ is density (kg m^{-3}), V is velocity (m s^{-1}), D is a characteristic length (m), in this case the assumed pipe diameter, and μ is the dynamic viscosity (Pa s). $\text{Re} < 2,000$ are considered laminar flow, while $\text{Re} > 4,000$ is considered turbulent flow. The flow regime was checked by running a turbulent flow model for 10 Hz oscillations under the higher flow value (0.1 LPM), and confirmed that the Re was under 200 for various locations in the model (outlet, mid cross section) based on the maximum velocity at a given spatial location in the model. With the Re confirmed to be $\ll 2,000$, laminar physics were used for all parametric sweeps.

COMSOL solves single-phase laminar fluid flow based on Navier-Stokes for conservation of momentum (4.2) simplified for incompressible flow and is solved in conjunction with the continuity equation for continuity of mass (4.3).

$$\rho \frac{\partial u}{\partial t} + \rho(u \cdot \nabla)u = \Delta \cdot [-pl + K] + F \quad 4.2$$

$$\rho \nabla \cdot u = 0 \quad 4.3$$

Where u is the fluid velocity, ρ is the fluid density, p is the fluid pressure, μ is the fluid dynamic viscosity, l is the identity matrix, K is the viscous stress tensor (Pa), and F is the volume force vector (N m^{-3})

Oxygen flux across from the fiber was set using a boundary condition and the fiber permeability. (4.4)

$$J = K \frac{(P_{\text{fiber}} - H * C_{\text{wall}})}{d_m} \quad (4.4)$$

Where K is the fiber permeability using molar units (s mol kg^{-1}), P_{fiber} is the partial pressure of oxygen in the fiber (Pa), H is the Henry's constant for oxygen, and C_{wall} is the concentration in the liquid at the wall, and d_m is the membrane wall thickness.

Oxygen transport within the system volume was solved using the advection-diffusion equations (4.5)

$$\frac{dC}{dt} = D\nabla^2 C - \vec{u} \cdot \nabla C \quad (4.5)$$

Where J is the mass flux diffusive vector ($\text{mol m}^{-2} \text{s}^{-1}$), D is the diffusion coefficient ($\text{m}^2 \text{s}^{-1}$) and C is the concentration (mol m^{-3}) and u is the velocity (m s^{-1}). Geometry deformation was controlled via the deformed geometry physics interface in COMSOL. A shape function of 1 was used in conjunction with Laplace mesh smoothing to accomplish deformations. Laplace was used because it is the least computationally intensive due to being linear and uncoupled in each coordinate direction, and is ideal for linear deformations such as the one in this model.

The models were tested for conservation of mass by comparison of total mass of fluid into and out of the system where anything less than a 5% difference was acceptable. No slip wall conditions were used for both the fiber and side walls of the model. The fluid parameters in the system were set using default COMSOL values and represent water. The pressure and temperature were set to 1 atm and 20 °C respectfully. The outlet boundary condition was controlled via a pressure of 0 atm, with no backflow allowed with normal flow across the boundary. Model meshing was controlled via

physics-controlled meshing in COMSOL using quadrilateral shapes at boundaries and triangular shapes in the rest of the model. The mesh was acceptable at coarse meshing for laminar flow physics; however, deformation was high and so the mesh size was reduced to normal allowing the mesh skewness to remain around 0.5 or better for simulations.

The final parametric sweep analysis was set up in COMSOL in two steps: 1) A steady state-study with no deformed geometry (i.e. no fiber motion) and 2) a time-dependent study that incorporated the steady-state results as the starting values of the time-dependent study. This was done to both speed up the computing times slightly, provide better starting values to the model, and finally to allow a pseudo-steady-state during fiber movement to be achieved within the short 20 second model time period.

4.2.3 Model evaluations

Model analysis was evaluated based on the total mass of oxygen transported out of the outlet over the 20 second study. To compute the total mass out of the system a total mass flux was recorded at the outlet over 0.05 second intervals. The mass flux was computed in mass per time (mol s^{-1}) for all cases. The outlet mass flow was periodic in nature depending on the oscillation settings, but confirmed to be in pseudo steady state by visual inspection of the time series data. **Figure 44** shows an example of a sub-set of outlet mass flow rates over the 20 second run.

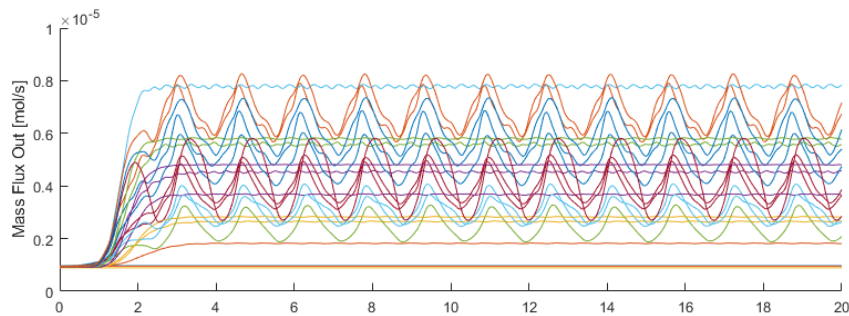


Figure 44: Mass flow out of the model over run time for various model runs (unlabeled) showing psuedo-steady states reached after roughly 2-3 seconds.

MATLAB was used to integrate all mass flow outlet time series into a cumulative mass out over time, an example of a subset of the data after integration (from **Figure 44**) is shown in **Figure 45**.

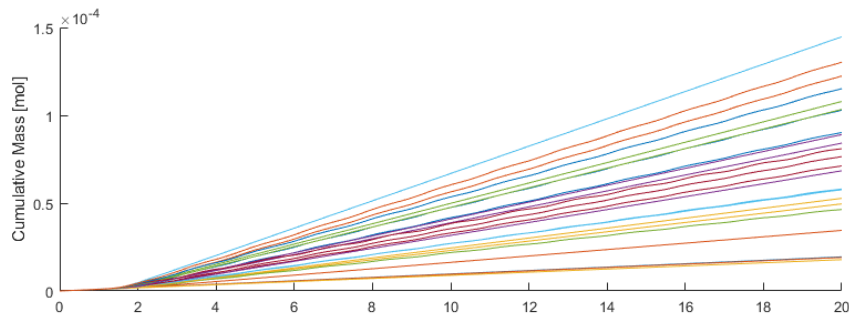


Figure 45: Cumulative mass out over time plotted after integration via MATLAB. Time-series are a subset of all model runs (unlabeled).

Finally, the data was normalized to a base-case scenario by dividing the cumulative mass out after 20 seconds. The base case that was used to normalize all data was a static model (no oscillations) with the lowest flow (0.05 LPM) and the smallest fiber-fiber spacing (100 μm). The final output was then a relative mass factor, indicating

how many times the cumulative mass was increased in the same time period as compared to the base or worst-case scenario. When plotted this data should appear to be roughly asymptote at a steady-state relative mass value over time if the model was indeed run for long enough, as shown in the **Figure 46** (derived from **Figures 44 and 45**).

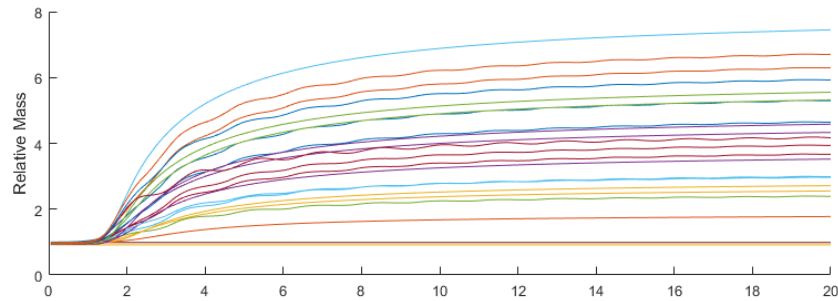


Figure 46: Relative mass value derived after normalizing cumulative mass out over time data to the worst-case model. [unlabeled] data should asymptote at a value to indicate relative stability in outlet mass flow.

In addition to the mass flux data at the outlet boundary, COMSOL probes were placed on the center fiber walls to record the maximum concentration along the wall at a given time-step, illustrated by the red highlights in **Figure 47**.

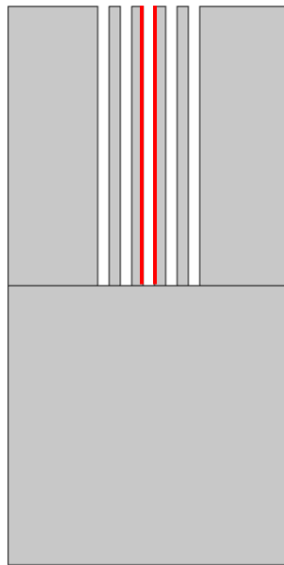


Figure 47: 2D geometry with center fiber walls highlighted in red, indicating boundary at which the maximum wall concentration data is monitored in the model over time for parametric analyses.

4.3 Results and Discussion

4.3.1 Relative mass flow results

The relative total mass out results are shown in **Figure 48** and **49**. While the values for these models cannot be directly compared to bench testing (Chapter 3), we can first note that the trends appear to follow earlier data as seen in Chapter 2 (**Figures 26,27,28**). Notably, as the velocity of travel is increased with all other factors being remaining constant, the system will reach a mass transport plateau (e.g., **Figure 48** at 400 μm spacing, relative mass increases are much lower after 1000 $\mu\text{m s}^{-1}$ velocity). This was most notable in the data from Fiber A, which are the same properties (i.e. membrane wall thickness) as used in this COMSOL model (Chapter 2, **Figure 28**). A second trend that matches experimental trends is the increased flux as a result of higher system liquid

flow rates with all other conditions being equal. The increase from very low velocities ($< 500 \mu\text{m s}^{-1}$) to high velocities ($> 1500 \mu\text{m s}^{-1}$) predict the large relative mass increases for a given fiber spacing in all cases. Similar improvements in relative mass are observed when fiber spacing is increased for a given velocity (from 100 to 400 μm), as well as when the flow is doubled from 0.05 to 0.1 LPM. The results show that these three factors (spacing, fluid flow rate, and movement velocity) are likely to play the largest role in total maximum flux in a system. However, the impact of the oscillation regime can be significant based on this model. For example, a near 2.5 times increase in relative mass output is observed in the 0.1 LPM flow, 400 μm spacing data when going from 200 to 600 μm micro movements (**Figure 49**). This illustrates the point that optimizations of such a mixing scheme will be very sensitive to a systems operating parameters, and is a perfect problem for this type of in-silica prototyping to tackle.

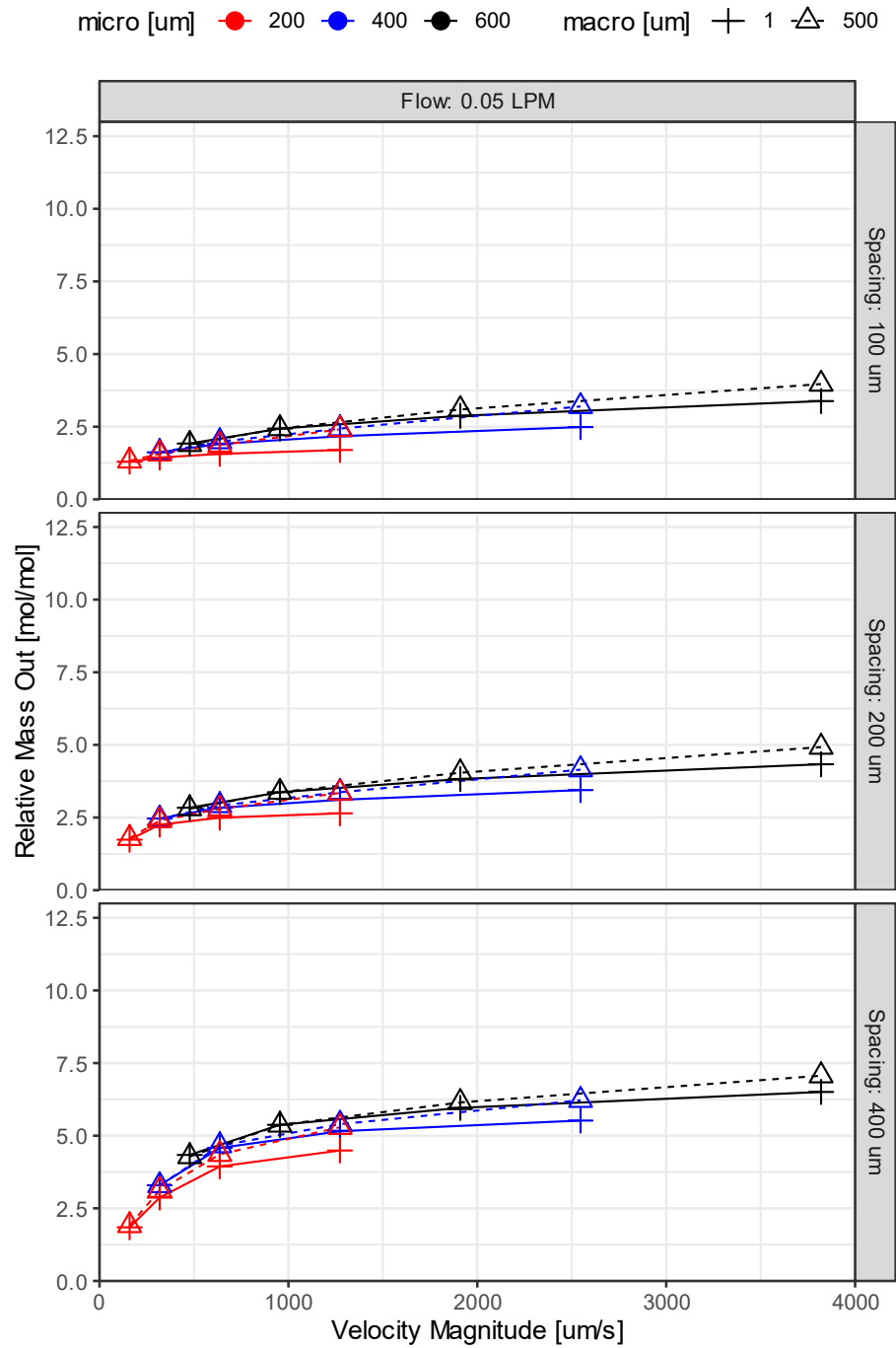


Figure 48: Relative total mass out of 2D model after 20 seconds for 0.05 LPM flow condition for fiber-fiber spacing between 100 and 400 μm versus average travel velocity. Macro steps vary between off (1 μm) and on (500 μm).

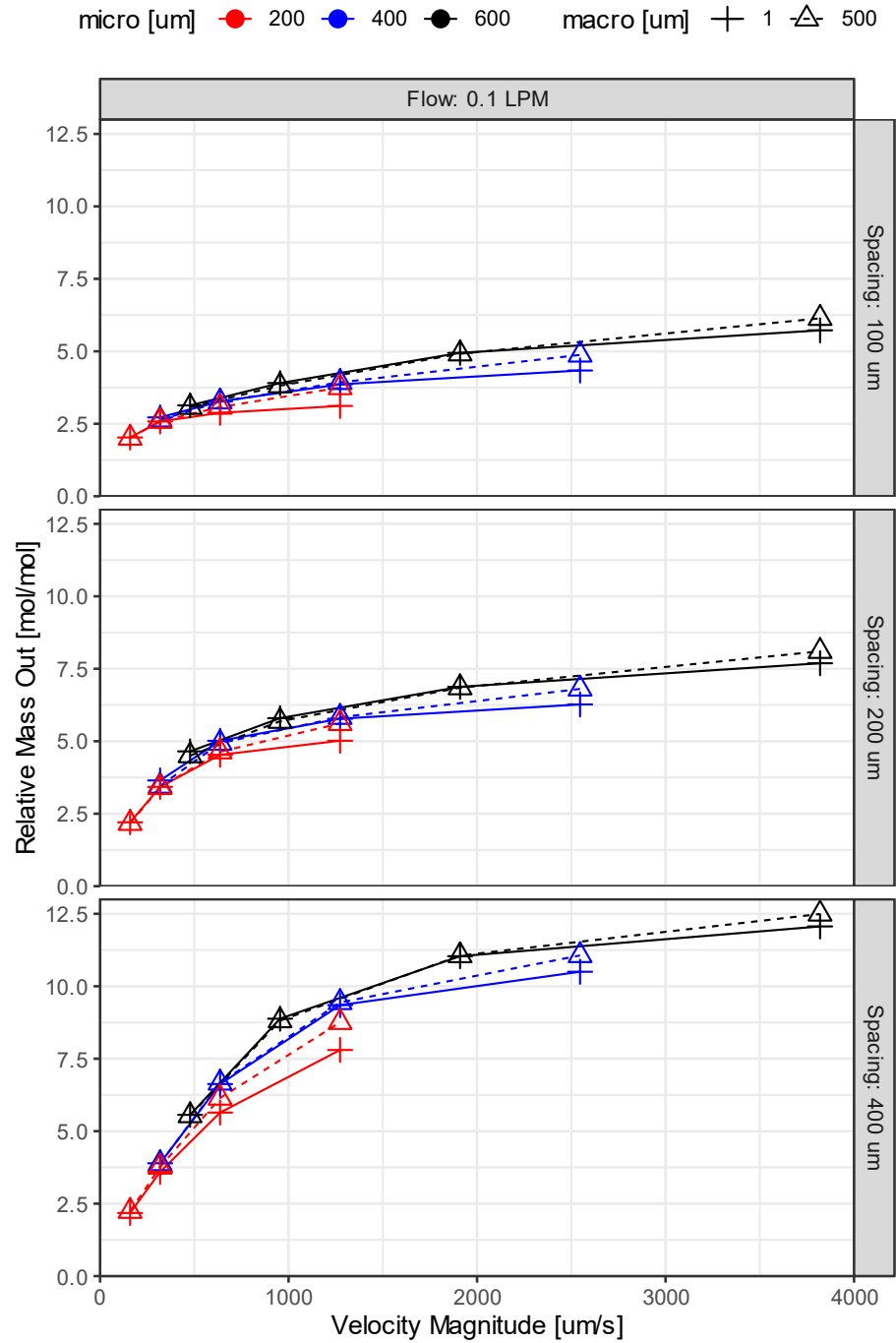


Figure 49: Relative total mass out of 2D model after 20 seconds for 0.1 LPM flow condition for fiber-fiber spacing between 100 and 400 μm versus average travel velocity. Macro steps vary between off (1 μm) and on (500 μm).

Finally, we can see that this modeling data indicates that macro and micro movements combined improve total mass output in the system so long as the only change in the system is going from micro steps only, to micro steps augmented by the macro displacement. However, this data also suggests total travel distance is a key factor in the total mass output, evidenced by the larger micro steps outperforming the smaller micro steps at a given velocity. For example, we see this most readily at the 0.1 LPM flow rate (**Figure 40**), where at around $1200 \mu\text{m s}^{-1}$ velocity, the addition of a macro step of $500 \mu\text{m}$ is not enough to offset the increased output of the micro step increasing from 200 to $400 \mu\text{m}$ without a macro step. This is not true for the 0.05 LPM case, where the macro step addition was able to surpass the $400 \mu\text{m}$ micro-only condition. This result indicates a diminishing return on the macro step if the system flow is large enough to clear away a significant portion of the bulk liquid (i.e. high external transport). In this regard, the model matches well with the trends from bench testing indicating a loss of flux with the addition of micro and macro-oscillations together.

4.3.2 Maximum wall concentration results

A secondary goal of this modeling effort was to see if any insight could be gained as to why less bubble formation was observed on the walls of fibers undergoing micro-oscillations in the bench testing performed in earlier work. To explore this, the maximum wall concentration along the center fiber was tracked during each study. The maximum value was used as opposed to the average to reduce the effects of the inlet

conditions the model was set-up under. It is also likely that the maximum DO concentration is more representative of the risk or likelihood of a bubble forming. Time series data for maximum molar concentration are presented in **Figures 50 to 55** below. The data has been reduced to the center fiber's 'right side' maximal concentration at a given time, and further separated by the fiber-fiber spacing and flow condition the model occurred under.

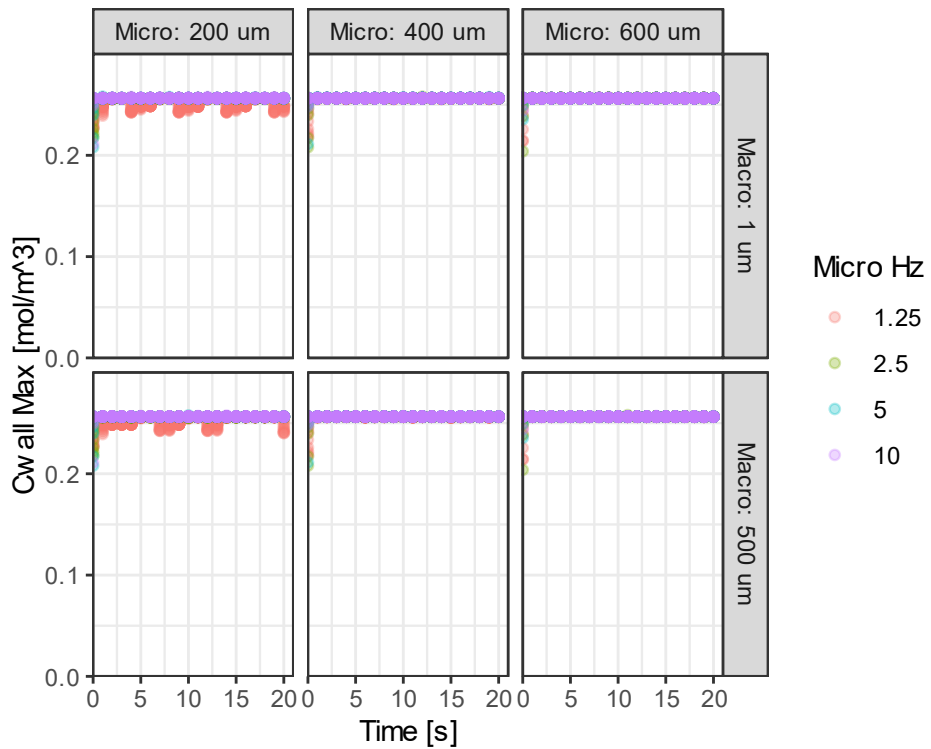


Figure 50: Time series data of maximum [right side] fiber wall DO concentration for 0.05 LPM and 100 μm fiber-fiber spacing. DO saturation at these conditions is a concentration of 0.26 mol m^{-3} .

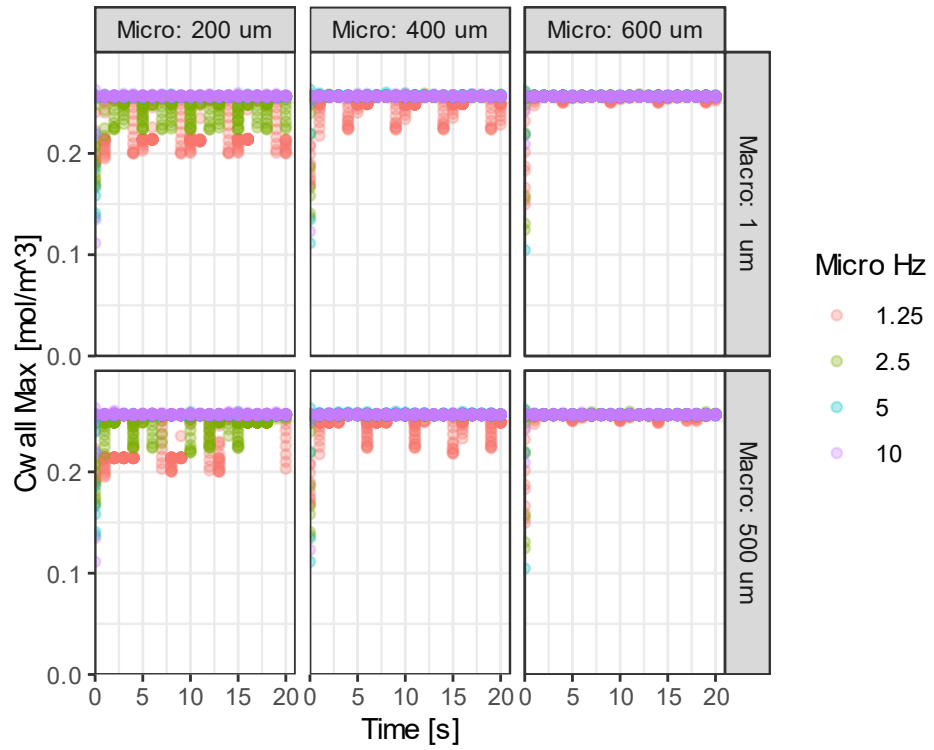


Figure 51: Time series data of maximum [right side] fiber wall concentration for 0.05 LPM and 200 μm fiber-fiber spacing. DO saturation at these conditions is a concentration of 0.26 mol m^{-3}

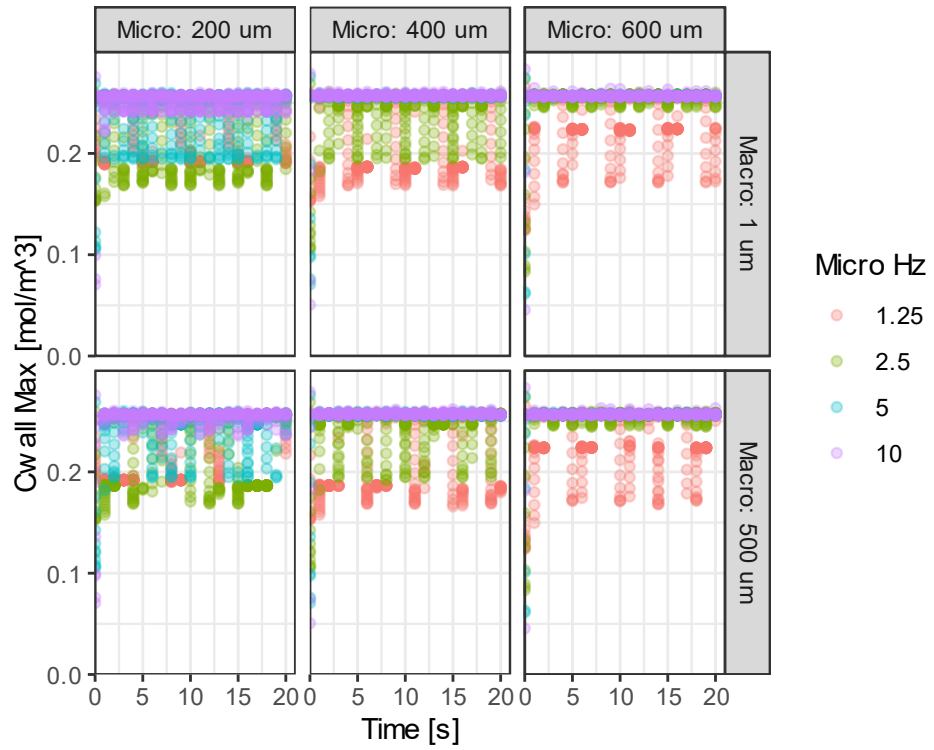


Figure 52: Time series data of maximum [right side] fiber wall concentration for 0.05 LPM and 400 μm fiber-fiber spacing. DO saturation at these conditions is a concentration of 0.26 mol m^{-3}

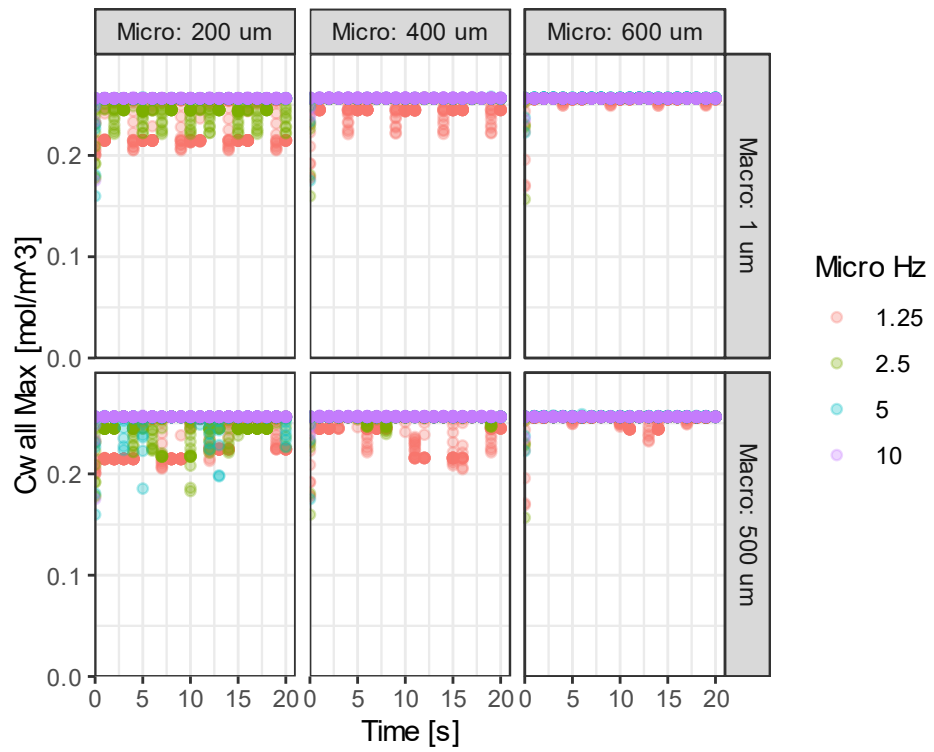


Figure 53: Time series data of maximum [right side] fiber wall concentration for 0.1 LPM and 100 μm fiber-fiber spacing. DO saturation at these conditions is a concentration of 0.26 mol m^{-3}

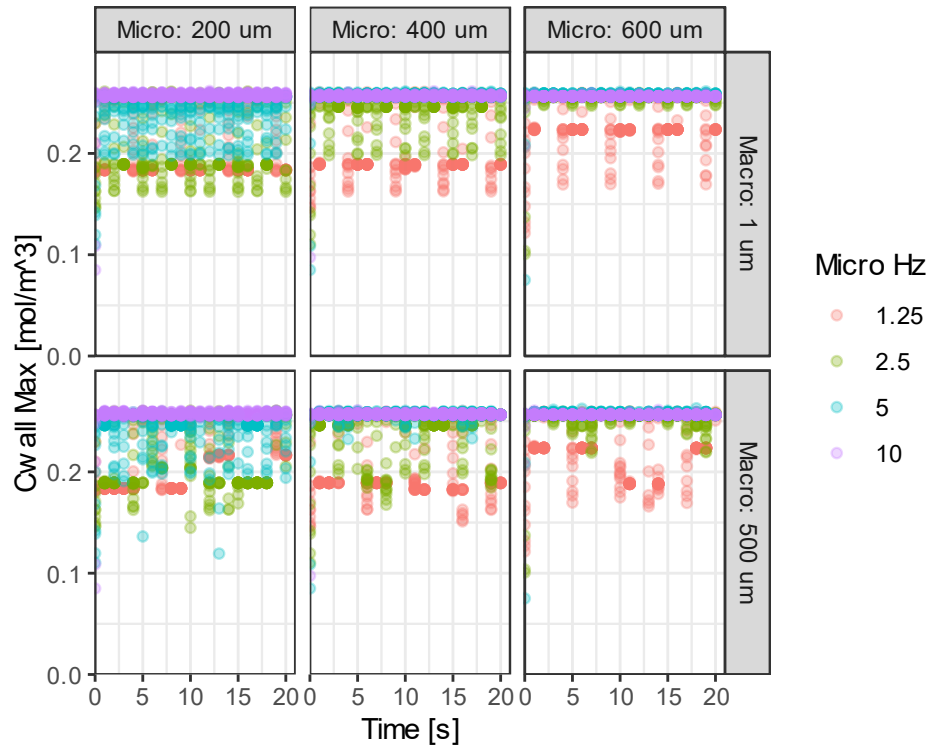


Figure 54: Time series data of maximum [right side] fiber wall concentration for 0.1 LPM and 200 μm fiber-fiber spacing. DO saturation at these conditions is a concentration of 0.26 mol m^{-3}

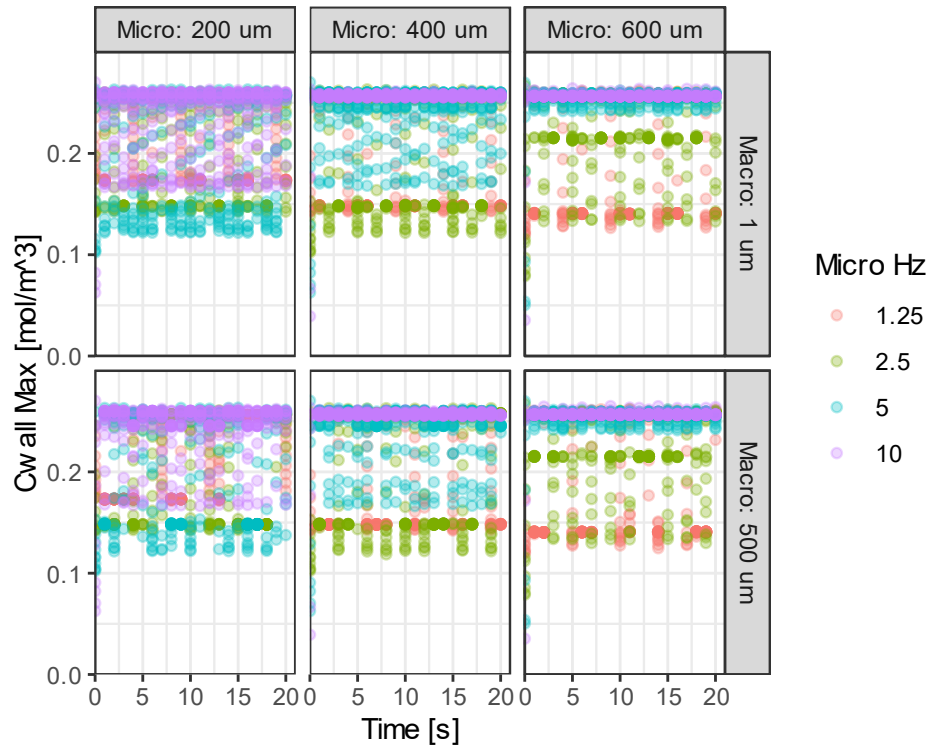


Figure 55: Time series data of maximum [right side] fiber wall concentration for 0.1 LPM and 400 μm fiber-fiber spacing. DO saturation at these conditions is a concentration of 0.26 mol m^{-3}

From these figures we can see that the maximum concentration that occurred was fairly similar between all model outputs. However, it is apparent that there are differences in the occurrences of a given wall concentration maximum as the micro and macro settings change. At the closest fiber-fiber spacing (100 μm), the maximum wall concentration was maintained for nearly all time series in both flow conditions (**Figure 50 and 53**). However, the smallest micro movements did transiently result in wall concentrations lower than the typical value (saturation $\sim 0.26 \text{ mol m}^{-3}$). As spacing increased from 100, to 200 and then 400 μm , two results become apparent: 1) the

instances of lowered 'maximum' concentration is increased and 2) higher frequency oscillations become affected. This result was compounded with an increase in flow (from 0.05 to 0.1 LPM), resulting in wall concentrations being affected by a given micro and macro setting differently. For example, the 2.5 Hz concentrations for 0.05 LPM flow (**Figure 51**) had no reductions at 400 μm micro displacements. Increased flow to 0.1 LPM (**Figure 54**) resulted in 2.5 Hz and 400 μm displacements lowering the wall concentrations with regularity.

Overall, it is clear the model predicts that under certain conditions, the (maximum) wall concentration can undergo large shifts which we can expect will affect DO transport. The magnitude of this effect depends greatly on both the system (total flow) as well as the fiber bundle properties (i.e., spacing, movement speed and distance). In particular at a given flow condition and fiber spacing, the impact of macro or no macro movement is not large, and if anything, it appears to show that there is a bit less of a reduction in predicted wall concentration maximums, especially at the smallest micro movement (200 μm) (See **Figure 54**, the micro only scenario has a much higher density of 5 Hz data points below the saturation values as compared to the micro + macro at the same micro movement magnitude). This is possibly due to the scale of motion being similar in these movements (500 μm macro motion vs a 200 - 600 μm micro motion). This was a constraint of the set-up of this 2D model (limited width), but nonetheless is possibly why we see no noticeable difference between the presence or

absence of macro motion in wall concentrations. Micro motion on the other hand had a clear impact, and the effect was increased with fiber spacing and flow increases. Notably the smaller the micro motion the larger the impact seen.

4.4 Conclusions

A simplified COMSOL Multiphysics model was used to investigate the effects of micro and macro-oscillations on oxygen transfer by an element of a fiber bundle. The analysis revealed that many factors improved overall oxygen mass transport in the system. Most notable are improved fiber spacing, increased system flow rates, and higher fiber velocities. The impacts of a micro and macro-oscillation motion were shown to improve overall oxygen mass transport in the system. However, the analysis demonstrated that under some conditions, the improvement of macro and micro movement together did not create larger mass fluxes than simply using a larger consistent motion (i.e., larger than micro only in this study). This result is similar to bench top results obtained in earlier work that demonstrated frequent small motions stepped across an overall distance (i.e., 11.25-degree oscillations stepped every second 22.5 degrees for a total of 180 degrees of motion) resulted in lower oxygen fluxes than one large motion across the entire range of motion (180-degree arcs). Further, the higher speed resulting in higher fluxes followed the trends seen in this work as expected. In addition to this result, the COMSOL analysis provided evidence that small frequent motion can reduce the maximum wall concentration of a given fiber as compared to

larger displacements. The impact of speed of motion appeared to be coupled with system fluid flow rates, suggesting that moving faster than the bulk liquid is replaced may net little to no reductions in wall concentrations.

Combined, this COMSOL investigation explains the reasons why micro-oscillations are reducing the incidence of bubbles on fiber walls in bench testing when the fibers are undergoing rapid small motions, while also producing less overall flux as compared to large oscillations back and forth over a larger distance. This result lends itself to future work to optimize the conditions of micro-oscillations such that bubble formation is reduced in bench top prototypes. Additionally, there is potential to optimize the range of motions used in micro-oscillations to reduce its negative impact on overall oxygen flux as compared to the large consistent motion of macro oscillation in real world testing.

5. Conclusions

5.1 Proof of concept work: hyperbaric oxygenation catheter feasibility

Intravascular oxygenation catheters have been developed in the past in attempts to deliver clinically significant amounts of oxygen. This work investigated the potential for hyperbaric pressures used with non-porous hollow fiber membranes to overcome mass transfer limitations in such a system. Proof-of-concept bench top testing was conducted with simple CSTR and tubular reactors, and demonstrated oxygen flux rates in water higher than previously reported in literature. Of note, under well-mixed conditions, fluxes as high as $550 \text{ mL min}^{-1} \text{ m}^{-2}$ were obtained in CSTR testing, while unmixed tubular reactor test yielded values near $400 \text{ mL min}^{-1} \text{ m}^{-2}$. Importantly, it was demonstrated that elevated pressures did not always cause bubble formation, and that some amount of mixing could reduce the number of bubbles. Pilot studies were completed with collaborators to develop bubble detection methods to quantitatively assess the amount and size of bubbles being formed using high frequency high frame rate ultrasound for use in future studies. This ultrasound method will be valuable for in vitro blood systems where visual bubble inspection is not possible. Along with developing experimental procedures and collecting data, this work facilitated modeling efforts that investigated both internal and external limitations of such a system. The model was used to determine the sensitivity to changes in membrane properties such as wall thickness and permeability, as well as external factors such as the pressure used

and the external mass transfer coefficient in the system, which was related to overall mixing. The model was used to predict that this hyperbaric approach has the potential to deliver significant amounts of oxygen using surface areas half the size (0.2 m^2) of previous devices. Importantly, this foundational work provided insight into what will be needed to successfully create future prototype devices using hyperbaric pressures. Specifically, it highlighted the need for active mixing methods that both improve flux due to convective transport and have the ability to reduce the bubble formation on the fiber during operation.

5.2 Angular oscillation active mixing applied to oxygenation catheter

The work performed on angular oscillation as an active mixing method has expanded on previous water-based feasibility testing using hyperbaric membrane oxygenations as a means to deliver oxygen directly into the bloodstream. This work demonstrates that the introduction of angular oscillation as a form of active mixing has allowed for oxygen fluxes of up to $400 \text{ mL min}^{-1} \text{ m}^{-2}$ to be maintained at lower pressures than the previous work without active mixing. This increase of almost $150 \text{ mL min}^{-1} \text{ m}^{-2}$ was achieved despite the use of water maintained at body temperature (37 C) and at the viscosity of blood (3.5 cP), both of which reduce oxygen transfer rates when compared to the 20 C water used in our previous work. Most importantly, the advent of bubbles in the system while undergoing angular oscillation was investigated. This work demonstrated that the active mixing helped to reduce bubbles overall, but micro-

oscillations added to the primary macro-oscillations had at least a qualitative reduction in bubbles that appeared on the surface of single fiber configurations. We noted that micro-oscillation mixing methods used had a negative impact on overall oxygen flux to a small degree; therefore, future work will need to balance bubble formation risk via a combination of both mixing and operating pressures. Further, adaptation of the previously developed mathematical model indicate continued improvements can be achieved with active mixing if increased angular speeds are possible. Future work in blood is needed to investigate the effects of angular oscillation on oxygen transport and bubble formation in an in vitro system, and to determine if this method of active mixing has any deleterious effects on red blood cells above certain oscillation speeds.

5.3 Computational fluid dynamic modeling of micro-scale mixing mechanisms for oxygenator catheter designs

A simplified COMSOL Multiphysics model was used to investigate micro and macro-oscillations in a mock fiber bundle. The modeling work conducted was not validated against a lab-scale model; however, overall modeling results were in agreement with the previous angular oscillation bench-scale testing. This analysis found that many factors impacted overall mass transport in such a system. Notably, total oxygen delivery was improved with increased fiber spacing, increased system flow rates, and higher fiber movement velocities. The results of the model lined up with experimental results that showed longer motions in a single direction tended to have larger overall oxygen fluxes. This was demonstrated in previous bench oscillation

experiments where 180-degree oscillations provided more oxygen delivery than 22.5-degree micro-oscillations. In the model, these movements were conducted in a linear mode ranging from 200 to 600 μm . At this small scale, the model still predicted 600 μm linear movements would provide more oxygen flux than 200 μm , even if velocities were constant. The model does predict conditions in which the macro-oscillation movement in conjunction with micro-oscillations could surpass the larger fiber movements as well, which should be a key focus in future optimizations of the mixing method. Notably, the scenarios where this occurred were interdependent on many of the operational factors, such as fluid flow, fiber spacing, and movement velocities.

A secondary goal of this investigation was to gain insight on the mechanisms reducing bubble formation in micro-oscillation scenarios tested at the bench scale. This modeling effort showed that under certain conditions the micro-oscillation itself could increase the range of maximum wall concentrations on the fiber at any given time, inherently reducing the chance for spontaneous bubble formation by reducing the amount of time concentrations remain high. The data from the model did not indicate that the macro steps used in this study had any additional impact on the wall concentrations being lowered. Additionally, the higher the velocities at which the fibers moved in conjunction with the liquid flow rates in the model showed the potential for fast velocities to actually help maintain a high wall concentration by preventing bulk fluid flow from evacuating the region of high concentration liquid.

5.4 Conclusions

This work entailed the early development of a hyperbaric membrane oxygenation catheter design that could use high pressure oxygen to deliver more oxygen per meter of fiber than previous attempts. The proof-of-concept work laid the groundwork for this device, demonstrating that there were operational parameters such a device could operate at without significant bubble formation, while also showing the potential such a device has by delivering $550 \text{ mL min}^{-1} \text{ m}^{-2}$ under well mixed high-pressure tests. This early work also served as the basis for early model development to better understand potential system limitations in regards to mixing, pressures, and membrane properties, which will help guide continued development. Mixing studies confirmed that active mixing could be used to both improve flux, but also to limit bubble formation during operation, and that high flux rates of oxygen could be maintained at much lower pressures than in the previous work (without mixing). Finally, computational fluid dynamics modeling demonstrated that the angular oscillation mixing methodologies can potentially be optimized around system parameters, and will likely be required to maximize the potential of such a device.

The end goal for this work was to demonstrate the feasibility of an oxygenation catheter that could be made small enough for intravascular use, yet efficient enough to provide a clinical benefit in patients with hypoxic respiratory failure. The work presented here demonstrates the feasibility of such a device using hyperbaric membrane

oxygenation combined with angular oscillation. This work provides the foundation for future optimization of such a device using more refined mixing methods. This work will be ongoing with next steps involving testing in whole blood, the complete development of an ultrasound method to quantitatively track potential bubbles, and further mixing optimizations based on this current and future modeling efforts.

Appendix A – Supplemental Information: Development of a novel intravascular oxygenator catheter: Oxygen mass transfer properties across nonporous hollow fiber membranes

A.1 Oxygen Mass Transport and Model Equations

Table 8 below presents a list of parameters used in the development of the model for the intravascular oxygenator catheter, as well as the source of value if applicable (1Henry’s Constant [65]).

Table 8: List of model symbols and model parameter values (with sources)

Parameter	Symbol	Value	Units	Source
Partial pressure of oxygen in HFM	P_{fiber}	0.24 – 1.9 bar	cmHg	Pressure regulator
Partial pressure of oxygen on outer HFM wall	P_{wall}	Varies	cmHg	Model output
Concentration oxygen in liquid on outside wall	C_{wall}	Varies	$\frac{\text{mmol}}{\text{L}}$	Model output
Concentration oxygen in bulk liquid	C_{bulk}	varies	$\frac{\text{mmol}}{\text{L}}$	Model output
Permeability of HFM to oxygen	$P_{m_{\text{HFM}}}$	9.9×10^{-8}	$\frac{\text{cm}^3(\text{STP}) \cdot \text{cm}}{\text{cm}^2 \cdot \text{s} \cdot \text{cmHg}}$	Manufacturer
Convective mass transfer coefficient	k	Varies	$\frac{\text{cm}}{\text{s}}$	Fitted via model
HFM wall thickness	d_{fiber}	89	μm	Manufacturer
Area of membrane (in segment [j])	A_m	Varies	cm	Model discretization
Permeability of tygon tubing to oxygen	$P_{m_{\text{tygon}}}$	3.9×10^{-9}	$\frac{\text{cm}^3(\text{STP}) \cdot \text{cm}}{\text{cm}^2 \cdot \text{s} \cdot \text{cmHg}}$	Fitted via model
Convective mass transfer coefficient into liquid from tygon tubing	k_{tygon}	6.5×10^{-5}	$\frac{\text{cm}}{\text{s}}$	Fitted via model
Tygon tubing wall thickness	d_{tygon}	1.59	mm	Manufacturer
Henry’s Constant	K_H	58520	$\frac{\text{cm}^3 \cdot \text{cmHg}}{\text{mmol}}$	Literature ¹
Rate of oxygen transfer in a segment	R_i	Varies	$\frac{\text{mmol}}{\text{s}}$	Experimental data and model output
Volume liquid segment	V	Varies	L	Experimental data
DO Probe electrode reading	C_e	Varies	$\frac{\text{mmol}}{\text{L}}$	Experimental data, and model output
Actual DO concentration in probe chamber	C_p	varies	$\frac{\text{mmol}}{\text{L}}$	Model output

Oxygen transport equations were developed using fundamental transport mechanisms, using limitations across the fiber wall, and convective mass transport limitations into the bulk liquid. It was assumed that equilibrium at the interface was reached instantaneously. Figure 56 below presents the conceptual model used to develop transport equations (1-4) used in the model to describe both the CSTR and tubular systems.

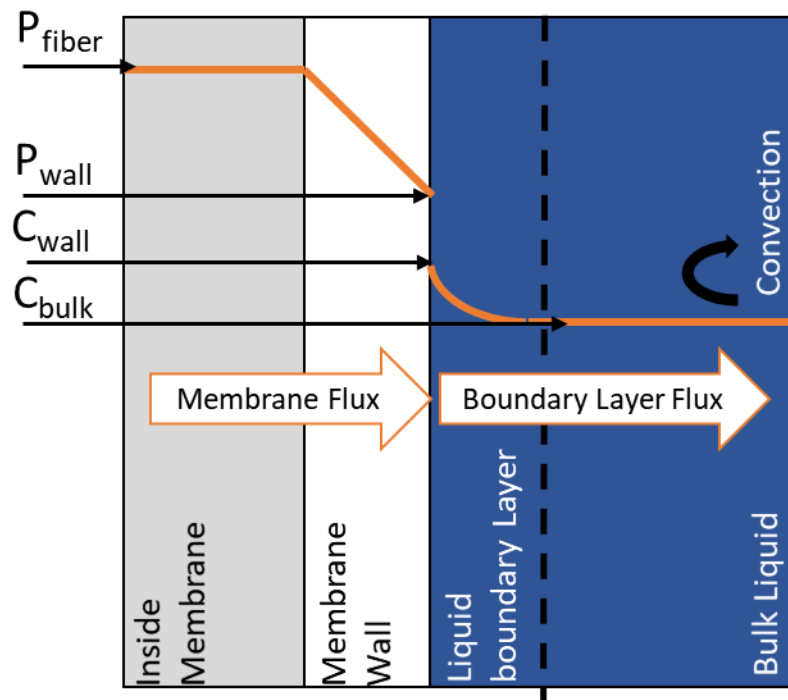


Figure 56: Conceptual model of the membrane interfaces with high pressure oxygen inside the fiber, diffusion through the non-porous membrane, liquid boundary layer, and bulk liquid.

Mass flux across the membrane was described by its permeability to oxygen, the pressure gradient across the fiber wall, and the fiber wall thickness:

$$J_{fiber} \left[\frac{mmol}{cm^2 s} \right] = -Pm_{HFM} / 22.4 \left[\frac{cm^3(STP)}{mmol} \right] \times \frac{(P_{wall} - P_{fiber})}{d_x} \quad (A.1)$$

Convective mass transport into the bulk liquid was described by the mass transfer coefficient for the system and the gradient of oxygen in the liquid from the membrane wall and bulk solution:

$$J_{convective} \left[\frac{mmol}{cm^2 s} \right] = k \times (C_{wall} - C_{bulk}) \quad (A.2)$$

A conservation equation since no oxygen can accumulate at the membrane-liquid interface, thus the flux across the membrane fiber and the convective flux are equal:

$$J_{fiber} = J_{convective} \quad (A.3)$$

Partitioning of oxygen between the fiber and liquid phase was described using a simple partition coefficient. At the membrane interface, the concentration of oxygen is assumed to be in equilibrium:

$$C_{wall} = \frac{P_{wall}}{K_H} \quad (A.4)$$

These equations were used to develop the differential equations used in the model. As described below and in the paper, the model uses discretization of the length of the fiber (and tubular model bulk liquid) into segments. The bulk solution surrounding the segments was assumed to be well mixed, and the average pressure inside each HFM segment was assumed to be constant. Figure 57 below illustrates a single segment of the tubular model, and an example differential equation are provided.

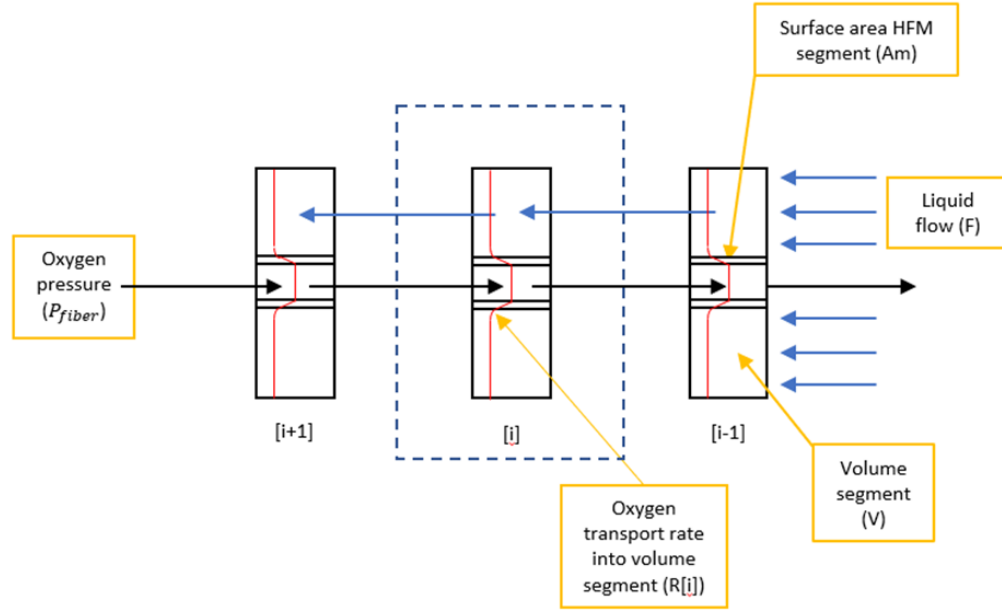


Figure 57: Schematic of discretization of tubular system model (single fiber). Each discrete segment (i) is considered ideally mixed. Liquid flow is countercurrent to the oxygen flow. The oxygen pressure drop from inlet (i=N) to outlet (i=1) is assumed linear.

Oxygen transfer rate into segment [i] from fiber segment [i]:

$$R[i] \left[\frac{\text{mmol}}{\text{s}} \right] = -Pm_{HFM} \times 22.4 \left[\frac{\text{cm}^3(\text{STP})}{\text{mmol}} \right] \times \frac{(P_{wall[i]} - P_{fiber[i]})}{dx} \times A_m \quad (\text{A.5})$$

Oxygen mass balance for one liquid segment:

$$\frac{dC[i]}{dt} = \frac{F(C[i-1] - C[i]) + R[i]}{V} \quad (\text{A.6})$$

The experimental system included the model intravascular oxygenator prototype, DO sensor, pump, bubble trap, etc. connected with Tygon tubing. Although the Tygon tubing was selected for its low permeability to oxygen, experiments at the lowest oxygen pressures and total membrane surface areas revealed that some oxygen permeated from air through the tubing and into the liquid, and affected the experiments.

Thus, this transport was included in the model (for data analysis, not for model sensitivity studies). Transport of oxygen across Tygon tubing was handled using the same equations as above. The Tygon segment was discretized in a similar way to the tubular model, and divided into 3 distinct lengths that separated the pump and CSTR/tubular system, the system and the bubble trap, and the bubble trap and pump. Tygon-related parameters were fitted using data collected without the CSTR or tubular system inline. A final discretized volume was added to the system to account for the volume of various fittings, assumed to be insignificantly permeable to oxygen as compared to Tygon. These volumes were added together, and incorporated into the model as a length of non-permeable 'tubing' the same inner diameter as the main system tubing.

Finally, the DO probe dynamics was incorporated as a first order lag-time (TE). The value logged in the data logger being the concentration at the electrode (Ce), and the true liquid concentration being the bulk liquid concentration around the probe (Cp). The chamber housing the DO probe was assumed to be well mixed. Probe lag TE was confirmed experimentally to be 9 seconds, and was incorporated via the following equation in the model:

$$\frac{dC_e}{dt} = \frac{(C_p - C_e)}{TE} \tag{A.7}$$

A.2 Supplemental Figures

Additional figures showing model fits not shown in the manuscript [chapter 2] for **Figure 12** are provided in **Figure 58**. The model fit for 400 rpm CSTR system is shown in **A**, and the 0.5 L min⁻¹ system model fit is shown in **B**.

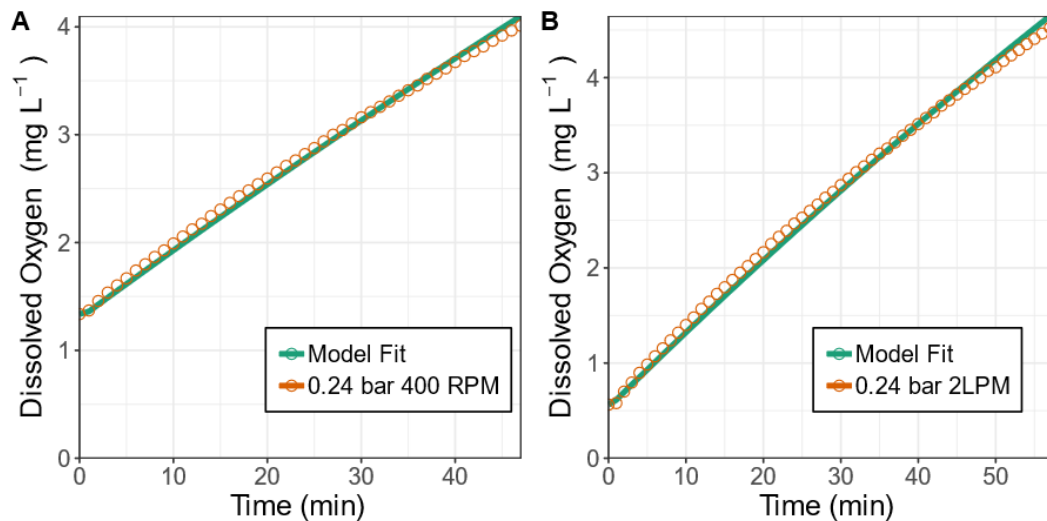


Figure 58: Model fitting for the convective mass transfer coefficient for the CSTR at 400 rpm CSTR (A) and the tubular device at 0.5 L min⁻¹ (B) for a single replicate. Model fitting used replicates of 0.24 bar experiments to find an average k value (one set of CSTR and tubular) for each mixing scenario (400/1200 rpm and 0.5/2.0 L min⁻¹).

A.3 On-line videos

Two videos are available on-line (see links with the SI): Video 1 shows sample B-mode and spatial coherence image frames spanning 100 msec at 4 kHz from a sample acquisition along the direction of flow (“Run 1” in Figure 7). The 15 individually identified bubbles are circled in the coherence images as they are tracked across the frames and their motions are shown in the rightmost plot. Video 2 shows sample

tracking of 19 bubbles in images collected across the direction of flow at 20 kHz as they cross through the imaging plane.

Appendix B Oxygenation Catheter mixing via rotational oscillation

Oxygen transport equations were developed using fundamental transport mechanisms, using limitations across the fiber wall, and convective mass transport limitations into the bulk liquid. It was assumed that equilibrium at the interface was reached instantaneously. **Figure 59** below presents the conceptual model used to develop transport equations (B1-4) used in the model to describe both the CSTR and tubular systems.

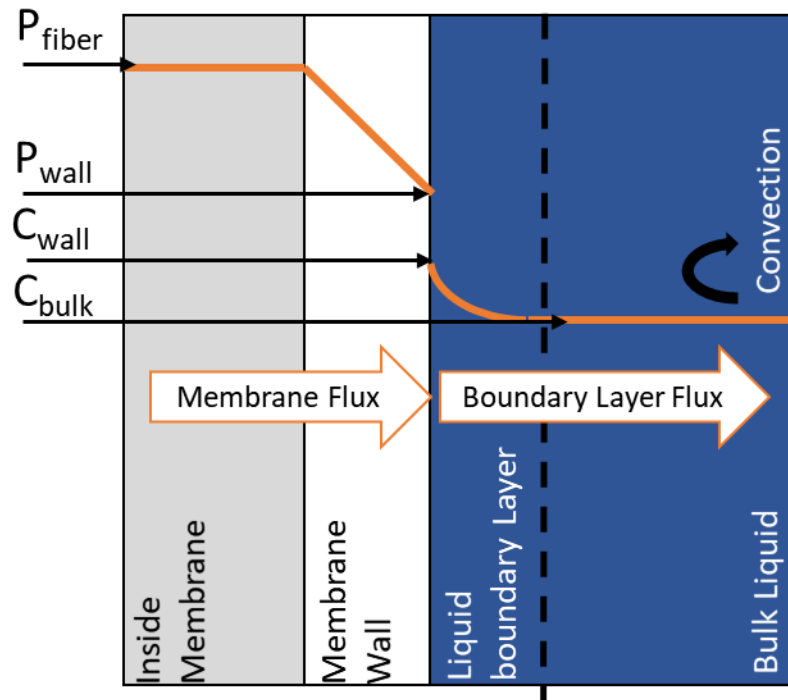


Figure 59: Conceptual model of the membrane interfaces with high pressure oxygen inside the fiber, diffusion through the non-porous membrane, liquid boundary layer, and bulk liquid.

Mass flux across the membrane was described by its permeability to oxygen, the pressure gradient across the fiber wall, and the fiber wall thickness:

$$J_{fiber} \left[\frac{mmol}{cm^2 s} \right] = -Pm_{HFM} / 22.4 \left[\frac{cm^3(STP)}{mmol} \right] \times \frac{(P_{wall} - P_{fiber})}{d_x} \quad (B.1)$$

Convective mass transport into the bulk liquid was described by the mass transfer coefficient for the system and the gradient of oxygen in the liquid from the membrane wall and bulk solution:

$$J_{convective} \left[\frac{mmol}{cm^2 s} \right] = k \times (C_{wall} - C_{bulk}) \quad (B.2)$$

A conservation equation since no oxygen can accumulate at the membrane-liquid interface, thus the flux across the membrane fiber and the convective flux are equal:

$$J_{fiber} = J_{convective} \quad (B.3)$$

Partitioning of oxygen between the fiber and liquid phase was described using a simple partition coefficient. At the membrane interface, the concentration of oxygen is assumed to be in equilibrium:

$$C_{wall} = \frac{P_{wall}}{K_H} \quad (B.4)$$

These equations were used to develop the differential equations used in the model. As described below and in the paper, the model uses discretization of the length of the fiber (and tubular model bulk liquid) into segments. The bulk solution surrounding the segments was assumed to be well mixed, and the average pressure inside each HFM segment was assumed to be constant. Because this model accounts for

a 'looped' fiber, each segment will have half the fibers in the system with a higher pressure than the other half for a given segment. This is due to the pressure drop profile along the fibers. To account for this, the number of fibers (N) were divided in half, with N/2 undergoing a pressure drop from inlet to the midpoint of the fiber and the other half seeing a pressure drop from the mid-point to the outlet of the fiber bundle.

Mathematically this was accomplished by doubling the number of discretized sections for the fibers as compared to the mock vein, resulting in 10 segments for the vein, and 20 segments for the membrane. Therefore, each vein segment of the model had two separate flux equations depending on if the fibers were on the outlet or inlet side of the equation. **Figure 60** below illustrates a single segment of the tubular model, and an example differential equation are provided.

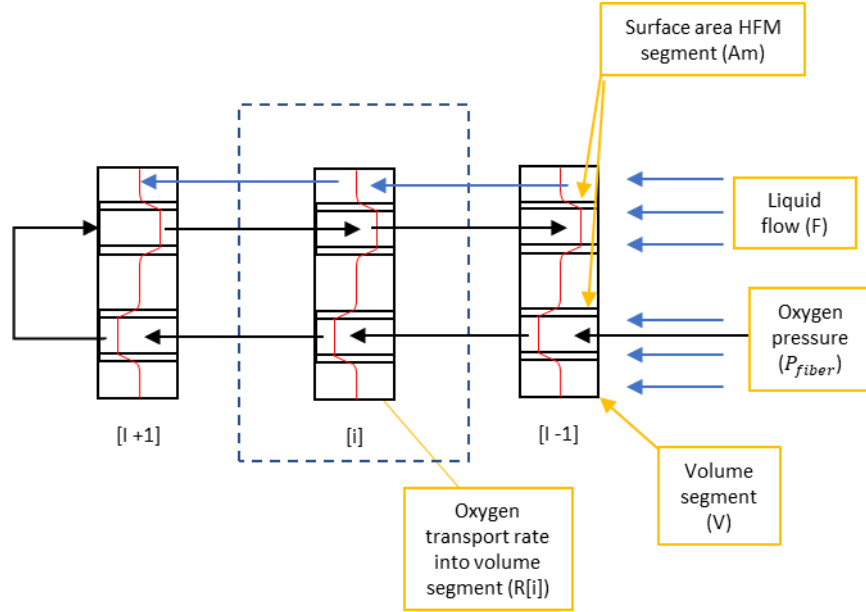


Figure 60: Schematic of discretization of tubular system model (single fiber looped). Each discrete segment (i) is considered ideally mixed. Liquid flow is entering at the same end as the oxygen flow. The oxygen pressure drop from inlet (i=N) to outlet (i=1) is assumed linear along the length of the entire loop.

Oxygen transfer rate into segment [i] from fiber segment [i]:

$$R[i] \left[\frac{mmol}{s} \right] = -Pm_{HFM} \times 22.4 \left[\frac{cm^3(STP)}{mmol} \right] \times \frac{(P_{wall[i]} - P_{fiber[i]})}{d_x} \times \frac{A_m[i]}{2} \quad (A.5)$$

$$R[i] \left[\frac{mmol}{s} \right] = -Pm_{HFM} \times 22.4 \left[\frac{cm^3(STP)}{mmol} \right] \times \frac{(P_{wall[N*2-i+1]} - P_{fiber[N*2-i+1]})}{d_x} \times \frac{A_m[i]}{2}$$

(B.6)

Oxygen mass balance for one liquid segment:

$$\frac{dc[i]}{dt} = \frac{F(c[i-1] - c[i]) + R[i]}{v} \quad (B.7)$$

Finally, the DO probe dynamics was incorporated as a first order lag-time (TE).

The value logged in the data logger being the concentration at the electrode (C_e), and the true liquid concentration being the bulk liquid concentration around the probe (C_p). The

chamber housing the DO probe was assumed be well mixed. Probe lag TE was confirmed experimentally to be 9 seconds, and was incorporated via the following equation in the model:

$$\frac{dc_e}{dt} = \frac{(c_p - c_e)}{TE} \quad (\text{B.7})$$

References

- [1] L. Dwyer-Lindgren *et al.*, "Trends and Patterns of Differences in Chronic Respiratory Disease Mortality Among US Counties, 1980-2014," *JAMA*, vol. 318, no. 12, p. 1136, Sep. 2017, doi: 10.1001/jama.2017.11747.
- [2] "WHO | Chronic respiratory diseases (CRDs)," *WHO*, 2019, Accessed: Mar. 06, 2019. [Online]. Available: <https://www.who.int/respiratory/en/>.
- [3] H. Wang *et al.*, "Global, regional, and national life expectancy, all-cause mortality, and cause-specific mortality for 249 causes of death, 1980–2015: a systematic analysis for the Global Burden of Disease Study 2015," *Lancet*, vol. 388, no. 10053, pp. 1459–1544, Oct. 2016, doi: 10.1016/S0140-6736(16)31012-1.
- [4] N. C. for H. S. (NCHS), "Table 19. Leading causes of death and numbers of deaths, by sex, race, and Hispanic origin: United States, 1980 and 2016," 2017. Accessed: Mar. 06, 2019. [Online]. Available: <https://www.cdc.gov/nchs/hus/contents2017.htm#019>.
- [5] J. L. Dieleman *et al.*, "US Spending on Personal Health Care and Public Health, 1996-2013," *JAMA*, vol. 316, no. 24, p. 2627, Dec. 2016, doi: 10.1001/jama.2016.16885.
- [6] S. Gupta, J. Sankar, R. Lodha, and S. K. Kabra, "Comparison of prevalence and outcomes of pediatric acute respiratory distress syndrome using pediatric acute lung injury consensus conference criteria and Berlin definition," *Front. Pediatr.*, 2018, doi: 10.3389/fped.2018.00093.
- [7] K. Parvathaneni, S. Belani, D. Leung, C. J. L. Newth, and R. G. Khemani, "Evaluating the Performance of the Pediatric Acute Lung Injury Consensus Conference Definition of Acute Respiratory Distress Syndrome," *Pediatr. Crit. Care Med.*, vol. 18, no. 1, pp. 17–25, Jan. 2017, doi: 10.1097/PCC.0000000000000945.
- [8] M. W. Quasney, Y. M. López-Fernández, M. Santschi, and R. S. Watson, "The outcomes of children with pediatric acute respiratory distress syndrome: Proceedings from the Pediatric Acute Lung Injury Consensus Conference," in *Pediatric Critical Care Medicine*, Jun. 2015, vol. 16, no. 5, pp. S118–S131, doi: 10.1097/PCC.0000000000000438.
- [9] R. Mac Sweeney and D. F. McAuley, "Acute respiratory distress syndrome," *Lancet*, vol. 388, no. 10058, pp. 2416–2430, Nov. 2016, doi: 10.1016/S0140-6736(16)00578-X.

- [10] G. Grasselli, A. Pesenti, and M. Cecconi, "Critical Care Utilization for the COVID-19 Outbreak in Lombardy, Italy: Early Experience and Forecast during an Emergency Response," *JAMA - Journal of the American Medical Association*, vol. 323, no. 16, American Medical Association, pp. 1545–1546, Apr. 28, 2020, doi: 10.1001/jama.2020.4031.
- [11] E. Livingston and K. Bucher, "Coronavirus Disease 2019 (COVID-19) in Italy," *JAMA*, vol. 323, no. 14, p. 1335, Apr. 2020, doi: 10.1001/jama.2020.4344.
- [12] "ECLS Registry Report, International Summary," Ann Arbor, MI, 2020. Accessed: May 18, 2020. [Online]. Available: <https://www.else.org/Registry/Statistics/InternationalSummary.aspx>.
- [13] D. J. Wallace *et al.*, "Geographic access to high capability severe acute respiratory failure centers in the United States," *PLoS One*, vol. 9, no. 4, Apr. 2014, doi: 10.1371/journal.pone.0094057.
- [14] J. D. Mortensen, "Intravascular Oxygenator: A New Alternative Method for Augmenting Blood Gas Transfer in Patients With Acute Respiratory Failure," *Artif. Organs*, vol. 16, no. 1, pp. 75–82, Nov. 1992, doi: 10.1111/j.1525-1594.1992.tb00271.x.
- [15] B. G. Hattler *et al.*, "A respiratory gas exchange catheter: In vitro and in vivo tests in large animals," *J. Thorac. Cardiovasc. Surg.*, vol. 124, no. 3, pp. 520–530, Sep. 2002, doi: 10.1067/mtc.2002.123811.
- [16] S. A. Conrad, A. Bagley, B. Bagley, and R. N. Schaap, "Major Findings from the Clinical Trials of the Intravascular Oxygenator," *Artif. Organs*, vol. 18, no. 11, pp. 846–863, Nov. 1994, doi: 10.1111/j.1525-1594.1994.tb03334.x.
- [17] J. D. Mortensen, "An Intravenacaval Blood Gas Exchange (IVCBGE) Device A Preliminary Report," *ASAIO J.*, vol. 33, no. 3, 1987, [Online]. Available: https://journals.lww.com/asaiojournal/Fulltext/1987/07000/An_Intravenacaval_Blood_Gas_Exchange_IVCBGE_99.aspx.
- [18] W. J. Federspiel *et al.*, "Recent progress in engineering the Pittsburgh intravenous membrane oxygenator," *ASAIO J.*, vol. 42, no. 5, pp. M435-441, Sep. 1996, doi: 10.1097/00002480-199609000-00026.
- [19] W. J. Federspiel *et al.*, "Ex vivo testing of the intravenous membrane oxygenator," *ASAIO J.*, vol. 46, no. 3, pp. 261–267, May 2000, doi: 10.1097/00002480-200005000-00004.

- [20] H. J. Eash, B. J. Frankowski, K. Litwak, W. R. Wagner, B. G. Hattler, and W. J. Federspiel, "Acute in vivo testing of a respiratory assist catheter: Implants in calves versus sheep," *ASAIO J.*, vol. 49, no. 4, pp. 370–377, Jul. 2003, doi: 10.1097/01.mat.0000074991.94234.b6.
- [21] J. F. Golob *et al.*, "Acute in vivo testing of an intravascular respiratory support catheter," *ASAIO J.*, vol. 47, no. 5, pp. 432–437, 2001, doi: 10.1097/00002480-200109000-00003.
- [22] M. Macha *et al.*, "Acute in vivo studies of the Pittsburgh intravenous membrane oxygenator," *ASAIO Journal*, vol. 42, no. 5. Lippincott Williams and Wilkins, pp. M609-614, Sep. 01, 1996, doi: 10.1097/00002480-199609000-00060.
- [23] H. J. Eash, K. M. Mihelc, B. J. Frankowski, B. G. Hattler, and W. J. Federspiel, "Evaluation of fiber bundle rotation for enhancing gas exchange in a respiratory assist catheter.," *ASAIO J.*, vol. 53, no. 3, pp. 368–73, 2007, doi: 10.1097/MAT.0b013e318031af3b.
- [24] K. M. Mihelc, B. J. Frankowski, S. C. Lieber, N. D. Moore, B. G. Hattler, and W. J. Federspiel, "Evaluation of a respiratory assist catheter that uses an impeller within a hollow fiber membrane bundle," *ASAIO J.*, vol. 55, no. 6, pp. 569–574, Nov. 2009, doi: 10.1097/MAT.0b013e3181bc2655.
- [25] A. J. Makarewicz, L. F. Mockros, and R. W. Anderson, "A pumping intravascular artificial lung with active mixing," *ASAIO J.*, vol. 39, no. 3, pp. M466–M469, Jul. 1993, doi: 10.1097/00002480-199307000-00063.
- [26] A. J. Makarewicz, L. F. Mockros, and R. W. Anderson, "A dynamic intravascular artificial lung," *ASAIO J.*, vol. 40, no. 3, pp. M747–M750, Jul. 1994, doi: 10.1097/00002480-199407000-00099.
- [27] K. Tanishita, G. Panol, P. D. Richardson, and P. M. Galletti, "Gas transport in the intracorporeal oxygenator with woven tubes.," *Artif. Organs*, vol. 18, no. 11, pp. 797–800, Nov. 1994, doi: 10.1111/j.1525-1594.1994.tb03325.x.
- [28] V. Nodelman, H. Baskaran, and J. S. Ultman, "Enhancement of O₂ and CO₂ transfer through microporous hollow fibers by pressure cycling," *Ann. Biomed. Eng.*, vol. 26, no. 6, pp. 1044–1054, Nov. 1998, doi: 10.1114/1.115.
- [29] T. Sueda *et al.*, "Development of an intravascular pumping oxygenator using a new silicone membrane," *Artif. Organs*, vol. 21, no. 1, pp. 75–78, Nov. 1997, doi: 10.1111/j.1525-1594.1997.tb00703.x.

- [30] H. Kawakami *et al.*, "Development of a novel polyimide hollow fiber for an intravascular oxygenator.," *ASAIO J.*, vol. 43, no. 5, pp. M490-4, Sep. 1997, doi: 10.1097/00002480-199709000-00029.
- [31] T. Kanamori *et al.*, "Estimate of Gas Transfer Rates of an Intravascular Membrane Oxygenator," *ASAIO J.*, vol. 46, no. 5, pp. 612–619, Sep. 2000, doi: 10.1097/00002480-200009000-00021.
- [32] G.-B. Kim, S.-J. Kim, M.-H. Kim, C.-U. Hong, and H.-S. Kang, "Development of a hollow fiber membrane module for using implantable artificial lung," *J. Memb. Sci.*, vol. 326, no. 1, pp. 130–136, Jan. 2009, doi: 10.1016/j.memsci.2008.09.045.
- [33] D. S. Lawson *et al.*, "Hemolytic characteristics of three commercially available centrifugal blood pumps," *Pediatr. Crit. Care Med.*, vol. 6, no. 5, pp. 573–577, Sep. 2005, doi: 10.1097/01.PCC.0000163282.63992.13.
- [34] G.-B. Kim, C.-U. Hong, J.-S. Kim, M.-H. Kim, and H.-S. Kang, "Improvement of gas Transfer by Hemosome," *Int. J. Artif. Organs*, vol. 33, no. 3, pp. 171–178, Mar. 2010, doi: 10.1177/039139881003300306.
- [35] G. Cattaneo, A. Strauß, and H. Reul, "Compact intra-and extracorporeal oxygenator developments," *Perfusion*, vol. 19, no. 4, pp. 251–255, Jul. 2004, doi: 10.1191/0267659104pf748oa.
- [36] S. Cockroft, J. Kuo, M. P. Colvin, C. T. Lewis, R. F. Innis, and P. S. Withington, "Initial evaluation of an intracorporeal oxygenation device," *Anaesthesia*, vol. 47, no. 1, pp. 48–51, Jan. 1992, doi: 10.1111/j.1365-2044.1992.tb01954.x.
- [37] H. J. Eash, K. M. Mihelc, B. J. Frankowski, B. G. Hattler, and W. J. Federspiel, "Evaluation of fiber bundle rotation for enhancing gas exchange in a respiratory assist catheter," *ASAIO J.*, vol. 53, no. 3, pp. 368–373, May 2007, doi: 10.1097/MAT.0b013e318031af3b.
- [38] G. F. M. Cattaneo, H. Reul, T. Schmitz-Rode, and U. Steinseifer, "Intravascular Blood Oxygenation Using Hollow Fibers in a Disk-Shaped Configuration: Experimental Evaluation of the Relationship Between Porosity and Performance," *ASAIO J.*, vol. 52, no. 2, pp. 180–185, Mar. 2006, doi: 10.1097/01.mat.0000204151.56591.28.
- [39] S. Farling *et al.*, "Development of a Novel Intravascular Oxygenator Catheter: Oxygen Mass Transfer Properties Across Non-Porous Hollow Fiber Membranes," *Biotechnol. Bioeng.*

- [40] H. P. Wendel and G. Ziemer, "Coating-techniques to improve the hemocompatibility of artificial devices used for extracorporeal circulation," *European Journal of Cardio-thoracic Surgery*, vol. 16, no. 3. Eur J Cardiothorac Surg, pp. 342–350, Sep. 01, 1999, doi: 10.1016/S1010-7940(99)00210-9.
- [41] M. Barak and Y. Katz, "Microbubbles: Pathophysiology and clinical implications," *Chest*, vol. 128, no. 4, pp. 2918–2932, 2005, doi: 10.1378/chest.128.4.2918.
- [42] J. B. West and A. Luks, *West's respiratory physiology : the essentials*. 2016.
- [43] L. K. Von Segesser, M. Tönz, T. Mihaljevic, B. Marty, B. Leskosek, and M. Turina, "Intravascular oxygenation: Influence of the host vessel diameter on oxygen transfer," *ASAIO J.*, vol. 42, no. 4, pp. 246–249, Jul. 1996, doi: 10.1097/00002480-199642040-00003.
- [44] H. J. Eash, H. M. Jones, B. G. Hattler, and W. J. Federspiel, "Evaluation of plasma resistant hollow fiber membranes for artificial lungs," *ASAIO J.*, vol. 50, no. 5, pp. 491–497, Sep. 2004, doi: 10.1097/01.MAT.0000138078.04558.FE.
- [45] R. G. Jeffries, B. J. Frankowski, G. W. Burgreen, and W. J. Federspiel, "Effect of impeller design and spacing on gas exchange in a percutaneous respiratory assist catheter," *Artif. Organs*, vol. 38, no. 12, pp. 1007–1017, Dec. 2014, doi: 10.1111/aor.12308.
- [46] B. RG, M. MA, M. A, S. D, T. BT, and W. A, "Ventilation with Lower Tidal Volumes as Compared with Traditional Tidal Volumes for Acute Lung Injury and the Acute Respiratory Distress Syndrome," *N. Engl. J. Med.*, vol. 342, no. 18, pp. 1301–1308, May 2000, doi: 10.1056/nejm200005043421801.
- [47] J. Phua *et al.*, "Has Mortality from Acute Respiratory Distress Syndrome Decreased over Time?," *Am. J. Respir. Crit. Care Med.*, vol. 179, no. 3, pp. 220–227, Feb. 2009, doi: 10.1164/rccm.200805-722OC.
- [48] L. R. A. Schouten *et al.*, "Incidence and Mortality of Acute Respiratory Distress Syndrome in Children," *Crit. Care Med.*, vol. 44, no. 4, pp. 819–829, Apr. 2016, doi: 10.1097/CCM.0000000000001388.
- [49] M. J. Harvey, M. G. Gaies, and L. A. Prosser, "US and International In-Hospital Costs of Extracorporeal Membrane Oxygenation: a Systematic Review," *Appl. Health Econ. Health Policy*, vol. 13, no. 4, pp. 341–357, Aug. 2015, doi: 10.1007/s40258-015-0170-9.
- [50] W. J. Federspiel and K. A. Henchir, "Lung, Artificial: Basic Principles and Current

Applications," *Encyclopedia of Biomaterials and Biomedical Engineering*. pp. 922–931, 2004, doi: 10.1081/E-EBBE.

- [51] G. Montaldo, M. Tanter, J. Bercoff, N. Benech, and M. Fink, "Coherent plane-wave compounding for very high frame rate ultrasonography and transient elastography," *IEEE Trans. Ultrason. Ferroelectr. Freq. Control*, vol. 56, no. 3, pp. 489–506, Mar. 2009, doi: 10.1109/TUFFC.2009.1067.
- [52] R. S. Hsi *et al.*, "Feasibility of non-linear beamforming ultrasound methods to characterize and size kidney stones," *PLoS One*, vol. 13, no. 8, p. e0203138, Aug. 2018, doi: 10.1371/journal.pone.0203138.
- [53] P. Perez-Calleja, M. Aybar, C. Picioreanu, A. L. Esteban-Garcia, K. J. Martin, and R. Nerenberg, "Periodic venting of MABR lumen allows high removal rates and high gas-transfer efficiencies," *Water Res.*, vol. 121, pp. 349–360, Sep. 2017, doi: 10.1016/j.watres.2017.05.042.
- [54] The Chemours Company, "Teflon™ AF: Product Information." 2016, [Online]. Available: <https://www.teflon.com/en-/media/files/teflon/teflon-af-product-info.pdf>.
- [55] K. M. High, T. Nicholson, R. B. Richard, G. R. J. Panol, K. Shelley, and M. T. Snider, "Effects of Blood Phase Oscillation on Gas Transfer in a Microporous Intravascular Lung," *ASAIO J.*, vol. 40, no. 3, pp. M735–M739, Jul. 1994, doi: 10.1097/00002480-199407000-00096.
- [56] S. N. Vaslef, L. F. Mockros, and R. W. Anderson, "Development of an Intravascular Lung Assist Device," *ASAIO Trans.*, vol. 35, no. 3, pp. 660–663, Jul. 1989, doi: 10.1097/00002480-198907000-00160.
- [57] G. Haller, E. Faltin-Traub, D. Faltin, and C. Kern, "Oxygen embolism after hydrogen peroxide irrigation of a vulvar abscess," *Br. J. Anaesth.*, vol. 88, no. 4, pp. 597–599, 2002, doi: <https://doi.org/10.1093/bja/88.4.597>.
- [58] H. Tabesh *et al.*, "Simulation of blood oxygenation in capillary membrane oxygenators using modified sulfite solution," *Biophys. Chem.*, vol. 195, pp. 8–15, Dec. 2014, doi: 10.1016/j.bpc.2014.07.005.
- [59] M. E. Taskin, K. H. Fraser, T. Zhang, B. P. Griffith, and Z. J. Wu, "Micro-scale Modeling of Flow and Oxygen Transfer in Hollow Fiber Membrane Bundle," *J. Memb. Sci.*, vol. 362, no. 1–2, pp. 172–183, Oct. 2010, doi: 10.1016/j.memsci.2010.06.034.

- [60] J. Zhang *et al.*, "Computational Study of the Blood Flow in Three Types of 3D Hollow Fiber Membrane Bundles," *J. Biomech. Eng.*, vol. 135, no. 12, p. 121009, Dec. 2013, doi: 10.1115/1.4025717.
- [61] S. R. Wickramasinghe and B. Han, "Designing Microporous Hollow Fibre Blood Oxygenators," *Chem. Eng. Res. Des.*, vol. 83, no. 3, pp. 256–267, Mar. 2005, doi: 10.1205/CHERD.04195.
- [62] S. R. Wickramasinghe, M. J. Semmens, and E. L. Cussler, "Mass transfer in various hollow fiber geometries," *J. Memb. Sci.*, vol. 69, no. 3, pp. 235–250, May 1992, doi: 10.1016/0376-7388(92)80042-I.
- [63] K. Y. Chan, H. Fujioka, R. B. Hirshl, R. H. Bartlett, and J. B. Grotberg, "Pulsatile Blood Flow and Gas Exchange Across a Cylindrical Fiber Array," *J. Biomech. Eng.*, vol. 129, no. 5, p. 676, Feb. 2007, doi: 10.1115/1.2768105.
- [64] J. Zhang, T. D. C. Nolan, T. Zhang, B. P. Griffith, and Z. J. Wu, "Characterization of membrane blood oxygenation devices using computational fluid dynamics," *J. Memb. Sci.*, vol. 288, no. 1–2, pp. 268–279, Feb. 2007, doi: 10.1016/J.MEMSCI.2006.11.041.
- [65] R. Sander, "Compilation of Henry's law constants (version 4.0) for water as solvent," *Atmos. Chem. Phys.*, vol. 15, no. 8, pp. 4399–4981, Apr. 2015, doi: 10.5194/acp-15-4399-2015.

Biography

Stewart Farling graduated from Northeastern High School in 2006, and received a bachelor's (2011) and Master's (2013) of science at North Carolina State University from the Department of Civil & Environmental Engineering. He studied environmental engineering, with a focus on soil and water remediation for his Master's.

Stewart worked as a consultant for 2 years after graduating from NC State in the field of soil and water remediation, before returning to Duke University to pursue a Ph.D. in Environmental Process Engineering under Dr. Deshusses. Stewart began his Ph.D. efforts in odor and bioaerosol related research, and authored a paper in the detection of enteric pathogens in the air related to pit emptying (listed below). While at Duke, Stewart became involved with Dr. Tobias Straube through his Ph.D. coursework and became a collaborator on the project that is the topic for his thesis: the development of a hyperbaric intravascular oxygenator, with one paper published to date (below).

S. Farling, T. Rogers, J. S. Knee, E. A. Tilley, J. Brown, and M. A. Deshusses, "Bioaerosol emissions associated with pit latrine emptying operations," *Sci. Total Environ.*, vol. 648, pp. 1082–1086, Jan. 2019, doi: 10.1016/j.scitotenv.2018.08.147.

S. Farling *et al.*, "Development of a Novel Intravascular Oxygenator Catheter: Oxygen Mass Transfer Properties Across Non-Porous Hollow Fiber Membranes," *Biotechnol. Bioeng.*